

Faculty of Engineering of University of Porto



Fabrication of Microelectrodes for *In Vitro* and Organotypic Cultures

Laura Apolinário

September of 2020

Faculty of Engineering of University of Porto



Fabrication of Microelectrodes for *In Vitro* and Organotypic Cultures

Laura Apolinário

Final Version

Dissertation For Master in Biomedical Engineering

Orientador: Ph.D. João Ventura

September of 2020

Resumo

O desenvolvimento de diagnósticos e terapias, assim como a compreensão de sistemas biológicos, depende da dissipação de fronteiras entre os dispositivos eletrônicos e o material orgânico.

Existem vários tipos de microeléctrodos, dos quais o microeléctrodo de matriz (MEA) é um sensor que permite a monitorização individual de vários pontos da amostra, sendo capaz de captar sinais com uma elevada resolução espacial. Particularmente, os microeléctrodos de matriz tridimensionais (MEA-3D) devido à sua geometria, permitem adquirir sinais com maior eficiência quando comparados com os microeléctrodos planares e alcançar sinais num plano mais alto do eixo Z das amostras orgânicas. Consequentemente, este tipo de microeléctrodos têm-se tornado populares em investigações com culturas 3D, nomeadamente culturas organotípicas ou *in vitro*.

O objectivo deste trabalho é fabricar um microeléctrodo de matriz 3D, recorrendo a um processo de nanofabricação de baixo custo, através de eletrodeposição de ouro com assistência de um molde. Propõe-se que este MEA-3D tenha estruturas com forma geral de um pilar, sendo constituídas por nanofios ancorados numa base, com uma altura mínima de 100 μm . Tal altura permite a aquisição de sinais acima da camada necrótica (aproximadamente 50 μm) inerente à extração da amostra organotípica.

O processo de fabricação recorre a métodos já bem estabelecidos como a fotolitografia, anodização e a eletrodeposição, a partir de um MEA planar comercial. Nos resultados demonstra-se a formação de moldes com poros bem definidos pela repetição do método de anodização, e a possibilidade de adaptar as suas dimensões (189 μm de espessura do molde, 259 nm de diâmetro do poros e 314 nm espaço interporo).

Apesar da simplicidade dos métodos utilizados neste processo de fabricação, a transferência

do molde para o substrato demonstra ser um passo complicado, do qual praticamente não existe registo na literatura. Desta forma, procedeu-se a uma otimização da transferência do molde ao substrato, sendo possível constatar a formação de nanofios em cerca de 70% da área de eletrodeposição, onde o molde se encontra aderido com sucesso ao substrato.

Neste trabalho são discutidas diferentes abordagens e possíveis razões em prol da aderência do molde de alumina ao substrato, propondo futuras direcções para reunir as condições necessárias para obter uma aderência total da membrana ao substrato. A transferência do molde constitui, portanto, um ponto critico para a obtenção de um processo de fabricação conveniente e de baixo custo.

Abstract

Diminish the borders between the electronics and the organic matter, are the most relevant to catalyze the progress in the development of diagnostics, therapies as well as disclose functionalities of the biological systems such as the neurons electrophysiology.

Within a wide range of micro signals recording devices, microelectrodes array are one of the most used tools for monitoring, since they acquire signals from a fine spatial resolution. Particularly, three dimensional microelectrode arrays (MEA-3D) has some advantage regarding planar MEA; such as acquire signal with lower impedance, as well as reach a higher z-axis plan in the organic sample. Therefore MEA-3D has been popular in studies with 3D cultures, either in organotypic culture or culture *in vitro*. However despite the wide range of microelectrodes options, there is a lack of microelectrode that are able to surpass the necrotic layer (has approximately 50 μm) inherent to the brain slices in organic culture as well as, simultaneously maintain the high aspect ratio.

Therefore the main objective in this work is to design and fabricate a 3D microelectrode, directly from a commercial planar 256 MEA 100/30iR-ITO. This microelectrode is featured by high aspect ratio gold micropillar, with 100 μm height. Additionally these micropillars are composed by nanowires which promote surface contact with the organic sample and hence increase the quality of electrical signal recorded.

For the fabrication of this microelectrode, is proposed a process based on template assisted electrodeposition. The process fabrication proposed, has the advantages to produce the 3D microelectrode directly from a planar MEA; also, this process relies in well-established techniques, namely: anodization, electrodeposition and photolithography.

The results demonstrates the formation of nanoporous template with well-defined pores through two step anodization, as well as their adaptability for tuning the pores dimensions (189 μm template thickness 259 nm of pore diameter and 314 nm of interpore distance).

Despite the simplicity of the methods used in this nanofabrication process, the transference of the template to the membrane is scarcely reported. Accordingly, in this work, this point of the process demonstrated to be considerably challenging. Thus, is discussed several forms of preparation for the optimization of the template adherence to the substrate, for further electrodeposition. As result it is achieved the formation of nanowires in 70% of the electrodeposited area, traducing on the area where the template successfully adhered to the substrate.

In this dissertation are discussed different reasons and approaches for the success of the template transference, which is also proposed different condition to achieve the total adherence of the membrane to the substrate, as future directions. Since the transference the critical point to achieve a convenient and low-cost nanofabrication process.

Contents

Resumo	V
Abstract.....	VIII
List of Figures	XIV
List of tables.....	XIX
Abreviation and Symbols	XXI
2 Introduction.....	1
2.1 Motivation.....	2
2.2 State of the art	2
2.3 Objective.....	3
2.4 Conclusion	3
3 Literature Review.....	7
3.1 Neuron electrophysiology: The Nervous System	7
3.1.1 Neurons anatomy and physiology	8
3.1.2 The membrane cellular and ions concentrations	9
3.1.3 Membrane electrophysiological proprieties as an approximation of the electrical circuit	14
3.2 Microelectrodes	19
3.2.1 . Measurement of electrical neural signals	20
3.2.2 Types of electrosignals from neurons.....	21
3.2.3 Extracellular recording	22
3.2.4 Interface between electrode electrolytes	24
3.2.5 Biocompatibility	26
3.2.6 Material for Microelectrodes	28
3.2.7 Micro Electrode types.....	30
3.3 Microelectrodes for organotypic culture and in vitro	34
3.3.1 Organotypic culture among other cultures	34
3.3.2 Fabrication of high aspect ratio microelectrode.....	37
3.4 Perspective on the present work	38

4	Material and Methods	39
4.1	Designing of the microfabrication process	39
4.1.1	Template Synthesis by Alumina Anodization	41
4.2	Electrochemical Deposition.....	46
4.3	Characterization of the microelectrodes.....	49
4.3.1	Profilometry.....	49
4.3.2	Scattered Electron Microscopy	49
4.3.3	Energy Dispersive Spectroscopy.....	49
5	Results and Discussion	51
5.1	The template synthesized.....	51
5.2	Optimization of the electrodeposition.....	55
5.2.1	Cyclic Voltammetry	55
5.2.2	Temperature	56
5.2.3	Continuous electrodeposition duration	57
5.3	Sputtered membrane	59
5.4	Transferring the NpAT to the Substrate	60
5.5	Future perspectives	70
6	Conclusion	73
	Bibliography	75

List of Figures

- Figure 2.1-** Image representative of neuronal tissue with its components: Astrocyte (dark blue), microglial cell (blue), neurons (yellow), oligodendrocytes (lighter blue) and ependymal cells (at red) that constitute the capillary; and their principal interactions between them [15]. 8
- Figure 2.2 -** Anatomy of regular neuron. It is composed fundamentally by three parts: Dendrites, Soma and Axon; in each part are discriminate with their important components. Also near to on dendrite is possible to visualize the communication of the former neuron with a second, this local of interaction is named synapse, where the signal from the other neuron is transmitted to the one display on the figure. [15] 9
- Figure 2.3. -** Illustration of Na^+/K^+ ion channel and antiporter ion pump on the neural membrane. On the ion pump at each transition there is consumption of ATP (“energy molecule”); where for each 3 Na ions that moves out the cell there is 2 ion of K that moves inside the cell. [17] 10
- Figure 2.4 -** Voltage-gated ions. Different conformation of the ion channel while their respective states (close, open and inactivated)[1]..... 13
- Figure 2.5 -** Schematization of the action potential at three perspectives: a) Reception of signal by the dendrites, proceed through the action potential and delivered at the synaptic end. The arrow shows the direction of the AP along the axon; b) Graphic of the three phases of mV -depolarization, repolarization and hyperpolarization; c) schematic voltage-gate ion channels dynamic at the same three phases, exhibiting the membrane potential values.[19] 14
- Figure 2.6 -** Equivalent electrical circuit of the membrane. [1]. A) Simplification circuit comprising: resistance R_m , electrical motive force E_m and capacitance C_m . B) Same circuit applied on the neuronal membrane, which includes Na^+ K^+ and Leak channels. The latter channel refers to leak channels representing other remain channels, for question of simplicity.[17] 15
- Figure 2.7 -** Representation of the equivalent circuit for passible uniform cable equation. C_m ; R_m - membrane capacitance and resistance, respectively; and R_a , I_a - Axial resistance and current, respectively. ΔX - dislocation of current in space [2]. 17
- Figure 2.8** Graphic of spatiotemporal resolution of the different techniques used to record neural activity. Each technique corresponding shadow box exhibits spatiotemporal range as the solid lines demonstrates the spatiotemporal resolution. Adapted from [7]. 21
- Figure 2.9 -** Schematic illustration of different types of electrosignals of the brain. Image adapted from [30] and [31]. Copyright 2008, Elsevier..... 22

Figure 2.10 - Schematic illustration of ion distribution upon the contact point between the abiotic material and electrolyte medium. The circles with plus and minus signal represent ions positively and negatively charged particles respectively; and circles with an arrow represent water dipole. Moreover it is defined inner and outer Helmholtz planes are also defined. Figure original from Bockris and Reddy, 1977 and adapted from [34].	24
Figure 2.11 - Electrical circuit at two context A. Electrical circuit of the interface between the electrode and electrolyte [3]. B. neuron-electronic junction, where R_{seal} is considered [54].	25
Figure 2.12 Young's modulus Scale. PaC denotes parylene C and PI - polyimide [3]	27
Figure 2.13 Schematic representation of the lack biocompatibility consequences and different foreign body reaction along time [81].	28
Figure 2.14 -Two images that allow to compare two electrodes, where at the image on right it suffer the buckling effect and in the right image the electrode has been correctly inserted. [5].	29
Figure 2.15 - Schematic illustration of different type of electrodes coating [3]	30
Figure 2.16 illustration and pictures of microwire microelectrode (A) illustration of single and a tetrode microwire (B)Michigan Electrode with single and tetrode microelectrode (C) Utah Electrode array [5]	32
Figure 2.17 Picture of Planar MEA A60 and schematic illustration of a microelectrode array . (A) micro-image of the centre of the microelectrode (B) cross view of one electrode of the MEA. Modified from: Egert et al., Brain Res Brain Res Protoc, 1998 [82].	33
Figure 2.18 A 3D microelectrode where the centre e expanded, with a picture of the structure at right up conner where the bar scales reads 10 μm . [57] Modified from A Heuschkel et al., J Neurosci Methods 2002. B picture of a mushroom shaped microelectrode at the top and more gernal view of a in vitro cultured neurons in mushroomshaped microelectrodes modified from Spira et al., 2015 [58]. C 3D-nanostructured boron doped diamond microelectrode modified from: Yvert et al, 2015 [59].	34
Figure 2.19 A. Schematic illustration of three type of cultures primary cultures in vitro, acute slices and organotypic slices [61]. B. picture from a hippocampal slice extract and transferred to a planar MEA [62].	35
Figure 2.20 Schematic representation of brain slice where demonstrates the necrotic layer inherent to its extraction.	36
Figure 3.1 - Schematic illustration of the fabrication of micropillar gold electrodes, resuming the principal steps of the process: 1-3-common steps of photolithography (2-spin coating, 3-exposure and development for PMMA patterning; 4- template transference; 5- electrodeposition of gold; 6- template removal; 7- removal of the remaining PMMA.	39
Figure 3.2 - Pictures of the mask produced at AutoCAD. A- General vision of the mask design featuring 16x16 circle array B - Demonstrates the diameter and interpore distance, in the figures reads 49,859798 μm and 100 μm respectively.	40
Figure 3.3 - Illustration of the central section of the final 3D MEA model design. 1- Nanowires form upon the bases; 2- Base, together with nanowires they for the micropillar; 3- the gold line conductors of the MEA devices; 4- the MEA substrate composed by Si.	41
Figure 3.4 Two types of formation layer type, during alumina oxidation. A- Barrier type B- Nanoporous type	42

Figure 3.5 - Illustration of the cross section of the PAA. Denotes the different dimensions in the membrane $d(int)$ - interpore distance; $d(p)$ pore diameter and $L(p)$ pore length also referred as the thickness of the membrane [14]..... 42

Figure 3.6 - illustrated by the graphic the ideal current density curve on during the mild anodization, which is accompanied with the schematized figures that illustrated evolution of the oxide layer along time of anodization process; the number identifying the each figure refers to one showing in the graphic, demonstrating the event on each phase [13] 43

Figure 3.7 - Anodization setup. 1- Base copper 2- O-ring rubber; 3 Aluminium sample 4 copper base connected to de sourcemeter; 5- fan to homogenize the electrolyte temperature 6 - structures that hold the Pt mesh an connects it to the sourcemeter 44

Figure 3.8 Schematic illustration of the formation of NpAT's steps. 1- illustration of the Al foil surface; 2- Al foil after the Electropolish process; 3- the formation of the pores after the first anodization; 4- Al foil after the removal of the alumina layer; 5- formation of the pores after the second anodization; 6 - result after the Al removal and pore opening. 45

Figure 3.9 - Schematic of chemical reaction for electrodeposition at the electrode-electrolyte interface [73]. 46

Figure 3.10. Different variables that influences the electrodeposition thermodynamics and kinetics.[73] 47

Figure 3.11. - Setup configuration of 3 electrodes for electrodeposition technique. A- Working electrode- cathode; B- reference electrode; B counter electrode- Pt mesh. The purple solution depicts the Orosene electrolyte..... 48

Figure 4.1. - Current density evolution along time, in mild anodization. A. First anodization for 24h; B. Second anodization 48h..... 52

Figure 4.2. SEM picture after the gold electrodeposition in NpAT formed form mild anodization. Through ImageJ, the and thickness (A), diameters and distance interpore (B) of the membrane were measure 147 μm , 82 nm and 104 nm, respectively 52

Figure 4.3 - Image capture through SEM technique. Demonstrates ductility of the nanowires resultants of the electrodeposition through NpAT produced form mild anodization 53

Figure 4.4. - Hard anodization graphics. The resulting development of current density of the three phases: Pre-Anodization, Anodization and After-anodization 54

Figure 4.5 - SEM picture after the gold electrodeposition in NpAT formed form hard anodization. Through ImageJ, the and thickness (A), diameters and distance interpore (B) of the membrane were measure 189 μm , 259 nm and 314 nm, respectively 54

Figure 4.6 - Cyclic Voltammetry of orosene, between -1,6 and 0 V with a scan rate of 100 mV/s..... 56

Figure 4.7 - Graphic of current density curve the experiment where it is been electrodeposited continuously during 3600 s corresponding to 1 h. 57

Figure 4.8 - Graphic of the current density curve development as it accumulatively implemented 10 min of electrodeposition, pausing 2 min between each other. The total duration is 6000 s corresponding to 1 h 42 min. 58

Figure 4.9 - Image captured from SEM of the sputtered membrane. In white are depicted the gold nanowires electrodeposited, with relatively same height, into the membrane depicted as the grey band. 59

Figure 4.10 - Results of the electrodeposition depicted graphically current density along time (A) and the top view of the electrodeposited NpAT (B) 60

Figure 4.11 - A-The final result of the preparation of vertical samples, where It disposes of a copper tape attached to the gold substrate, which in turn is isolated at the edges, either with S1818 (for the sample S) or varnish (for sample V). B and C describe the process for sample preparations. B -sample S preparation process: 1- spin coated application of the NpAT and baking of S1818. 2- Application of the acetone 3- removed acetone; C- sample V preparation process: a-the gold substrate b- application on the NpAT c- application of varnish surrounding the NpAT. 63

Figure 4.12 - A - Illustration of the cross view of the resulting samples preparation to be integrated on the set up illustrated in the left. It characterizes by the substrate peace (light blue) with a thin film of gold (in golden), wrapped in copper tape show at the right side of template. At the top centre of the substrate is illustrate NpAT with the respective pores, some on the centre are coloured at back demonstrating the ideal result. Surround it, the varnish showing in semi-transparent colour. B- Illustrates the setup similar to the anodization described ate section 3.2.1. Although in this case the electrolyte used is orosene depicted with a purple colouration instead. 64

Figure 4.13 - Pictures of the sample after the electrodeposition. A- Sample B demonstrates the broken template; B- Sample C was not electrodeposited, since the substrate broke soon enough to grow nanowires. D - Identical set up presented in Figure 4.12, but modified by introducing a piece of cotton bellow the sample. 65

Figure 4.14 - Sample E. A- at 8 h after electrodeposition B-12 h after electrodeposition 66

Figure 4.15 - SEM images demonstrating cross section of the sample E with only a half of the template removed. The scale of the images, it reads: A- 200 μm B- 10 μm C- 20 μm and D-10 μm 67

Figure 4.16 - A- Identical set up presented in Figure 4.13.D, but modified with an extra weight employer at the centre of the sample. B-Result of the sample F after the electrodeposition, where extra weight was employed..... 68

Figure 4.17 - EDS spectrum of the sample E with the NpAT 68

Figure 4.18 - Result of the preparation of the sample for proposed experience. A - Although the thickness of the layer is too high, therefore not the right sample; it demonstrates de distribution of orifices with the O-ring for scale. B- The sample prepared with the right thickness. 69

List of tables

Table 2.1 - Ion concentrations. Typical ion concentration in Giant squid and Mammalian neurons, in- and outside the cell and their respective Nernst (1) [16].	11
Table 4.1 - Resume of the condition implemented for produce NpAT from mild anodization	51
Table 4.2 - Resume of the condition implemented for produce NpAT from hard anodization.....	53
Table 4.3. - Thickness of samples electrodeposited with different temperature (17 °C room temperature, 20 °C 30 °C)	56
Table 4.4 - Picture that identify each representative sample, after the electrodeposition.	61
Table 4.5 - Resume of: the preparation condition for electrodeposition, results of observation and percentage of the electrodeposited area of the respective sample. Note that sample are not depicted in the previous table 4.4 due to the lack of change between before and after the electrodeposition	61

Abreviation and Symbols

Lista de abreviaturas e acrónimos (ordenadas por ordem alfabética)

3D	Three Dimensions
AAO.....	Anodic Aluminum Oxide
AP.....	Action Potentials
ATP.....	Adenosine Triphosphate
BBB.....	Blood Brain Barrier
C	Capacitance
CNS.....	Central Nervous System
CNT	Carbone Nanotubes
CP.....	Conductive Polymer
CPE	Constant Phase Element
Dp.....	Pore Diameter
Dint.....	Interpore distance
ECoG.....	Electrocorticography
EEG.....	Electroencephalography
F	Faraday Constant
FBR.....	Foreign Body Reaction
GHK.....	Goldman-Hodgkin-Katz

gM μ E.....	Gold Mushroom Microelectrode
HH.....	Hodgkin-Huxley
ITO	Indium Tin Oxide
Lp	Pore Length
LPF.....	Local Potential Field
M1.....	Manufacture 1
M2.....	Manufacture 2
MEA.....	Microelectrode Array
NpAT.....	Nanoporous Alumina Template
NW	Nanowire
PAA.....	Porous Anodic Alumina
Pac	Parolee C
PDMS.....	Polydimethylsiloxane
PEDOT	3, 4- Ethylenedioxythiophene
PI.....	Polyimide
PNS.....	Peripheral Nervous System
PSS.....	Poly (Styrene Sulfonate)
PPy	Polypyrrole
R.....	Resistance
RC.....	Resistance And Capacitance Circuit
SNR.....	Signal To Noise Ratio
Su-8.....	Set Of 8 Epoxy Groups
T	Temperature
Z	Valence Of The Ion

Chapter 1

Introduction

The nervous system is responsible for sensing, processing information and elaborating physiological responses; relies on billions of neurons between other cells to regulate all organism. As a fundamental unit of nervous system, neurons are highly specialized cells that interconnects deliberately with other cells in order to communicate through electrochemical signals. The information shared is encoded by different patterns of action potential (AP) sequences that are generated by these electrochemical signals, within neural circuit in different parts of the nervous system. Due to the electrical properties of these cells it is possible to record and transduce this signal to a machine interface by specialized sensors. Neuronal electrophysiology attends to study the neuronal activity relying on electrodes' sensitivity of these electrical pulses in the front line at biotic/abiotic interface [1, 2].

Defining the ideal electrode is still a challenge due to the constant compromising, since they have to deal with biocompatibility at the same time they must maintain its functionality as long as possible. Consequently, a wide range of microelectrode types have been developed, whose materials, size, shape are some of the variables that should be considered upon the fabrication of the microelectrode. The variety on each of those variables opens an endless number of options, therefore the microelectrode selected should be tuned to the objectives of the investigation in question. For instance, in vivo and in vitro models have distinct features that

bring to different advantages and disadvantages [3]. Organotypic cultures, in turn, as an ex vivo model benefits both from in vivo and in vitro models, such as the ability to control experiment environment as well as maintaining the architecture of the genuine neuronal networks. Particularly, 3D microelectrodes have showed in the recent literature an improved performance relatively to the planar electrodes [4].

1.1 Motivation

Neural networks still conceal key systems that endure pathologies as much as physiological mechanism of the nervous system. Understanding the electrophysiological mechanisms underlying communication between neurons is crucial to unveil the rules for the formation of a determined patterned neural network. The electrophysiology has therefore an enormous importance in neuroscience; since it depends on advances on microelectrodes engineering, which potentiates the investigation in different spatial and temporal scales. Furthermore, to do it so, is highly important to expand fabrication process possibilities, which enables to forge devices with such reduced dimension.

1.2 State of the art

Investigate the electrophysiological mechanics underlining neurons communication is conventionally achieved by patch clamping; yet such method requires high expertise to perfume the technique as it also implies damage to the cell [5]. Extracellular recording is less invasive as it enables to perceive electrical activity from multiple neurons at the same time. These characteristics are an asset to investigate the interaction between population neurons. The engineering of new fabrication protocol as well as the inclusion of different materials allowed the production of microelectrode arrays (MEAs) that permit to record several neurons simultaneously. The planar MEAs were first produce, followed by 3D MEAs which demonstrated ability to improve record signal with lower impedance and high signal to noise ratio since they extent their recording site surface without increasing the size of the electrode [6, 7].

Moreover, organotypic slice cultures are an innovative and a good alternative to in vitro models allowing study specific parts of the nervous system comprising several types of cell [8]. Nonetheless, within the wide range of microelectrode type option, often their structures are conceived in a context of in vivo experiments with a range of mm or, more recently, with a range of nm suitable for in vitro experiments promoting high spatiotemporal resolution [9, 10]. Therefore there are few reported precedents of microelectrode in the range of 100 μm with a corresponding lack of development of its fabrication process for organotypic culture [11].

The fabrication techniques of 3D microelectrodes often include lithography, etching and deposition process. Moreover, the fabrication of these structures with metal material resorts to electrodeposition as for polymeric structures uses template-based techniques such as hot embossing, draw lithography. Lately the development in 3D printing also assist the development of this structures [12]. Interestingly, template based electrodeposition, is a method that allow the syntheses of nanowires by electrodeposition into the pores of the template. This is an inexpensive method currently use to produce nanowires that does not require complex equipment comparatively to physical and chemical vapour deposition methods [13, 14].

1.3 Objective

The aim of this dissertation project it is to fabricate and characterize a nanostructured three-dimensional microelectrode, integrated on standard planar MEA, for electrophysiological studies either organotypic culture or in vitro models. The 3D MEA is composed by micropillar that consist on high aspect ratio nanowire anchored on a solid base; importantly, total height ($\sim 100\text{ }\mu\text{m}$) of the resultant structure is tall enough to surpass the layer of necrotic cells inherent to the extraction process. The microfabrication of proposed model resorts to template-assisted approach through nanoporous aluminium oxide membrane to produce nanowires attached to short base micropillars. The overall process comprises two well-established techniques: aluminium anodization and gold electrochemical deposition. Their implementation promotes simplicity and low-cost process that provide potential approach for batch fabrication.

1.4 Conclusion

The Dissertation is elaborated as it follows: in the first section of the chapter 2, it is provided a theoretical frame work about the neurons electrophysiology, which mechanisms of the membrane that enables the generation and transmission of electrical signal was well as the approximation of the electrophysiological properties of the membrane to the electrical circuit. This provides a context, to understand of the important characteristics required from microelectrode. So that, in the next section 2.2 is discussed the different proprieties of the microelectrode, namely differ material and shapes; and how those affects either their biocompatibility as well as efficiency. Also is provided small resume of organotypic cultures an influence of the microelectrodes influence the recording in 3D cultures, in section 2.3. Next, chapter 3 provide an detailed description of the designed microfabrication process, introducing method and techniques to achieve the proposed product. On the following sections, the

different methods and techniques are described, providing some insight about their mechanism of fabrication methods - Anodization and Electrodeposition, present in section 3.1 and 3.2 respectively; as well as characterization methods, in section 3.3 such as the profilometer, scattered electron microscopy and energy dispersive Spectroscopy. Then the next chapter comprises the results and discussion. It organized per the objective the experience, thus it starts with results of the template production through anodization at section 4.1; next the different test for optimization of the electrodeposition are describe, in section 4.2, so that, the temperature, the voltage and the duration of the electrodeposition are define for the further production of gold micropillar. In section 4.3 and 4.4 are described the sequence of adjustment and process in order to achieve an adequate membrane adherence. The chapter ends, in section 4.5. is recommended some experience for improve the coherence of the present results as well as it is proposed new approaches to overcome the remaining challenge. The dissertation finalizes with a brief resume, highlighting the hypothesis propose in precious chapter as well as it indicate future direction once this challenge is mastered.

Chapter 2

Literature Review

This chapter aims to introduce the main theoretical concepts that will be used in this dissertation and is divided in two sections: the first recapitulates general notions about neuron anatomy and further relating with its electrophysiology, including biological mechanism involved in the generation and propagation of signal on neuronal cells, such as action potential which is a primary via of communication in the nervous system; followed by the second section will describe the variety of microelectrodes for neuronal electrophysiology, focusing the extracellular recording and highlighting gold mushroom-shape microelectrode. We will conclude this chapter, at the third section with an outlook on the present work.

2.1 Neuron electrophysiology: The Nervous System

The nervous system is one of the most highly elaborate and enigmatic communication systems. It is able to sense and adapt both to external and internal conditions in order to maintain vital functions; as well as assemble self-consciousness for, besides others, behaviour and reasoning. To mitigate its complexity, various divisions were established based either on their physiology or on anatomy that complement each other and function together. However, the nervous system is divided into two major systems: the central nervous system (CNS) constituted by brain and the spinal cord and the peripheral nervous system (PNS) constituted by the nerves which roam every inch of the organism. Apart from neuron, the neuronal tissue is also composed roughly by the same amount of glial cell, shown in Figure 2.1. They support the neuron activity: astrocyte and microglia are responsible to regulate and protect the interstitial environment, respectively; and oligodendrocytes extension involves the axon which allows faster

communication between neurons [15].

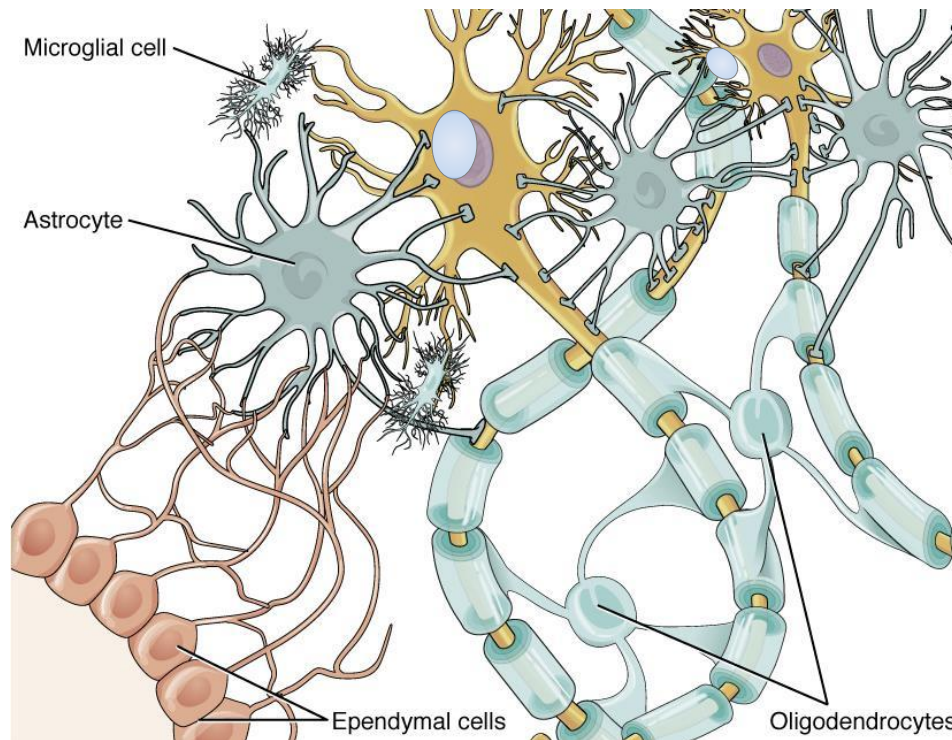


Figure 2.1- Image representative of neuronal tissue with its components: Astrocyte (dark blue), microglial cell (blue), neurons (yellow), oligodendrocytes (lighter blue) and ependymal cells (at red) that constitute the capillary; and their principal interactions between them [15].

This first section reviews general notion about neuron anatomy and further relating with its electrophysiology; including action potential and the dynamics of the ion channels, as fundamental supporting concepts. In the following section we will describe the membrane and the ion channel as well its dynamic, from an electrophysiological point of view.

2.1.1 Neurons anatomy and physiology

The neuron is the basic unit in the nervous system, although the connection between them can shape a very complex network that is capable of exchange, storage and process information within milliseconds. The neuron anatomy is composed of three main parts: the soma, the dendrites and the axon; as shown in Figure 2.2. Considering that the soma is the centre of the neuron it might be also referred as cell body; as other cells in our organism, the soma contains the nucleus, Golgi apparatus, mitochondria and other organelles required for the metabolism of the cell. While uniquely, the neuron is a specialized cell to transmit electrical signals, and

for such, the cell body exhibits projections from itself - axon and dendrites - to reach and connect with surrounding cells. The axon is the longer and more robust projection of the cell body, responsible for delivering the electrical signal to next cell; despite the reduce dimension of neuron's axon diameter (which leads to an slow signal displacement along the axon), the axon is often wrap in myelin sheets allowing a faster propagation of the signal; these sheets are cellular membrane extensions of oligodendrocyte or Schwan's cells from central and peripheral nervous system respectively. On the other hand, dendrites are responsible for the reception of electrical signals from other neurons, they exhibit more numerous and ramify projections, allowing establishing various point of communication with multiple neurons. This specific point or locations is called the synapse, where nerve impulses are transmitted by mediation of neurotransmitters which are chemicals compounds release from terminal axon to synaptic cleft giving the opportunity to bind to ion channels in the dendrites membrane of the next neuron and initiate a new signal propagation[15].

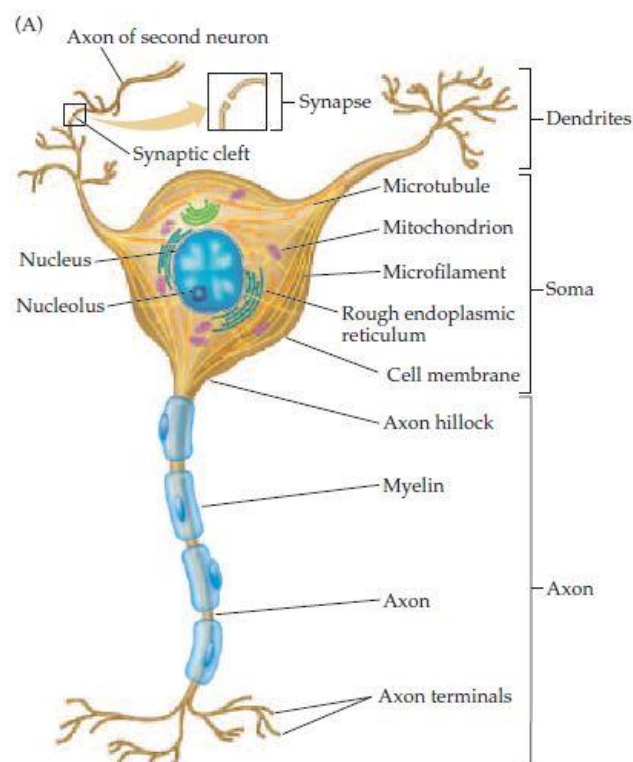


Figure 2.2 - Anatomy of regular neuron. It is composed fundamentally by three parts: Dendrites, Soma and Axon; in each part are discriminate with their important components. Also near to on dendrite is possible to visualize the communication of the former neuron with a second, this local of interaction is named synapse, where the signal from the other neuron is transmitted to the one display on the figure. [15]

2.1.2 The membrane cellular and ions concentrations

The neuronal membrane comprises a pair of phospholipids layers in which there is, among

them, different types of ion channels (Figure 2.3 and 2.4) constituted by transmembrane proteins. The phospholipids bilayer is an important barrier between extracellular and intracellular mediums. This separation results in inequivalent charges between two sides of the cell, avoiding the passage of the current through the barrier; and therefore it confers the property of insulator to the phospholipid bilayer. Moreover, the excitable property of the neurons relies on different ions concentrations and charge separation between the two medium [1]. This creates by definition, an electrical potential feature through the membrane known as membrane potential V_m ; which can be establish mathematically as the difference of intracellular V_i potential and extracellular potential, V_e ($V_m = V_i - V_e$) [16].

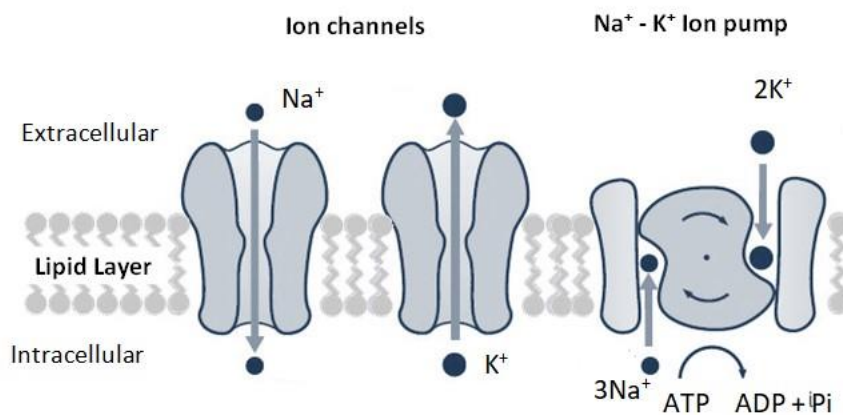


Figure 2.3. - Illustration of Na^+/K^+ ion channel and antiporter ion pump on the neural membrane. On the ion pump at each transition there is consumption of ATP ("energy molecule"); where for each 3 Na^+ ions that moves out the cell there is 2 ion of K^+ that moves inside the cell. [17]

Although the phospholipid bilayer permeability is quite restricted, due to the presence of ion channels such as pores, pumps or voltage gate channels in the neuronal membrane, there still is some flux of ions through the membrane, yet controlled. The pore, also referred as leak channel or simply ion channel, allows ions to migrate passively to other side of the membrane. These types of channels facilitate the passage selectively for specific ions to the opposite side of the membrane. On the other hand, electrogenic ion pumps restore, resorting to consumption of energy (ATP molecules), the ion concentration on the respective sides of the cell to preserving the polarity of the membrane, such as the Na^+/K^+ pump channel, in which for each two K^+ ions that flow outside the cell three Na^+ flows inside.

The movement of these ions across ion channels is driven by two main reasons: 1) Chemical diffusion - where the ions tend to move from higher to lower concentration areas; 2) Electrical diffusion - caused by the electrical field derived from ions that repel or attract one another, each pair of ions have the same or different charges respectively. These two oppose driving forces balance one another [1]. When it results in their cancellation; either there is no net movement of ions or an equal movement in and out of the cell; achieving, at this point, the equilibrium potential of the membrane. As long as it is referred to only one determined ion,

this point coincides with the definition of reversal potential. The reversal potential is the point where net movement across the membrane of the particular ion switches the direction [2].

A German physical chemist, named Walter Nernst formulated an equation, in 1888, determining the electrical potential E_X of a charged particle required reaching the equilibrium potential, depending on the concentration of the extracellular $[X]_{out}$ and intracellular $[X]_{in}$ environment of the particular ion X. This equation is well-known as the Nernst equation (1);

$$E_X = \frac{R_g T}{zF} \ln \left(\frac{[K^+]_{out}}{[K^+]_{in}} \right) \quad (1)$$

This formula also takes into account the temperature of the medium, T; the valence of the ion in question, z (the portion of the work necessary to divide a given amount of charge); the Faraday constant, F (C.mol⁻¹) as well as the constant of gas, R_g (J/K-1.mol⁻¹) [2].

The Nernst equation (1) only considers one ion permeable to the neuronal membrane. Nevertheless, it still provides valuable understanding of the correlation between these components. For particle positively charged like K⁺, it is possible to see that the value of E_K is positive as long as the concentration outside the cell is superior to the concentration inside the cell. In other hand, for particles negatively charge like Cl⁻, when it is more concentrated outside than inside the cell, E_{Cl} is negative [17]. It is also possible to perceive that in a steady ion concentration both inside and outside the cell, it has a tendency to move out of the cell once the membrane potential is above the potential equilibrium value and vice-versa.

However, in a more realistic situation, the membrane is permeable to multiple ions, where sodium (Na⁺) and potassium (K⁺) are the two main propellers of the signal propagation across the membrane, although other ions, like chloro (Cl⁻) and calcium (Ca²⁺), also participates on the electrical activity of the neuron. Thus, the membrane potential is often not equivalent to the membrane equilibrium of one particular ion neither the sum of their individual equilibrium. Giving it to consideration, Goldman proposed other expression, with a better approximation of what takes place in the neural membrane, which was handled by Hodgkin and Katz later on [2].

The Goldman-Hodgkin-Katz (GHK) expression defines the reversal membrane potential for a given set of monovalent ions concentration, which refers to the steady-state of the membrane potential V_m [2]. Assuming the membrane is permeable to K⁺, Na⁺ and Cl⁻, it reads:

$$V_m = \frac{RT}{F} \ln \left(\frac{(p_K [K^+]_{out} + p_{Na} [Na^+]_{out} + p_{Cl} [Cl^-]_{in})}{(p_K [K^+]_{in} + p_{Na} [Na^+]_{in} + p_{Cl} [Cl^-]_{out})} \right) \quad (2)$$

The values of V_m resulting from GHK equation lies between the potential equilibrium of different ions that move independently across the membrane. Although this equation (2) is similar to the Nernst equation (1), the total current takes into account the sum of the individual currents of various ions, assuming that each ion does not influence the movement of others [17].

Table 2.1 - Ion concentrations. Typical ion concentration in Giant squid and Mammalian neurons, in- and outside the cell and their respective Nernst (1) [16].

	Ions	Inside (mM)	Outside (mM)	Nernst eq
Giant squid				
	K ⁺	400	20	-75
	Na ⁺	50	440	55
	Cl ⁻	40-150	560	-66 to -33
	Ca ²⁺	10 ⁻⁴	10	145
Mammalian cell				
	K ⁺	140	5	-89,7
	Na ⁺	5-15	145	61 to 90
	Cl ⁻	4	110	-89
	Ca ²⁺	10 ⁻⁴	2.5 – 5	136 to 145

As illustrated in table 2.1, either both in giant squid (firstly studied due to its large dimensions) and mammalian neurons: K⁺ ions are the exception since, conversely to the other ions such as Na⁺, they have greater concentration intracellularly in comparison to extracellular space. Hence, the intracellular potential is more negative relatively to the extracellular environment, as the positive ions in general stands outside the cell.

As long as the membrane potential cell has no significant external perturbations, it remains in resting potential state. Due to the ions concentration on the different sides of the membrane at resting potential, it exhibits conventionally, a potential around -70 mV [18]. However the neuronal membrane, as an excitable cell, is often subject to electrical potential alterations. For instance, the electrical signals gathered by the dendrite, either with excitatory or inhibitory nature, converge on the soma. The quantity of signals arrival per unit time - firing rate, builds up on the axon hillock to a major signal response. Depending on its amplitude that affects the membrane potential, the response may trigger different reactions on the propagation of the electrical signal. For instance: 1) if the electrical potential of the neural membrane does not suffer major changes, the electrical signal propagates through the membrane but dissipates along the distance. 2) Conversely, if the membrane potential alteration large enough to reach the electrical potential threshold, it triggers an abrupt and short-lived rise on the electrical potential of the membrane. Consequently, it enables the activation of the voltage-gated ion channels and the propagation along the axon without attenuation, which reflects the active propriety of the membranes called action potential (AP)[1].

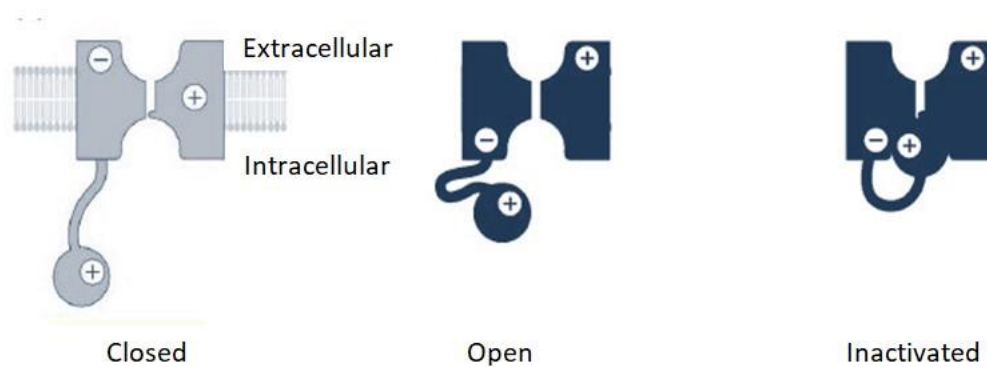


Figure 2.4 - Voltage-gated ions. Different conformation of the ion channel while their respective states (close, open and inactivated)[1]

The action potential is the fundamental instrument for neurons to communicate between them. The high peak of the membrane potential that generates the action potential is sustained by the presence of a third type of ion channel in the neuronal membrane, the voltage gate ion channel. These channels are sensible to the electrical potential above the thresholds of -55mV . When electrical potential reaches the threshold, it leads to the opening of the Na^+ and K^+ voltage gate channels (Figure 2.4). However, a shortly late reaction of the K^+ gate channels to the change of the membrane electrical potential leads to a difference in time shift between the Na^+ and K^+ movement through the cell. This difference is crucial, the increase of the Na^+ ions permeability when the K^+ are still to open causes a high peak in the membrane potential (up to 20 mV) and therefore depolarization (Figure 2.12.c-1). By the time the K^+ ion channels opens releasing K^+ ions outside the cell allowing the repolarization (Figure 2.12.c-2) of the membrane and the Na^+ channels are inactivated. Note that the inactivation state of the ion channels limits the membrane to trigger two action potentials too close in time also prevents the action potential to travel backwards; this moment is called refractory period. The last phase of the action potential hyperpolarization (Figure 2.12.c-3) is characterize by the returning of the membrane potential to the resting state after to the further reduction on the membrane potential caused by leak of K^+ ions due to the late closing of its voltage-gated channels [1].

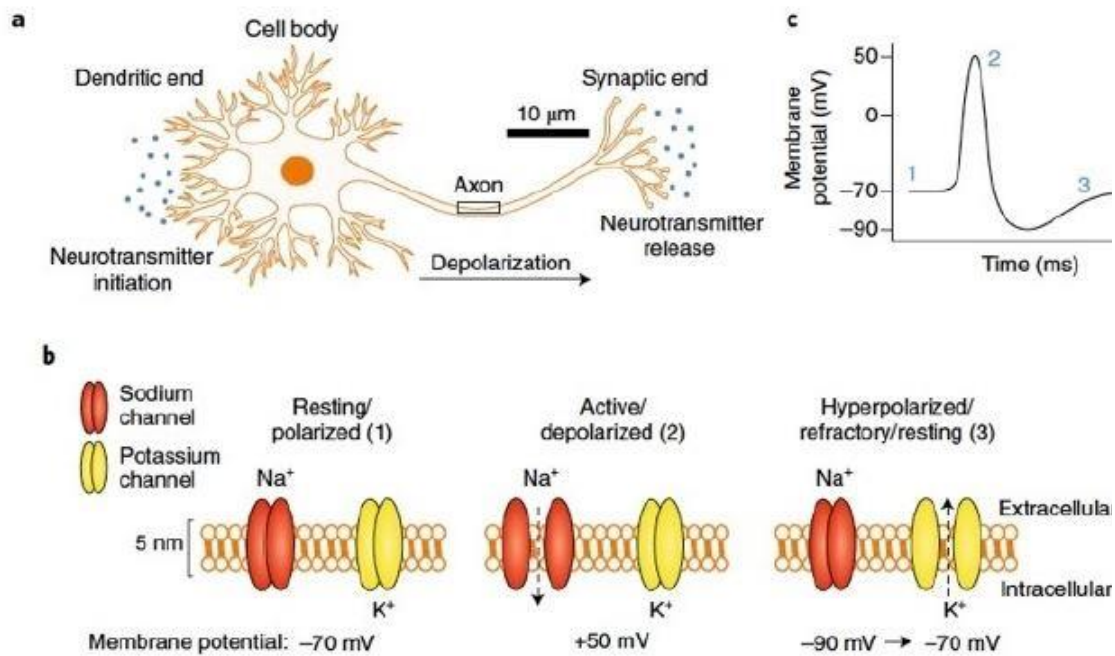


Figure 2.5 - Schematization of the action potential at three perspectives: a) Reception of signal by the dendrites, proceed through the action potential and delivered at the synaptic end. The arrow shows the direction of the AP along the axon; b) Graphic of the three phases of mV -depolarization, repolarization and hyperpolarization; c) schematic voltage-gate ion channels dynamic at the same three phases, exhibiting the membrane potential values.[19]

2.1.3 Membrane electrophysiological proprieties as an approximation of the electrical circuit

As an alternative approach to understand ions flow across the membrane, Hodgkin and Huxley compared electrical components to the electrophysiological properties of the neurons membrane, and represented them in a simpler electrical circuit by developing an equivalent circuit model characterized fundamentally by their resistance and capacitance properties, Figure 2.6.

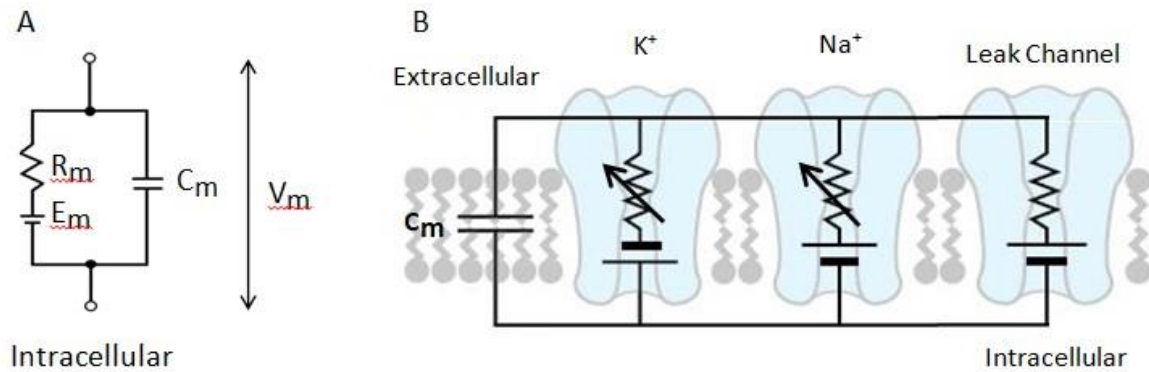


Figure 2.6 - Equivalent electrical circuit of the membrane. [1]. A) Simplification circuit comprising: resistance R_m , electrical motive force E_m and capacitance C_m . B) Same circuit applied on the neuronal membrane, which includes Na^+ K^+ and Leak channels. The latter channel refers to leak channels representing other remain channels, for question of simplicity.[17]

The equivalent circuit is fundamentally composed by resistors R and capacitor C ; therefore referred as RC circuits, are well known in electronic and widely used in neurophysiology. They provide an intuitive and quantitative description about how neural component affect the variation of the membrane potential variation. which considers: 1) the insulator property of the lipid bilayer and accumulation of different charges on the two sides of the membrane, completing the description of a capacitor, $C_m = Q/V_m$; and 2) the fact that the ions channel in the membrane grants passage to ions towards opposite side in a limited rate; thus it confers resistance to the flux of ions through the membrane.

It should be noted that each type of ions has its own reversal potential; therefore, their dynamic is affected by their respective ion channels permeability, which is represented by a resistance, disposed in the circuit in parallel with each other as well as with the capacitor representative of the lipid bilayer. Furthermore, each resistor is followed in series by a battery representing the electrochemical gradient impelling the ion motion through the ion channels. In order to simplify this electrical circuit we may resort to Thévenin's theorem. It enables reducing the multiples resistor and batteries from the different ions channels into only one resistance and membrane battery, denote as the membrane resistor R_m and electromotive force E_m respectively.

Moreover, when injected a positive current, the amount of time response necessary until the membrane potential rises and reaches the steady state response by describing an asymptote, is nominated as time constant, τ which is mathematically defined by the product of the capacitance and resistance, $\tau=RC$. Considering that the time of response is affected by the ability of the membrane to accumulate charge changes over time (depending on its capacitance) as well as by the quantity of ions flow crossing the ions channels, in other words by their lack of resistance.

Attending the relationship between the charge, capacitance and potential defined as $q = C_m V_m$ and considering its variation along time, it is possible to deduce equation (3) which relates the capacitance to the current I . Since I is mathematically defined by the time

derivative of the charge, it can be described as:

$$\frac{Q}{\Delta t} = c_m \frac{\Delta V_m}{\Delta t} \quad \Leftrightarrow \quad I_C = c_m \frac{\Delta V_m}{\Delta t} \quad (3)$$

Where I_C is the capacitance current, V_m is the membrane potential and c_m the capacitance per unit area.

The driving force, ΔV , of a determinate ion to crosses through the ion channel, is given by subtracting the potential from its electrochemical gradient to the potential membrane ($V_m - E_X$); therefore when those are equivalent the driving force is null. Taking into account that the conductance, \hat{g} is the inverse of resistance; using Ohm's Law and solving equation (4) for the ionic current I_R , one can write:

$$\Delta V = V_m - E_X = IR \quad \Leftrightarrow \quad I_R = \frac{V_m - E_X}{R} = \hat{g}_X (V_m - E_X) \quad (4)$$

Kirchhoff's current law previews that the sum of all current within a circuit is equal to zero. Hence applying it to the equivalent circuit model it would give the sum of capacitance current I_C , ionic current I_R and the current source $I(t)$:

$$I_C + I_R + I(t) = 0 \Rightarrow c_M \frac{\Delta V_m}{\Delta t} + \frac{(V_m - E_R)}{r_m} + \frac{I(t)}{A} = 0 \quad (5)$$

It is worth notice that, the electromotive force E_X , can be calculated by the Nernst equation (1) which does not depend on the number of a determinate ion channels type in the membrane. Hence, supposing that in each unit area there are N_X ion channels, both specific membrane conductance and resistance are express per unit area and are given by $g_X = N_X \hat{g}_X$ (S/cm²) and $r_X \equiv 1/g_X$ (Ω.cm²) respectively. Usually the current source is not expressed per unit area and it is therefore needed to divide it by the total surface area of the neuronal membrane, A . Additionally R from E_R denotes the summation of the cell's resting potential of all ionic channels; the same applies to the resistance as specific membrane resistance r_m .

So far, passive properties of the cell membrane have been analysed as isopotential where the membrane potential is equal in all extension. However, considering that neurons have extensive arborisations, the propagation of the current differs due to the variation of their capacitive and resistive along their extension; also depending on their dimensions and geometry [16]. The cable model ponders those variations describing the spatiotemporal evolution of the membrane potential $V_m(x, t)$ along the cell. It resume mathematical expressions which relies on an electrical circuit shown in Figure 2.7 similar to the equivalent circuit model, with the difference that it takes into account the propagation of the axial current flow longitudinally to the cell membrane; that denoted the resistances in series along the axon.

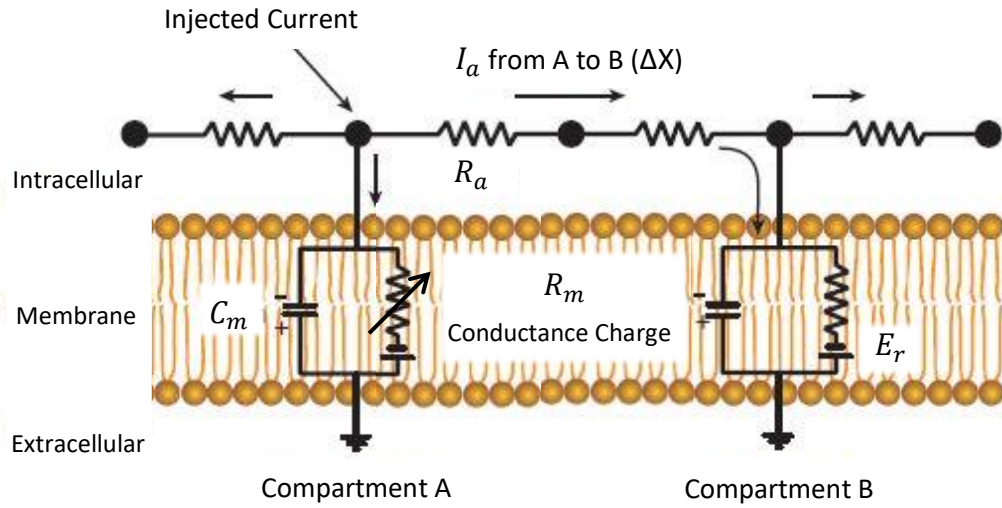


Figure 2.7 - Representation of the equivalent circuit for possible uniform cable equation. C_m ; R_m - membrane capacitance and resistance, respectively; and R_a , I_a - Axial resistance and current, respectively. ΔX - dislocation of current in space [2].

Contemplating the neurons shape being similar to a long cylinder, where the longitudinal extension is greater than the diameter, the flow is considered to propagate in only one spatial dimension. As a result, the membrane potential depends only on the length of the cell, ignoring the radial or angular component [17]. It is worth noticing that the length of the current flow, ΔX , is proportional to the resistance in the cytoplasm and inversely proportional to the radius a of its cross section (πa^2). Therefore, the axial resistance R_a is given by $R_a = r_a \cdot \Delta X / (\pi a^2)$, where r_a is the specific intercellular resistivity. The extracellular conductance is considered to be much higher when compared to inside the cell, thus the extracellular resistivity is established as zero. This assumption, however, is not always accurate if considering a more restricted extracellular volume.

The cable equation is partial derivative equation of the infinitesimal cylindrical compartment of the cell based on the compartment model. It depends on following parameters: the axial resistance R_a , membrane resistance R_m ($R_m = r_m / A$) and conductance C_m ($C_m = c_m / A$); where, r_m and c_m are the specific resistivity and capacitance of the membrane, respectively; and the A is the area of the membrane surface given by $A = 2\pi a \Delta X$.

Attending to equation (5) describes previously that relates the membrane current $I_m(x, t)$ with the resistance and capacitance, as a starting point, it is possible to solve the same equation to apply the specific and membrane resistivity and capacitance,

$$I_m(x, t) = 2\pi a \Delta x \left(c_m \frac{\Delta V_m(x, t)}{\Delta t} + \frac{\Delta V_m(x, t) - E_m}{r_m} \right) \quad (6)$$

On the other hand as derivation of equation (5), following Kirchhoff's law, $I_m(x, t)$ is also the sum of axial current I_a on different point in the cable ($I_m(x, t) = I_a(x + \Delta X, t) -$

$I_a(x, t)$). Note that the direction of the current is positive when the direction of the flow is towards the increasing Δx

$$I_a(x, t) = \frac{\pi a^2}{r_a \Delta x} (V_m(x, t) - V_m(x - \Delta x, t)) = \frac{\pi a^2}{r_a \Delta x} \Delta V_m(x, t) \quad (7)$$

$$I_a(x + \Delta x, t) = \frac{\pi a^2}{r_a \Delta x} (V_m(x + \Delta x, t) - V_m(x, t)) = \frac{\pi a^2}{r_a \Delta x} \Delta V_m(x + \Delta x, t) \quad (8)$$

Notice that the equation (9) is the reformulation of equation (7) and (8)

$$I_a(x, t) = \frac{\pi a^2}{r_a \Delta x} [\Delta V_m(x + \Delta x, t) - \Delta V_m(x, t)] = \frac{\pi a^2}{r_a} \frac{\Delta^2 V_m(x, t)}{\Delta x} \quad (9)$$

Associating both definition of $I_m(x, t)$ (7) and $I_m(x + \Delta x, t)$ (8) at the final cable equation (9), dividing by $2\pi a \Delta x$ and reorganizing the component, one obtains Eq. (10) where additionally it is possible to simplify by applying the definitions $\tau_m = C_m V_m$ and $2 = ar_m/2r_a$:

$$\begin{aligned} r_m c_m \frac{\Delta V_m(x, t)}{\Delta t} + \Delta V_m(x, t) - E_m &= \frac{ar_m}{2r_a} \frac{\Delta^2 V_m(x, t)}{\Delta x^2} \Leftrightarrow \\ \Leftrightarrow \tau_m \frac{\Delta V_m(x, t)}{\Delta t} + \Delta V_m(x, t) - E_m &= \lambda^2 \frac{\Delta^2 V_m(x, t)}{\Delta x^2} \end{aligned} \quad (10)$$

A sequence of five articles published in 1952 earned Hodgkin and Huxley a noble Prize in Physiology and Medicine [20-24]. They unveiled proprieties of the potential membrane and the related ion channels conductance. Through their experiences perpetrating on axon of a giant squid, they provided experimental data, in the first four articles; as to the final one, it formulates the theoretical framework which fundamentals the modern perspective of neural excitability. Notice that the biochemical constitution of cellular membrane was not clear at that time, yet Hodgkin and Huxley were able to empirically explore the ions dynamics across membrane resorting to intracellular recording, in which they understood that the conductance of ions are not constant.

The Hodgkin-Huxley (HH) equation describes below (12) alludes to the expression previously described in Eq. 5, as the second members of equations are both a conjunction of I_C (Eq. 3) with I_R (Eq. 4). However, this equation (12) is more elaborated so it is able to handle with the variability of each ion channel conductance as a function of the time and voltage applied at membrane. Moreover, they also distinguish Na^+ and K^+ channels as active part of the membrane since they are voltage dependent, in opposition to the capacitive current and leak ion channels parcels which are considered as a passive part of the membrane.

HH attributed the voltage dependence to a “gate particle” that in a stochastic manner

causes membrane to be more or less permeable to ions. This dynamic can be easily represented through a relation similar to a first order chemical equation where: closed \rightleftharpoons open. Since the channels does not open or close instantaneously: α and β coefficients are considered as the transition rates, i.e. number of times per second that a gate opens or closes, respectively.

Establishing \bar{g}_{ion} as the maximum conductance of a determined type of ion through the membrane, HH further proposed that membrane conductance would only reaches its maximum depending on the permeability regulated by the activation and inactivation gates; which in turn, is modulated by voltage. This 'gating variables' (n , m and h), represents the portion of open gates of a determinate type of ion. Hence, based on the experimental measurements, HH defined ion channel type conductance, $g_K = \bar{g}_K n^4$ and $g_{Na} = \bar{g}_{Na} m^3 h$, where each gate variables is raised to exponent representing the number of independent events necessary to open the variable gates (for example, neurotransmitter bonding to channels ligands). This is that described by the following equation:

$$I = C_m \frac{dV}{dt} \bar{g}_K n^4 (V - E_K) + \bar{g}_{Na} m^3 h (V - E_{Na}) + \bar{g}_L (V - E_L) \quad (12)$$

Furthermore, HH assumes α and β coefficients shifts instantaneously along with voltage, although that does imply an instantaneously change on the variable gates. Hence the rate the gates follow the g the α and β coefficients, is formulated:

$$\frac{dX}{dt} = \alpha_X (1 - X) - \beta_X X, \quad X \in [0,1] \quad \text{where: } n, m, h = X \quad (13)$$

2.2 Microelectrodes

The cell theory was already accepted in the middle of the 19th century, stating that cells are the basic unit of all living organism. However, the cellular organization of the neuronal tissue, at that time, remained far to be enlightened. Most neurologists defended the Reticulum theory, as the cell bodies observed in nervous systems were integrated in a continuously protoplasmic cell nerve, like a unique giant cell network or reticulum. With technology available at that time, it was hardly possible to have perception of neuron or nerve pathways. Not until Camilo Golgi developed the staining method of a limited number of cells in the nerve tissue, it was not possible to disclose the entire nervous cells morphology. Even though, Golgi endured as a proponent of the reticulum theory.

Employing the same method, Santiago Ramon y Cajal performed a finer observation of the neuronal architecture. Cajal, conversely defended the cell theory was suitable for nervous system and raised the neuron doctrine still applicable today. The invention of Golgi stained method and its masterful use by Cajal earned them, in 1906, the Nobel Prize in Medicine. Early in 1897, Sir Charles Sherrington demonstrated the electrical signal communication between neurons or neurons with other cells providing support for the neuronal doctrine. However, only later on in 2007, with development of electron microscopy, providing a resolution with a scale

of nanometres was possible to confirm the gap between neurons, featured by a distance of 20-100 nm. [1].

The continuous evolution of new techniques and technologies is crucial to accompany exiting and new hypotheses in neuroscience as well as to increase the rate of its development and increasing speed of discovery.

Electrical signals are the main source of communication within neuronal networks. Those signals can be described by their magnitude, sign, direction, existence and temporal dynamics; which all of them convey valuable information. The extents of these descriptions are restrained by the instrumentation and the data available, and therefore the record of neuron activity with high spatiotemporal resolution, still remains a challenge [25]. As a consequence of the lack of information, underlies the complexity of the neuronal system [4]. To overcome this problem, it is required to evolve practical methods to solve principles of neuronal coding, decipher functional connectivity among the brain regions, as well as understand the mechanisms of electrical signal propagation [26].

Nowadays the ideal microelectrode is yet to be produced; due to the necessity to compromise some parameters to guarantee the quality of others, for instance: between biocompatibility of neuronal cells and the quality of the signal recorded.[9] . The continuously pursue of the ideal interfaces between the nervous system and electrical sensors, lead to a vast range of different types of microelectrode. This allows a vast choice when selected accordingly with the investigation objectives. They can be categorized variously, addressing to their different features: shapes, materials or location relatively to the electrical source; as much as their invasion degree; either they are used in *in vitro* or *in vivo* experiment.

2.2.1 . Measurement of electrical neural signals

Traduce the flow current from neuronal membrane to electronical signals, is the transversal function of all microelectrodes. Signals recorded by microelectrodes reflect voltage deflection originated from transmembrane currents; that causes neuronal events such as action potential, also referred as a spike. Each spike occurs within few milliseconds (~0.5-2 ms). This time frame also take in account the refractory time of the Na⁺ channels [2], which reflects on a maximum spikes frequency of 500-1000 Hz [3]. However, these frequencies are not yet coherent in the literature, once the neuronal spiking rate might be higher. There still is a debate about how the information between neurons is encoded, either by their firing rate or by the precise time of the spike[4] The firing frequency is highly variable depending not only on the type of neuron that is firing but it is also modulated by external stimuli or internal proprieties of each neuron[5].

The analysis of the signal recorded also relies, fundamentally, on the signal selectivity of the neural activity of interest among other signals; as well as the sensitivity to perceive slightest fluctuations in the membrane potential. Neural activity signals are characterized no more than 80-100 mV (depending on the distance of the microelectrode to the source) [6]. Within this scale, the signals of interest are easily buried among noise, either originated from biophysical

noise or anthropogenic noise [7].

Therefore the interface between electrode and biological medium are been developed in order to maintain the signal-to-noise ratio (SNR) not less than 5:1[8]. It should be note that SNR is inversely proportional to the impedance of the electrode; which in turn, is also inversely proportional to the recording site's size. Furthermore in order to obtain better quality of the signal recorded from electrode; they are often proceed through the signal processing such as amplification, filtering and digitalization.

It should be noted that the longer is the distance between electrode and the source, less informative will be the signal, considering that the amplitude scales of the current, at some point in space, scales is inversely compared with distance from the source. Moreover the accumulation of other interfering signals lead to the spatial averaging [9]. In terms of space resolution, depending on the technique resorted the signalling might be analysed from different scales: from microscopic level which permit to address to the single neuron inner mechanisms; until macroscopic level allow an understanding in the general neuronal architecture.

Those might be achieved depending on the techniques resorted, approaches and analyse the signals at different scales, shown in Figure 2.8.

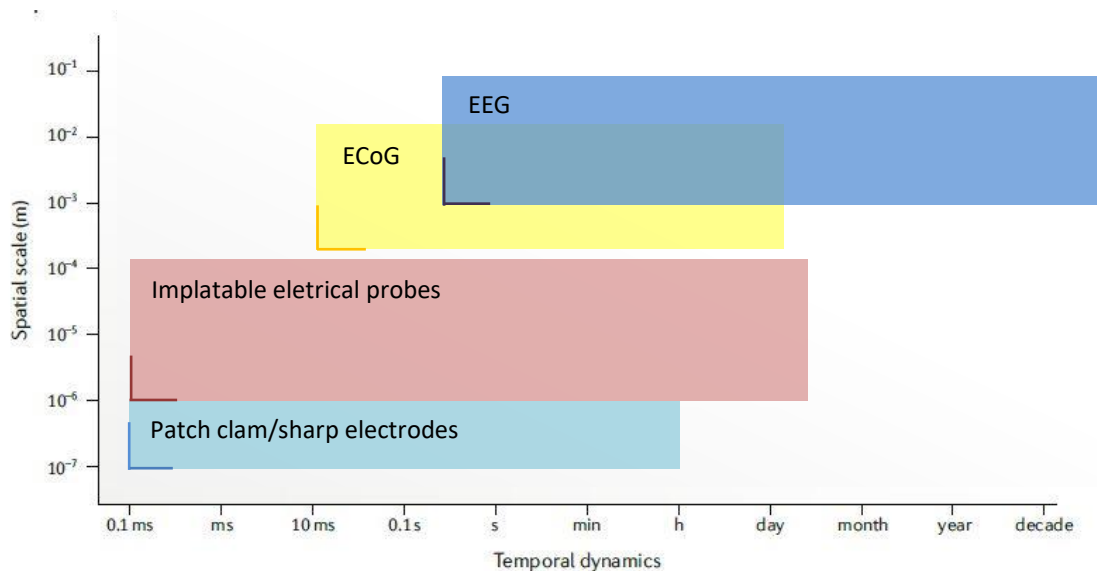


Figure 2.8 Graphic of spatiotemporal resolution of the different techniques used to record neural activity. Each technique corresponding shadow box exhibits spatiotemporal range as the solid lines demonstrates the spatiotemporal resolution. Adapted from [7].

2.2.2 Types of electrosignals from neurons

Single unit recordings provide measurements of neuronal events from single neurons, therefore requires the use electrode with a considerable high spatial resolution. These recording might either be intracellular (such as patch clamp) or extracellular level, they are capable e to detect current sub-threshold events at the single cell [4]. However since each neuron signal is subjected to interferences mostly at extracellular recordings, it is still a

challenge to record this type of signal in the long term [26].

Up to a certain limit, the overlapping signals from various neurons can be resolved by their amplitudes and AP waveforms. In order to improve this spike sorting, more electrodes are added in the extracellular space allowing to organize spikes of multiple neurons through triangulation, provided by the different distances from each signal and the various electrodes and identifying their neuron of origin; otherwise, this set of recorded signals are termed multiple unit record.

As the close-neighbour recording improved it enable to perceive signals from a larger spatial scale, referred as local field potential (LFP) signals. Those signals reflect a superposition of neural activity and they are affected by the synchrony of post-synaptic and transmembrane current as well as spatial density [27]. However, they are mostly composed by low frequencies, instead of high frequencies characteristic of action potential. That occurs due to the fact that high frequencies tend to filter and attenuate along the extracellular space [28].

At most macroscopic side there are the signals recorded by electroencephalogram (EEG) and electrocorticography (ECoG). As less invasive microelectrode, they are able to perceive synchronous post-synaptic AP signals, mostly comprising by LFP originated from pyramidal neural cell localize on the outer layer of the brain. Although the inner layers also contribute, the signals are prone to be partially refracted through different cranial layers until it reach the electrode. Also, EEG electrodes are subjected to interference from environmental or biophysical activity.

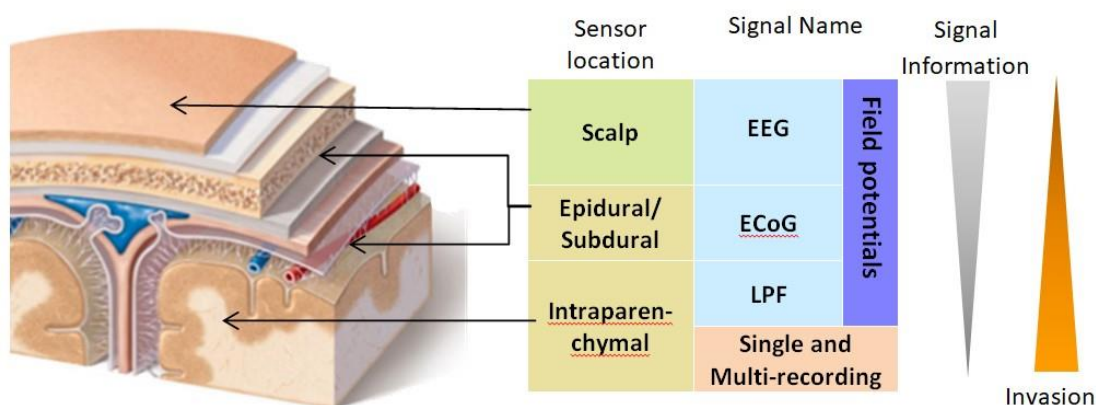


Figure 2.9 - Schematic illustration of different types of electrosignals of the brain. Image adapted from [29] and [30]. Copyright 2008, Elsevier.

2.2.3 Extracellular recording

Intracellular recording are more sensitive, as they can easily detect any neural activity; however it is always related with cell damage, as it is a more invasive methods, demanding a more delicate manipulation. On the other hand extracellular measurements are able to perform long term recordings but are more susceptible to recording interferences. Moreover the AP recording diverge, depending on the position of the electrode, both in amplitude (which is

higher in intracellular records) and in the shape of the waveform (since it depends on the exact geometry and position of the electrode) [31]. These two possibilities offer different advantages which are selected depending on the objective. In the present work the focus is deposited on extracellular measurements.

Electrical current of the membrane are not limited to the neuron; instead, they propagate through ions in the extracellular space. Extracellular currents are originated by AP, synaptic inputs as well as other electrically active events. Attending to Ohm's Law, the propagation of these currents along with the resistive features of the intracellular space, creates fluctuation of potential over time in the extracellular medium [32]. Hence, for extracellular recording, the electrode perceives the electrical diffusion caused by the ion flow. During the action potential the cell created ionic currents into two directions. As the ion flow moves towards inside the cell (depolarization), there is a drop on extracellular tension, and the electrode record a negative spike that is consequently mentioned as current sink; as ions flow outside of the cell (hyperpolarizing), positive spike are produced referred as a current sources.

For instance, considering a simplified picture derived from volume conductor theory, where the electrode is placed extracellularly, at some point near to an isolated axon; as the action potential passes by, the fluctuation of membrane potential recorded can be considerate as triphasic: as the depolarization approaches the current at the closest membrane region underlying the electrode flows outward from the membrane causing a positive deflection on the recording potential; as the depolarization reaches the closest membrane region the current flows inward to the membrane causing a negative deflection; finally, as the depolarization is flowed by an hyperpolarization, the electrode records once again a positive deflection on the membrane potential. It should be noted that the potential recorded is the result of the comparison of the electrode adjacent do the neuron(s) relatively to the reference electrode.

The quantitative relationship between the current source and the potential variation takes into account Maxwell's equations and it follows the volume conductor theory, where the extracellular field is taken as a certain volume with uniform conductance. The electrode placed at some point $r = (x, y, z)$ in the extracellular space, is able to sense variations of potential φ through time. Also, the transmembrane current I , from the electrical activity source at the point $r' = (x', y', z')$, is responsible for generating these potential variation. All these variables may be defined by the volume conductor theory,

$$\varphi(x, y, z) = \frac{I}{4\pi\sigma\sqrt{(x - x')^2 + (y - y')^2 + (z - z')^2}} \quad (14)$$

In Eq. 14 the conductivity σ is assumed to be independent of frequency and propagates equally in all directions, which holds a perspective which the extracellular space is characterized as an isopotential, where the resistance is uniform. However, this assumption does not quite correspond to the reality. The space between cells that comprehends the extracellular area is actually quite irregular and restricted; it only fulfills about 20 % of the

neuronal tissue. Therefore, not surprisingly, some resistance is involved, which is accompanied by potential differences across space in the extracellular field. Still, the volume conductor theory contributes for the development of biophysical forward-modeling method, which computes the physical field originated by known sources; and the comprehension of how various type of electrical activity relates with the recorded potential along the distance.

2.2.4 Interface between electrode electrolytes

In the contact point of a solid as an electronic conductor (i.e. electrode) and electrolyte medium such as the extracellular space, the transduction of electrical current from neuronal activity is established, through the equilibrium and distribution of ion charges. Assuming that the electrode is negatively charged, the water molecules in the surrounding, as dipoles, are redirected in depending on the electrode charge, comprising the first layer adjacent do the electrode's surface, known as hydration sheath. Next to the hydrated layer a solvated ions compose a second layer, whose limits are defined by Helmholtz planes. The two layers, referred as electrical double Layer (EDL), tend to assume a distribution as a cloud form with ion density gradient that increases progressively, which is also referred as the Gouy-Chapman diffuse-charge layer. Here, the signal transduction occurs, when potential variation causes charge redistribution of ions surrounding the electrode [33].

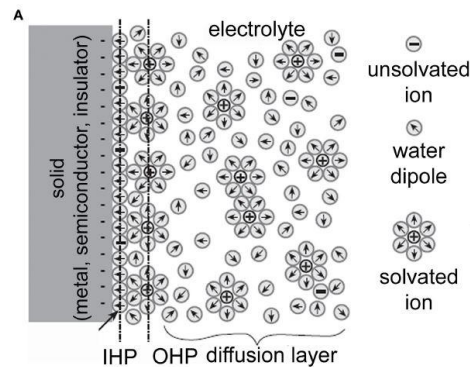


Figure 2.10 - Schematic illustration of ion distribution upon the contact point between the abiotic material and electrolyte medium. The circles with plus and minus signal represent ions positively and negatively charged particles respectively; and circles with an arrow represent water dipole. Moreover it is defined inner and outer Helmholtz planes are also defined. Figure original from Bockris and Reddy, 1977 and adapted from [33].

The electrical dynamic at the interface can be resumed through an electrode-electrolyte circuit model, similar to the equivalent circuit of the cellular membrane, exposed in the figure 2.6 A. This model includes the interface capacitance C_e which relies on the potential applied and the ionic strength of the medium; is represented in parallel with R_e denoting the charge transfer resistance. In series with $C_e - R_e$ follows a resistance; depending on the nature of the experience (for instance: *in vivo* or *in vitro*) this resistance is associated to the solution, R_{spread} ; or with the degree of the cell attachment to the recording site, R_{seal} Figure 2.6 B Often in this case different pairs of RC circuit are considered for each different portion of the

neuronal membrane. Referring to the membrane portion that is the junctional side to the electrode as (R_j and C_j) and non-junctional side (R_{nj} and C_{nj}). Additionally before the $C_e - R_e$ is denoted, in series, a resistance related to interconnections of the electrode to the following electronic; however it is negligible in materials such as metals although it is significant in organic conductors [33].

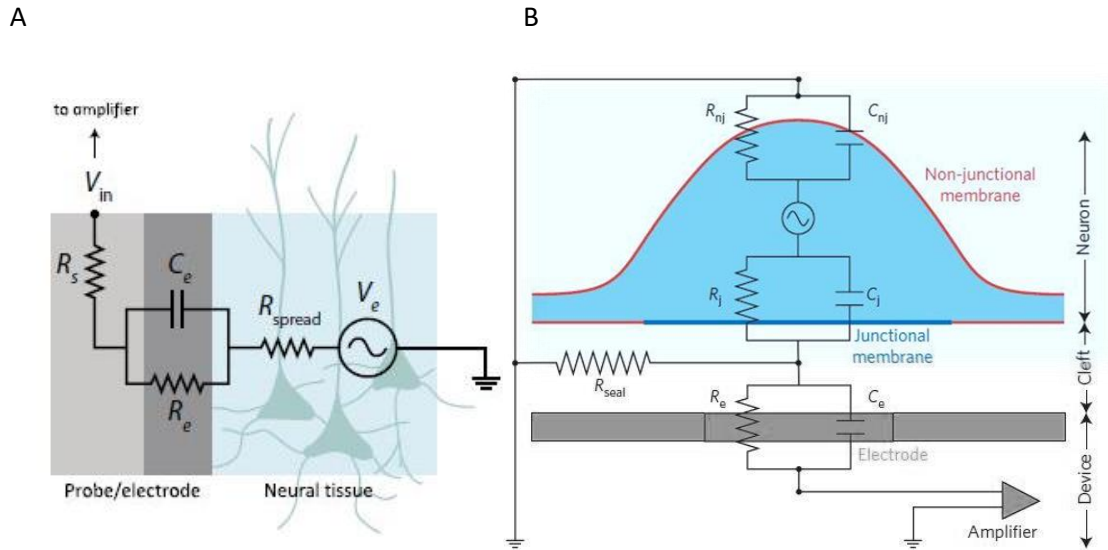


Figure 2.11 - Electrical circuit at two context A. Electrical circuit of the interface between the electrode and electrolyte [3]. B. neuron-electronic junction, where R_{seal} is considered [54]

Depending on the electrode type the nature of the current flow transduction can be Capacitive or Faradaic. The event of faradaic transition, which is associated to electrodes with non-polarizable materials and low resistance R_e ; implies an electrochemical processes i.e. reduction-oxidation reaction involving elements on the surface of the electrode [34].

Conversely, a capacitive transition is a characteristic of polarizable materials, usually selected for electrophysiology recording. They have higher resistance and therefore the current is more prominent on the capacitor path. As the ionic double layer goes through charge and discharge over the electrode surface, the accumulation of opposite charges depends on the potential applied and the concentration of ions at the interface. This is a chemical stable event where no substance is created or consumed. Moreover high frequency signal are well perceive through capacitive reaction conversely to low frequencies such as LFP [35].

However, it should be noted that the double layer capacitance can only be relate as linear when it is considered an ideally polarizable electrode; otherwise this capacitance rather behave as a constant phase element (CPE) [36]. Furthermore as the transduction process of the current flow through electrode is highly influenced by the impedance of the circuit, it reflects on the electrode output signal. Therefore, the CPE impedance, Z_{CPE} describes the ion diffusion nonlinearity as well as the electrode surface morphology. It yields an empirical relation with the interface capacitance described as [36]:

$$Z_{CPE}(\omega) = \frac{1}{Q(j\omega)^n} \quad (15).$$

where Q denotes the capacitance related to the EDL; ω is the angular frequency and n is the empirical measure of the inhomogeneity of the surface that range between 0 and 1; for instance if n is equal to 1, Q is comparable to an ideal interface capacitance [37]. Nevertheless, though the relation described by Eq. 15, as long as the capacitance at the interface is high the impedance is reduce.

The reliance of the microelectrode's output signal on the impedance as well as difficulty of sensing low-threshold signals, compromise the efficiency of recording neural signal. To address these issues, by taking advantage of the area-impedance trade off, one is able to achieve low impedance by increasing the area leading to low R_{spread} and higher capacitance. Large areas enable to measure low-frequency LFP signals, despite resulting into averaging the signal over a population of neurons. On the contrary, recording sites with reduced dimension entail higher impedance and thermal noise, but allows to record neuronal activity at the single level; and to perceive sub-cellular signals resolution [3].

2.2.5 Biocompatibility

The success of recording signal highly relies on the biocompatibility of the electrode. In contact with biological tissue, as the electrode is perceived by the organism as a foreign object causing inevitably a chain of biological reaction, leading to biochemical alteration related events on tissue-electrode. The damage not only affects the tissue itself but also the electrode integrity. Despite the increase in variety and enhancement in the last decades, no electrode so far is able to completely overcome their impairment with neuronal tissue [38]; therefore the development of electrodes focus instead, on maintaining their functions and bio-stability as long as possible [39].

The lack of compatibility is endorsed not only by chemical properties regarding the toxicity of the material but also due to the mechanics between the electrode material and biological preparation. For comparison purpose, the scale of material stiffness, Young's modulus (Pa) (Figure 2.5) demonstrates a fair contrast between various materials mechanical propriety. Electrodes that are composed by metal are characterized by high Young's modulus in the range of GPa. On the other hand the human body falls between 3-200 KPa; particularly, neuronal tissue in the range of 3 KPa.

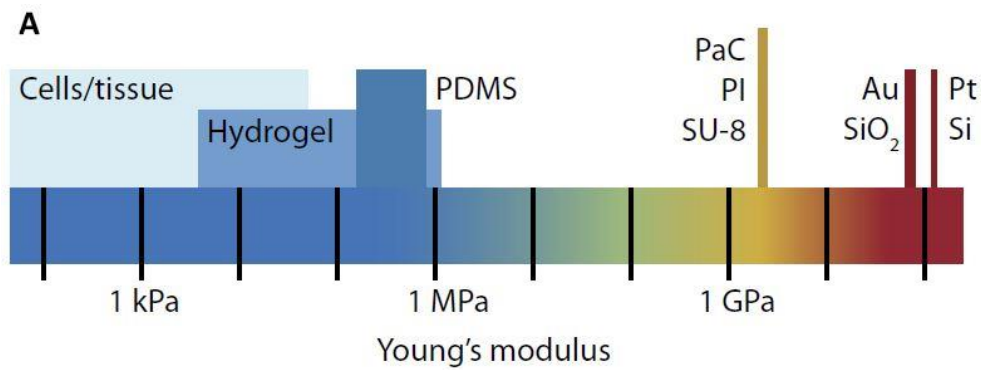
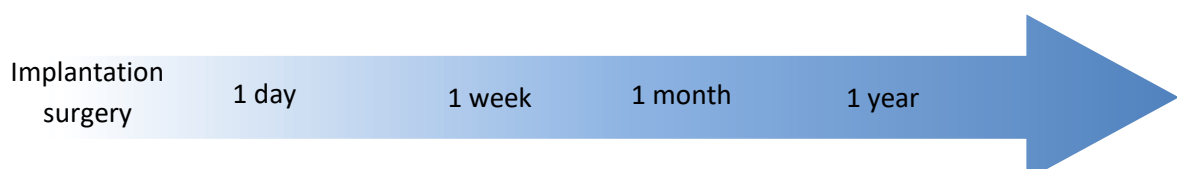


Figure 2.12 Young's modulus Scale. PaC denotes parylene C and PI - polyimide [3]

Early studies attend to the cells biomechanics, emphasizing cells as highly susceptible to the rigidity of their surrounds, independently of the biochemical environment. Furthermore this stiffness mismatch is more sensible *in vivo* experiments since it easily triggers FBR, [40]. Note that the brain is embedded in a medium called cerebrospinal fluid; hence there is some degree of micro-movement associated with the whole structure. This adds to the necessity of the electrodes to compliance and have certain amount of bendability and stretch ability [41].

As *in vivo* uses experience usually use more invasive methods, requiring electrode implantation, they evoke an acute response from the immune system followed by chronic response causing signal transduction degradation. The former response is mainly caused by the rupture on the vascularization which implies an open gap in the blood brain barrier (BBB); leading to the activation and migration of glial cell towards the insertion site and initiating the healing process which often undergoes through inflammation. The chronic response involves proliferation of astrocytes cell and encapsulation of the electrode. Both the inflammation and encapsulation processes entail negative consequences such as: rearrangement of the neuronal network, neuronal death, as well as increasing the tissue impedance obstructing the ion flow, leading to electrical isolation [35], (Figure 2.13). In general, wherein the experience is perpetuated *in vitro*, the environment is more controlled, albeit the viability of the neurons is more susceptible.



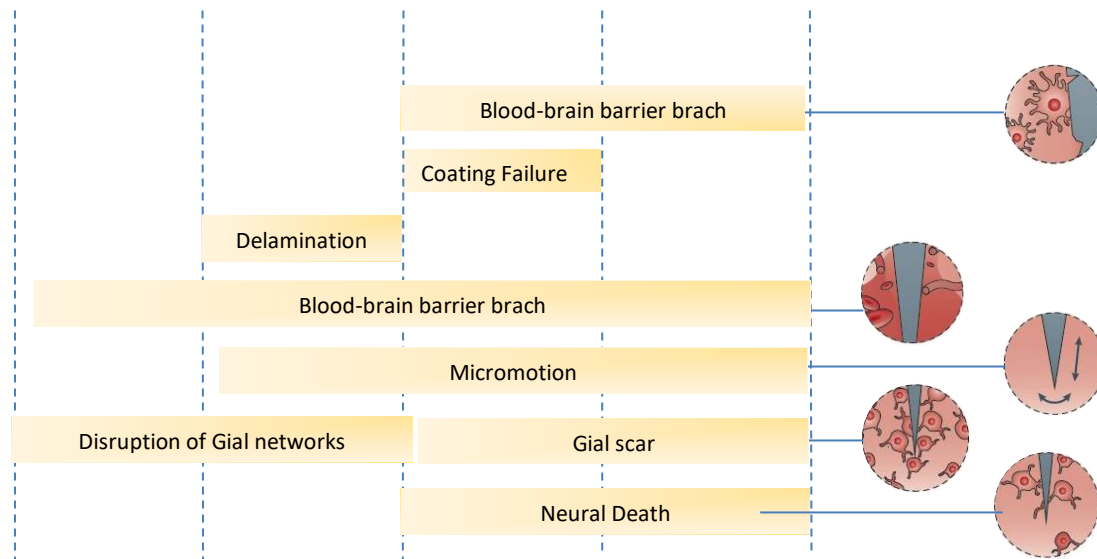


Figure 2.13 Schematic representation of the lack biocompatibility consequences and different foreign body reaction along time [81].

2.2.6 Material for Microelectrodes

Upon the selection of the material there are numerous factors to be considered: the electrode must avoid causing toxicity to the biological tissue, while maintain high conductivity as long as possible, as well as its integrity. Also, importantly, the saline-rich medium from biological preparations contributes potentially to corrosion of the electrode surface, where its ratio depends of the material selected. For instance, metals like tungsten and stainless steel would easily corrode, entailing its conductivity deterioration and production of toxic ions. Over time the exposition to the physiological environment also collects other possible consequences, such as the insulation layer is subjected to crack or dissolute due to the poor adhesion layer or mechanical stress. Moreover, the material also should considerate low thermal expansion coefficient during fabrication: in cases where inorganic materials, such as metals, are combined with polymeric films, the oscillations of temperature results on the material expansion which leads to mechanical stress. As another condition: low surface roughness should be considerate; in order to prevent formation of prominences and cracks in the most exposed layers which may evolve in delamination and further device failure. This may be achieved using deposition techniques such as spin-coating. Transparency is also an advantage, as it is convenient for microscopic observations. Materials as Indium Tin Oxide (ITO) or Graphene-based electrodes meet this requirement although it has been reported that these materials exhibit lower conductivity relatively to metal films [41].

Attending the electrode as a set, it can be roughly divided into the electrode itself and the

substrate. The primary function of the substrate is to support the electrode. Materials used in substrates can be separated into inorganic for example silicon, glass or titanium; or into organic including, among others: SU-8, parylene or silicone. Note that silicone includes PDMS with important properties, particularly elasticity. As for the electrodes, they are made typically with of metallic conductors, including: gold, titanium nitride, platinum and iridium as they presents high conductivity, biocompatibility as well as they are electrocatalytic but usually stable in air and aqueous solvent [42]. However mainly noble metal are often expensive and has tendency to form an oxide layer as result from corrosion [42]. Pure titanium oxidize easily in contact with physiologic tissue and therefore is rather used as an adhesive layer; Iridium has a high melting point which implies a more complicated deposition [43]. As an alternative, carbon materials follow the metals as the most used electrode material. They present numerous advantages: good biocompatibility, low cost and high chemical stability. For instance, graphene is highly attractive due to its mechanical strength, transparency and charge carrier mobility. The major drawback they present is lower conductivity when compared to metals [42].

Furthermore, the stiffness mismatch between the electrodes and body tissue is the main cause of electrode failure [44]. Therefore there has been an effort to build electrodes with more flexibility. Flexible materials based on SU-8, or Parylene are in the range of GPa; softer polymers such as PDMS and Hydrogels have more similar brain tissue rigidity. However they are not easily manufactured as it is difficult to conceive devices with those materials in ultra-thin layers. Additionally, too soft materials are also a challenge, since the electrode should not have the same stiffness as the brain structure as it is required to plot a straight path when inserted into the tissue. Associated with the electrode installation there is the risk of buckling (Figure 2.14), i.e. of bending the probe, which consequently leads to tissue injury and misplacement.

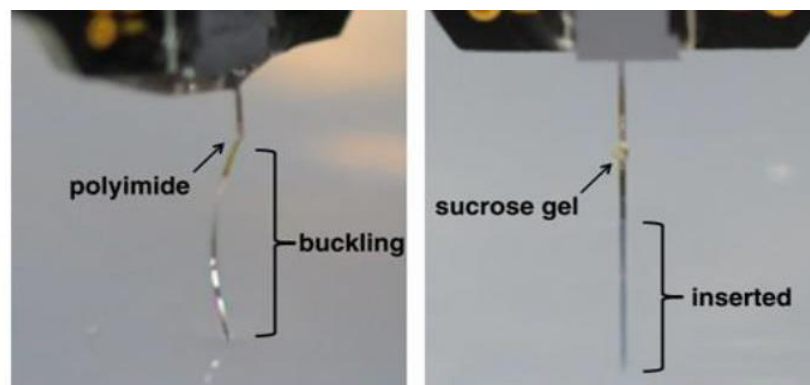


Figure 2.14 -Two images that allow to compare two electrodes, where at the image on right it suffer the buckling effect and in the right image the electrode has been correctly inserted. [5].

Conducting polymers and nanostructures (Figure 2.15) have been explored to apply on the surface of the electrode in order to improve the effective surface area of neuronal recording as well as reducing the immune response in long term applications.

Larger penetrating electrodes imply greater tissue damage; as an alternative to increase electrode dimensions, one could rather increase the electrochemical surface area over to the Geometric surface area; that is accomplished by introducing a thin film of micro and nano structures to alter either the porosity or roughness of abiotic\biotic interface. Nanostructures, such as carbon nanotubes (CNTs) or IrOx, TiN, Pt black porous material and nanowires (NWs) can improve considerably the surface area of the interface between the electrode and biological tissue [3]. This effect is also achieved by gold mushroom shape microstructure which will be explored in this work. Particularly NWs demonstrated results with low impedance recording and it is tolerable for neurons as they allow engulfment of the membrane and increase de SNR.

As another approach, electrodes are coated with conductive polymers (CPs) which enables a mechanical and chemical enhancement of the electrode performance. As CPs are able to assume nanotube morphologies or polymerize creating covalent cross-links with biomolecules and cells; diminishing the limits between biotic and abiotic interface. Materials such as polypyrrole PPy and PEDOT (3, 4- ethylenedioxythiophene) are commonly used due to their good conductivity and biocompatibility. Their elasticity conferred by the weak intermolecular bonding allows an easier adaptation to the electrode patterns. Additionally, for instance, combining PEDOT (as some others CPs) along with excess of poly (styrene sulfonate) PSS provides a higher ionic mobility and a more flexible propriety at the interface, contributing to increase volumetric capacitance as well as better biocompatibility [3]. Other combinations such as conductive metal with polymer nanocomposite like Pt/Au and AU/PDMS improves the reduction of impedance while electrode performance [41].

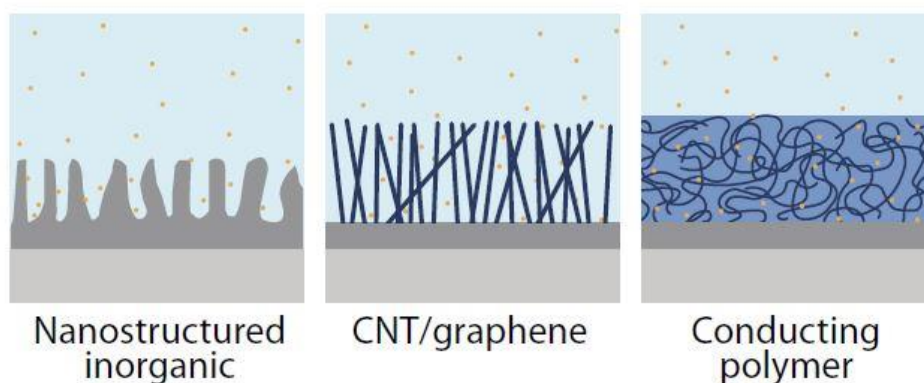


Figure 2.15 - Schematic illustration of different type of electrodes coating [3]

2.2.7 Micro Electrode types

Microwires, belongs to the first generations of microelectrodes. They often are a sharpened

wire with a diameter up to 80 μm , composed by conducting a metal (such as gold, platinum, tungsten, iridium, stainless steel, among others). The metallic microwire is involved by a non-toxic insulator material, excepting for the tips, since they are the recording site. Depending on the purpose of the experience microelectrode might be used as single-wire or microwires (in plural), commonly referred as tetrode (four electrodes) or multi-wires (up to hundreds of electrodes) (Figure 2.16 A). These electrodes are capable of enduring neuronal recording along a period of days. Nevertheless, it is worth pointing out that Williams et al developed a protocol that allows chronic recording, in awake animals up to five months [45]. Nicolas et al and Schwarz et al reported successfully recordings from a monkeys for 18 month and 5 years [46, 47] [48]. Note that this type of electrodes allows more freedom in assembly as they are relatively easily to fabricate and cost-efficient. Furthermore, their rigidity depends of the materials selected, although the stiffer is the microwire, the easier it is to implant it, allowing accessing deeper structures in the brain. Recently more flexible material has been used to improve biocompatibility, and therefore, the longevity as much as the functionality of the electrode. Yet, they have some disadvantages as they are prone to bending over during the implantation process, which leads to diminish the accuracy of recording location [49].

As the enhancement of recording techniques proceed, microelectrode arrays (MEA) become possible; along with microwires electrodes they are one of the most classical microelectrodes, but with the advantage that their introduction allowed to record up to hundred neurons simultaneously. Structurally MEAs are constituted by a substrate that supports patterned conductor lines, which are electrically connects an array of distributed recording sites to the recording equipment. Emerging lithography techniques promoted the development of devices with more diversified materials and reduced electrodes sizes. This enabled more recordings sites within the same tissue displacement amount. In the 70's, Wise et al. concurrently with Starr and Angel were pioneers in producing silicon-based microelectrodes; which led to well-known Michigan probes (Figure 2.16 B) [50]. They are design with multi recording site electrodes along the length of each probe which enables to record LFP, single and multi-unit signals from various layers on the cortex when implanted [38]. Two decades later on similar electrodes, called Utah electrode (Figure 2.16 C), were produced; these have an array of silicone shanks perpendicular to the substrate where only the tips are able to receive signals. These electrodes mainly address studies *in vivo*; they are the only probe that received the US Food and Drug Administration authorizations for chronic use in human. Although the conjunction with coating materials enables to enhance the biocompatibility and recording efficiency, those are always limited by the foreign reaction of the tissue eventually.

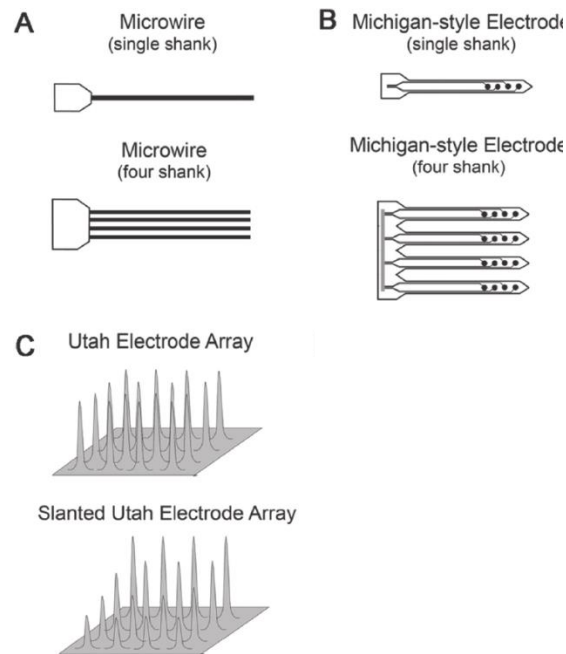


Figure 2.16 illustration and pictures of microwire microelectrode (A) illustration of single and a tetra electrode microwire (B) Michigan Electrode with single and tetra electrode microelectrode (C) Utah Electrode array [5]

To meliorate studies *in vitro*, planar MEAs were introduced, in parallel, by Thomas et al. at the beginning of 70's [51]. This type of MEA allows a non-invasive and a long term extracellular recording. Since it is a more controlled experimental environment recording, where either slices of the nervous tissue or dissociated cell are cultured *in vitro*. This permits to study the influence of materials biocompatibility, drugs and disease modelling in the neurons as well as their behaviour, activities and plasticity in a small network. Due to their non-penetrating feature, they do not induce cell or tissue damage, so in theory are able to endure longer electrophysiological record [52]. Nowadays this conventional electrode is broadly commercialized (Figure 2.17); they are integrated in a cell culture dish, where the substrate is preferably constituted by glass, as its transparency is convenient for posterior observation through microscopic optic. To facilitate the cell attachment of neurons cultures or slices of the neuronal tissue, the surface of planar MEAs is coated with laminin or polyline (protein involved in neuronal membrane adhesion) [9].

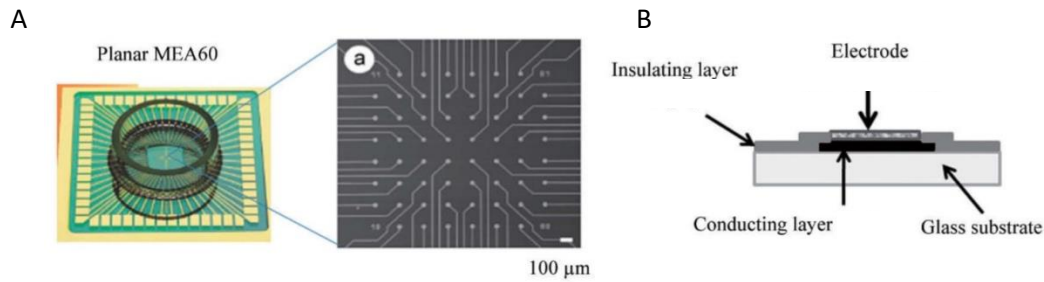


Figure 2.17 Picture of Planar MEA A60 and schematic illustration of a microelectrode array . (A) micro-image of the centre of the microelectrode (B) cross view of one electrode of the MEA. Modified from: Egert et al., Brain Res Brain Res Protoc, 1998 [82].

These electrodes are constituted by corrosion-resistive metals and covered by an insulator layer that isolates electrodes from each other; reportedly, the standard diameter of each electrode is about 60 μm. They are distributed in patterns of 8x8 or 6x10 on planar MEA, within a few mm [40]. The continuous development allowed the raise of multiplexed versions of MEAs which allows the reduction of the total number of conductors lines on electrode array [48], enabling the existence of smaller and denser MEA with more spatial resolution, which led to the ability to record higher frequencies and perceive APs. MEAs with 11,011 and 128x128 [53, 54] electrodes were successfully tested. However, due to the reduced electrode area, only a limited number of electrically active neurons are within the range of the recording site [10].

Although they are well established in the field for extracellular recording, 2D MEAs models presents important drawbacks relatively to 3D MEAs (Figure 2.18). For instance, due to third dimension functionality, it diminishes the impedance of the electrode due to the larger area contact.

Attending that there is a high resistance on the junctional membrane, thus only a fraction of the current that crosses the entire neuronal membrane is able to flow through the junctional membrane portion. Moreover, the junctional resistance R_j varies as a function of the ratio between the total neuronal membrane and the junctional membrane area. The area of the recording site is a malleable variable which depends on the geometry. Hence, the shape of the microelectrode is relevant for the good electrical coupling between the biotic and abiotic elements [52]. Attending to this, recently there is an increase on research that focus in developing three dimensional micro- and nano- structures such as gold nano-flakes, mushrooms, nano/micro-pillars and carbon nanotubes as well as platinum black or Ti_3N_4 porous layers, to improve the surface area without increasing the electrode area [9, 52].

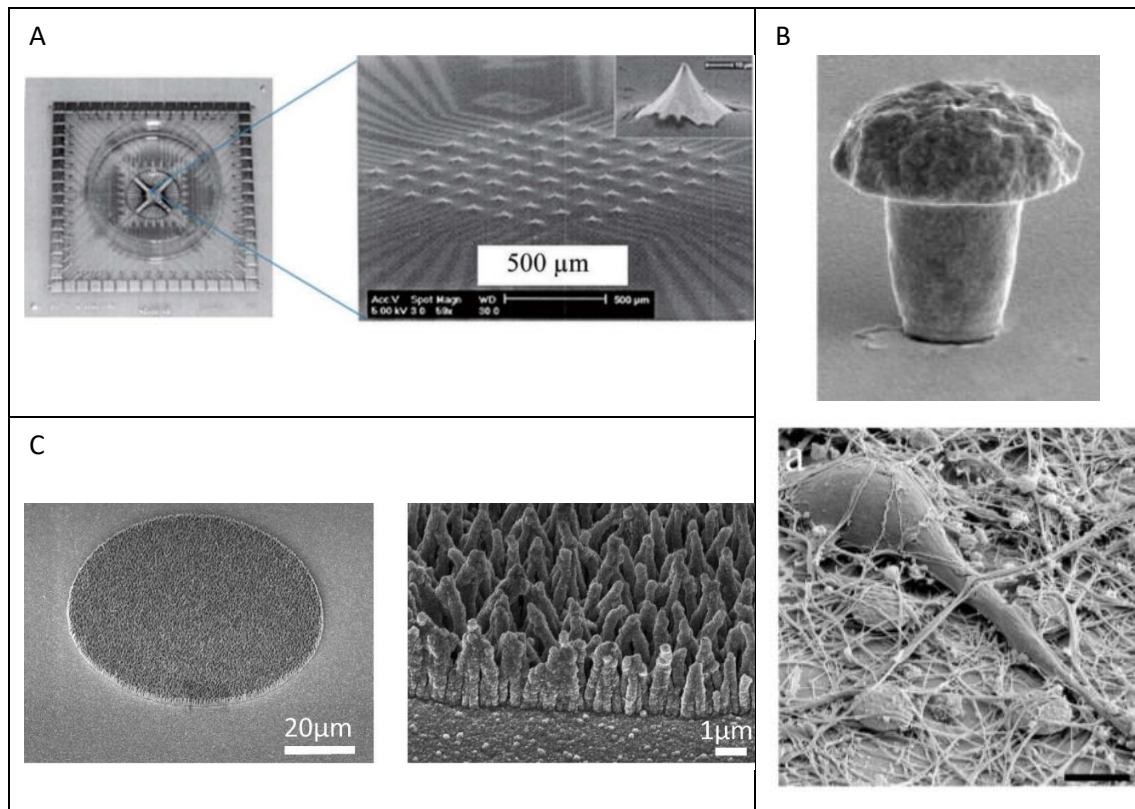


Figure 2.18 A 3D microelectrode where the centre expanded, with a picture of the structure at right up corner where the bar scales reads 10 µm. [55] Modified from A Heuschkel et al., J Neurosci Methods 2002. B picture of a mushroom shaped microelectrode at the top and more general view of a *in vitro* cultured neurons in mushroomshaped microelectrodes modified from Spira et al., 2015 [56]. C 3D-nanostructured boron doped diamond microelectrode modified from: Yvert et al, 2015 [57].

2.3 Microelectrodes for organotypic culture and *in vitro*

2.3.1 Organotypic culture among other cultures

Either *in vivo* or *in vitro* models are the most discussed for experiment process. The use of *in vivo* models favours the preservation of natural tissue structure and conservation of neural network organization and multiple cell types interactions are important aspects, regarding the viability and accuracy of results of electrophysiological and pharmacological experiment. Although it requires a surgical procedure which implies damage caused by electrode implantation; which leads to inflammatory processes that are more complex in these cases. Other drawback should be considered such as the amount of resources necessary for animal experimentation. In the other hand *in vitro* model offers a controlled environment and they represent a simple model (mainly 2D cultures) to investigate microelectrodes functionality or neuronal behaviour. Conventionally *in vitro* studies are conducted in two dimensions where the lack of the extracellular matrix and inherited cell mechanics, leads consequently to different recording and loss of detailed information. More recently 3D *in vitro* cultures have been

developed offering a mean to microelectrodes investigation. However the improvement in the physiological neuronal architecture resemblance 3D *in vitro* model still has some constrains, for example, physical challenges like oxygenation and perfusion of the cells [58] [44].

As alternative the organotypic culture (Figure 2.19) consists of *ex vivo* experiment, i.e., thin slices are extracted from the organ and further cultured *in vitro*. These structures enable the replication of *in vivo*-like conditions which are not featured *in vitro* experiments. In addition, they provide access and precise control of the extracellular environment, from a single animal yields several slices, which constitute an advantage towards ethical acceptability by respecting the principles of Replacement, Reduction and Refinement [44].

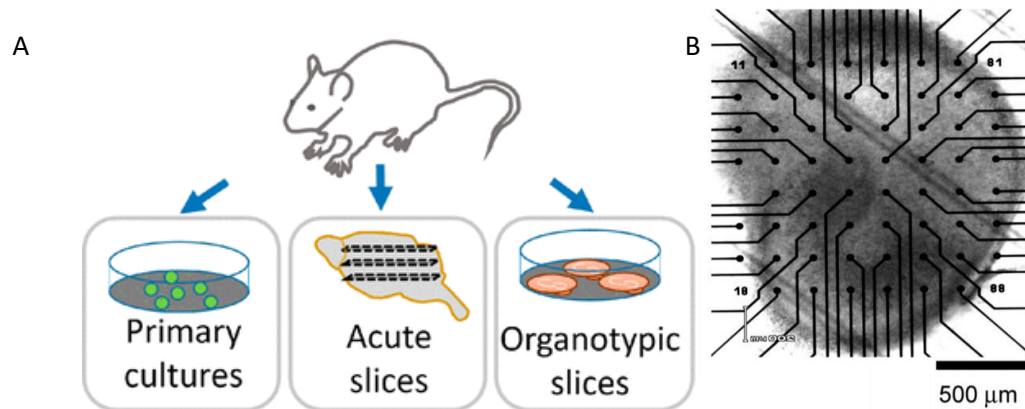


Figure 2.19 A. Schematic illustration of three type of cultures primary cultures *in vitro*, acute slices and organotypic slices [59]. B. picture from a hippocampal slice extract and transferred to a planar MEA [60].

Acute slices extraction from adult brains is one of the two types of preparation that can be performed. In this case, the slices are not cultured, therefore the preparation is simpler and required less maintenance. Although these exerts are limited by time due to the reduced amount of hours of viability, they provides a reliable insight of cellular and molecular mechanism that occurred *in vivo* before the harvest [11]. Acute slices are vastly used for electrophysiological recording, such as for investigation of synaptic plasticity mechanism [44, 58].

The second type of preparation, the *ex vivo* tissue is incubated for a longer period of time under controlled condition, so-called organotypic culture. For this purpose slices originated from neonate rodents are preferred, because previous to differentiation, in the early stage of neural connection with no elaborated synaptic network the tissue has superior capacity to regenerate from eventual lesions. On the other hand, slices derived from the adult brain are also used for investigation, although the more mature is the tissue used for the long term cultivation, the smaller are the chances of the cell surviving, therefore, it is a technique that still required to be optimized [11].

Organotypic cultures are subjected to mechanical aggression from the slicing procedure, which may result in the lack of nutrients and oxygen perfusion, causing death cells and tissue

debris. Comparing to the other cell types, the neurons are the ones more susceptible to the slicing procedure. Additionally, as a finite piece of the organ, the organotypic slice has a reduced circulation of immune cells and a lack of brain-blood barrier (BBB) which constitute a drawback in the foreign body responses studies [11].

The survival of cells in the organotypic culture depends on different factors, e.g. medium composition with growth factors and serum; the thinning of the tissue slice; the speed of the preparation and its sterility; health of the donor animal, as well as its age [11]. To maintain in good physiological shape, a support chamber might be required. It was first described, by Boyd et al. (1971) [61]. On the following decade, Gähwiler, B. H et al improved this technique and developed the roller tube technique, where the slice cultivated is immobilized on one side of the tube, which provided uniform aeration through its constant rotation [62].

This technique was again modified, by Stoppini et al. (1991) which used semipermeable membrane method for organotypic culture that provides, through culture inserts, a porous interface between the slices and the culture medium as well as humidified air, also ensuring the adequate oxygenation and nutrition by capillarity [63].

The dead-cell layer caused by the slicing is not only a problem in term of viability related to the release of intercellular component that may lead to neurotoxicity, but also in terms of electrical recording. The electrically passive layer formed mostly by inactive cells, at least in the first 50 μm from the extremity of the slice (Figure 2.20), which forms a barrier between the planar microelectrodes and the active cells in the inner layer of the slice. As result, the numbers of the neurons as well as the signal amplitude are significantly reduced.

However, has been stated that the use of organotypic slice culture can meliorate those difficulties. Due to their longer-term viability, necrotic cells have time to be eliminated and therefore remaining active cells migrate toward the extremity reducing the distance between them and the electrode [6]. Nevertheless microelectrodes, with a third dimensional functionality, are capable to sensing signal form neuronal pathway located at higher level on the 3D cultures models, hence they reveal to be more adequate for signal recording in 3D cell or organotypic cultures. For these reasons, several groups are investing their attention on 3D MEAs lately, in order to overcome technological challenges inherent to their microfabrication.

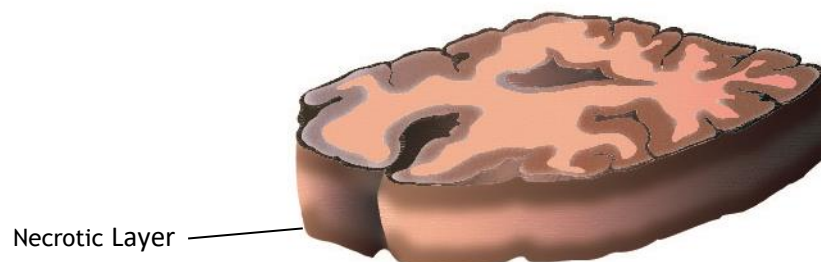


Figure 2.20 Schematic representation of brain slice where demonstrates the necrotic layer inherent to its extraction.

Although these microelectrodes are successfully fabricated and further applied on, most of first models these has a height less than $\sim 70 \mu\text{m}$. However, for organotypic cultures, it is

required taller structures in order to reach active layer of neuronal cells, beyond the damage.

Interestingly, the aspect ratio of the microelectrode is also an important characteristic that should also be considered. The higher is the microelectrode protrusion relatively to its width, less damage it causes during the insertion of microelectrode in case of organotypic culture. Moreover it provides a larger surface area of contact with the tissue without increase the volume of the electrode also contribute to improving the signal-to-noise ratio.

Where is being useful in several works such as in co-cultures investigation of functional regeneration of spinal cord in organotypic co-cultures [8]; as much as characterization of propagation of epileptiform electrophysiological activity [64].

2.3.2 Fabrication of high aspect ratio microelectrode

The list of microfabrication techniques it is been accumulating along time, nowadays, is almost as long as the different microelectrodes types list itself. Among them photolithography, e-beam lithography, dry etching and deposition are process often referred for 3D microelectrodes fabrication with high aspect ratio; mostly because of their compatibility with well-established material, such as semiconductor and metals (Au, Pt)[65].

All these processes can be roughly clustered in two categories: top-down, and bottom-up fabrication. Top-Down techniques are subtractive process that produce the desired pattern by means of removing selectively a portion of given the material; as for Bottom-up techniques, inversely, are additive process, which involve bonding individual units, such as particles or atoms, to shape the desired structure.

High density microelectrodes were developed resorting to deep reactive ion etching (DRIE) process, which enables that enable to build electrodes with approximately vertical walls, ranging hundreds μm depth, additionally, with a good surficial finish. However it should be noted, this approach is usually specific to silicon [66]. Nevertheless, like the first approach just mentioned, technique in both categories have their vantages and disadvantages, therefore they are, increasingly, used in conjunction, in order to come with creative solution to overcome their inherent difficulties. For instance, Kibler et al. [67]. was able to create high aspect ratio microelectrode, with 200 μm high and diameter of 20 μm , converging different approaches DRIE, wet etching, chemical vapour deposition and anodic bonding.

Additionally Spanu et al. has proposed a simple approach to fabricate 3D gold microelectrode with more than 100 μm resorting only to standard photolithography directly on the planar MEA surface [68]. More recently Rajaraman et al. successfully proposed a novel process using metal transfer micromolding technique producing 3D MEAs with 300-500 μm height for acute brain slices [69].

Again, the selection of the fabrication of the microelectrode should be firstly considered the objective of the investigation with the resultant product will be employ. However the ideal process would respect the following parameters: such as the capacity to fabricate directly on

planar microelectrode, the cost-effectiveness, the time consumed to be produce, their reproducibility as well as ability to manoeuvre materials that have high conductivity as well as good biocompatibility, such as metals like gold; high aspect ratio is also an important aspect. [70]

2.4 Perspective on the present work

The literature review compasses the theoretical framework referring to neural electrophysiology, providing the context necessary, for wide range of microelectrodes proprieties to cope with different challenges inherent of acquiring neuro-signals discriminated along this chapter.

There are extensive options of different types and forms of microelectrodes that can be selected, as already commented; it depends on the objective of the investigation in which they will be used; as well as their fabrication. Nevertheless there is some aspect that should be considered independently of the investigation: the efficiency and the biocompatibility of the microelectrode. Their proprieties should comprise high conductivity as well as should not evoke adverse reaction from the organic sample; influenced either by material, shape or stiffness of the microelectrode.

Microelectrode array have been widely used, they gather multiple recording sites enabling to receive data from multiple site simultaneously, within other advantages presented at subsection 2.2.7. Furthermore, is also mentioned that planar MEAs developed their ways into 3D microelectrodes add several advantages to neuronal recording, which are fundamental when considering 3D in vitro cultures. The highly recommendation of the use of high aspect ratio electrode due to their low impedance an improved biocompatibility in 3D cultures are explained in section 2.3. Further discussion of the different methods of microelectrode fabrication is displayed at subsection 2.3.2.

The ultimate objective of this work is to produce a 3D microelectrode, for either in vitro or organotypic culture. In which, the gold micropillars with 100 μm height, are constituted by a conjunction of long nanowires attached to the micropillar base. This specific structure allows a higher aspect ratio than a full block standard micropillar instead. To develop such microelectrode directly from a commercial planar 256 MEA 100/30iR-ITO, is proposed, in this dissertation, the use of template-assisted electrodeposition process; which comprise well established methods and is characterized as a convenient and simple process. Conversely, this process owns a major drawback which is the transference of template to the substrate. However once the condition for a practicable adherence of the template to the substrate are mastered, it will enable the batch production of microelectrodes. Therefore despite that was only possible to produce results until this point, due to the intrinsic challenge and time constraint, the possible reasons for the unsuccessful transference are discussed as well as possibilities to overcome this challenge.

Chapter 3

Material and Methods

3.1 Designing of the microfabrication process

Attending the main objective of this dissertation: develop a simple and convenient approach for 3D MEA array fabrication, characterized by high aspect ratio gold micropillar with at least 100 μm high; a microfabrication process were arranged, based on template assisted method. The manufacture of such microelectrodes relies, fundamentally, on two well-established techniques: aluminium anodization and electro chemical deposition. The illustration of the sequential procedure is depicted in Figure 3.1.

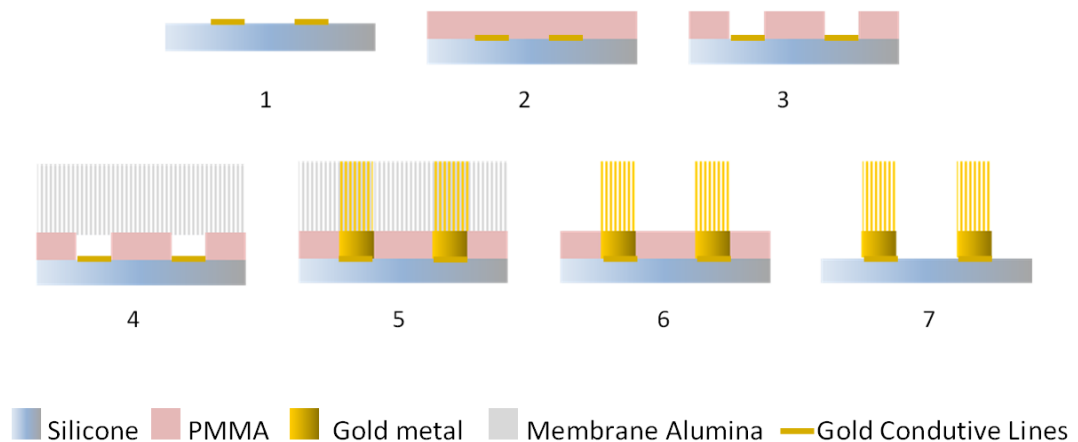


Figure 3.1 - Schematic illustration of the fabrication of micropillar gold electrodes, resuming the principal steps of the process: 1-3-common steps of photolithography (2-spin coating, 3-exposure and development for PMMA patterning; 4- template transference; 5- electrodeposition of gold; 6- template removal; 7- removal of the remaining PMMA.

In a more detailed description of the microfabrication process, firstly the surface of planar 256 MEA 100/30iR-ITO is coated with a 20 μm thick layer of PMMA photoresist by spin coating and patterned through photolithography¹, as it illustrate in Figure 3.1. 1-3. The pattern consist array of 16x16 distributed circles, with 50 μm of diameter and 100 μm spacing distance, corresponding to the recording site placement and dimensions. The mask design was produced in AutoCAD program; it is demonstrated in Figure 3.2.

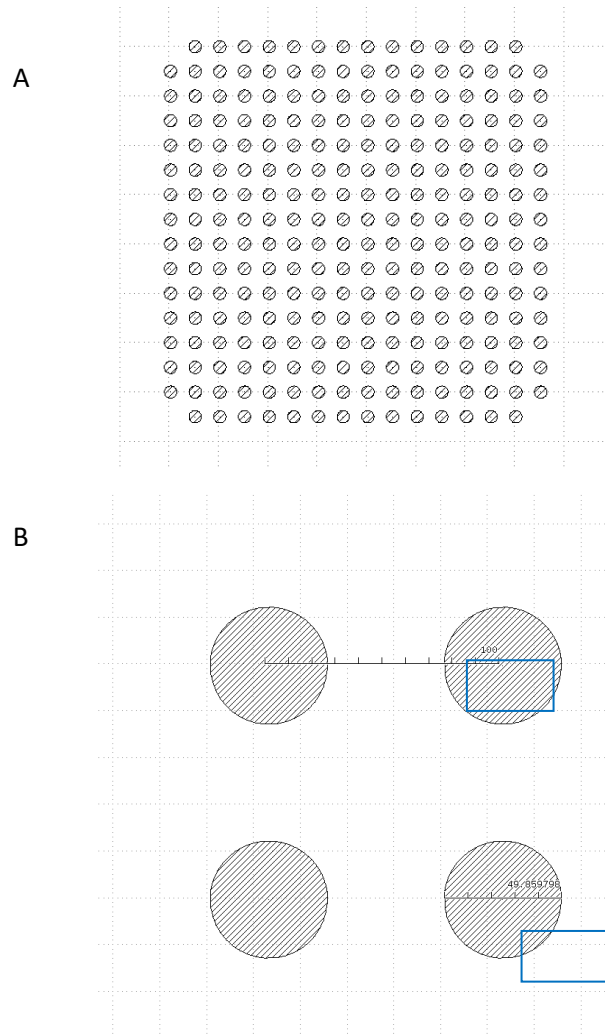


Figure 3.2 - Pictures of the mask produced at AutoCAD. A- General vision of the mask design featuring 16x16 circle array B - Demonstrates the diameter and intercore distance, in the figures reads 49,859798 μm and 100 μm respectively.

¹This method was not possible performed in this work, therefore despite it is include on the microfabrication design it was not it is not include on Methods Chapter.

Secondly, for the step depicted in Figure 3.1.4 is produce a porous alumina membrane to use as a template by anodization methods. The template is transferred onto the surface of the planar MEA. So that when performed the gold electrodeposition, which the step depicted in Figure 3.1.5, the formed the structures will assume the form of the template, represented in Figure 3.2. Further on the template is removed by chemical etching through alumina removal sodium hydroxide 98%wt (NaOH) at room temperature for 24h, in Figure 3.1.6. Finalizing by the removal of the poly(methyl methacrylate) PMMA with the acetone.

Notice that, before using the alumina template, the surface of the MEA has already cover layer a PMMA previously patterned by means of photolithography. This patterned layer presence before electrodeposition is important for two main reasons: it ensures that the original recording sites of the planar MEA are exposed, hence they are able to establish electrical contact during the electrodeposition; in other hand, it isolates the remains gold conducted lines, that connect the electrode site to rest of the recording equipment, on the MEA surface to prevent unrequited deposition.

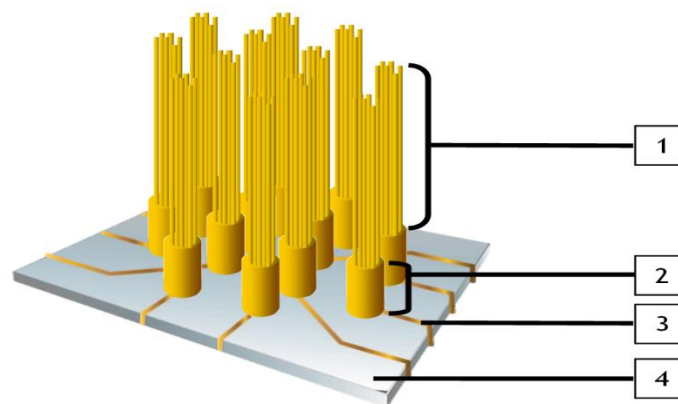


Figure 3.3 - Illustration of the central section of the final 3D MEA model design. 1- Nanowires form upon the bases; 2- Base, together with nanowires they for the micropillar; 3- the gold line conductors of the MEA devices; 4- the MEA substrate composed by Si

3.1.1 Template Synthesis by Alumina Anodization

Naturally, an oxide film forms on the surface of the metal due to its chemical instability in an ambient atmosphere, particularly, in contact with oxygen. In the case of aluminium, its oxidation is constituted by the exchange of aluminium (Al^{3+}) with oxygen (O^{2-}) ions at the metal-electrolyte interface; producing an oxide layer composed by alumina (Al_2O_3). At the pace that the oxide layer forms, the ions become out of each other reach, and as consequence, the rate of the chemical reaction is diminished. However, subjecting the oxide to an electric field, contributes to ion diffusion through it; thus catalysing the continuous growth of the oxide layer at the metal-oxide interface. Since it composes the anode in an electrolytic cell, it is referred to as anodic aluminium oxide (AAO) as the method is named anodization.

Interestingly, depending on the chemical nature of the electrolyte used in the anodization

process, the AAO layer may result in two different morphologies. In the presence of an electrolyte with moderated pH the oxide layer form as a flat continuous barrier type, in other hand, with more acidic electrolyte a porous layer type forms instead (Figure 3.4).

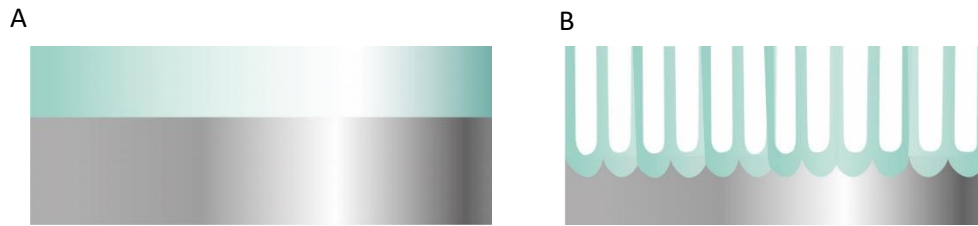


Figure 3.4 Two types of formation layer type, during alumina oxidation. A- Barrier type B- Nanoporous type

The porous layer type is also referred to as porous anodic alumina (PAA) layer and is characterized by cylindrical pores with a determinate diameter (D_p) displayed, organized parallel to each other in a hexagonal structure with regular inter pore distance (D_{int}), illustrated in Figure 3.5. The modulation of these dimensions might be achieved by the balance of different anodization conditions; such as the anodization potential, and electrical field, temperature, and proton (H^+) concentration. These structural features dimensions can be adapt, depending on the electrochemical reaction condition upon its syntheses. Hence, due to its properties, PAA has been intensively explored as a template-synthesis method for nanofabrication, and often named as Nanoporous Alumina Templates (NpATs).

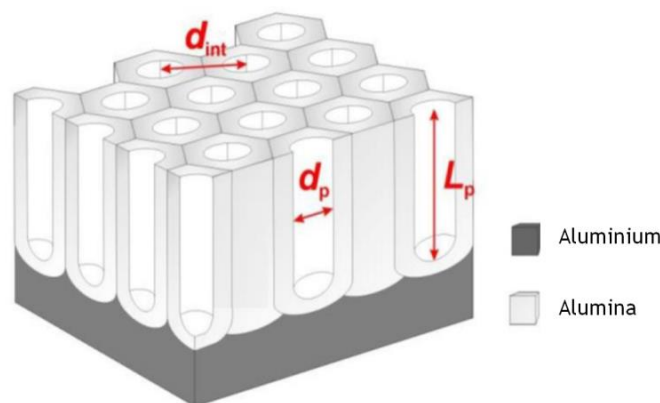


Figure 3.5 - Illustration of the cross section of the PAA. Denotes the different dimensions in the membrane $d(int)$ - interpore distance; $d(p)$ pore diameter and $L(p)$ pore length also referred as the thickness of the membrane [14]

All chemical reactions involved in the formation of PAA are complex and yet to be clarified. Nevertheless, it is hypothesized that the formation of such structures results from a competition between the formation and dissolution of Al_3O_2 , at the aluminium-electrolyte frontier. This duality is easily reflected graphically, where the current density assumes roughly a "J" shape followed by a constant line, which represents the PAA growth in potentiostatic

condition, depicted in Figure 3.6.

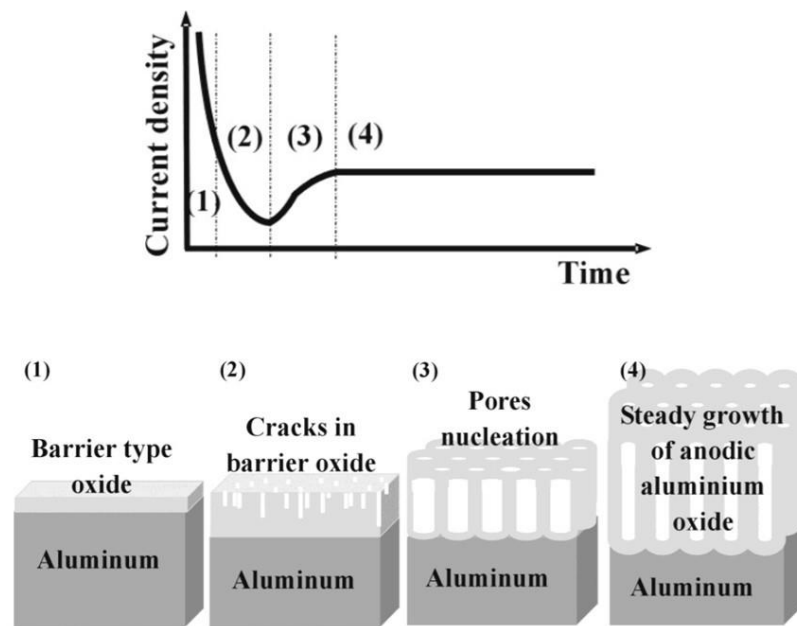


Figure 3.6 - illustrated by the graphic the ideal current density curve on during the mild anodization, which is accompanied with the schematized figures that illustrated evolution of the oxide layer along time of anodization process; the number identifying the each figure refers to one showing in the graphic, demonstrating the event on each phase [13]

Apart from the initial phases, in the 4th and last phase of PAA formation, the current density remains constant along time conversely to the barrier layer type. This is a consequence of the constant thickness of the oxide layer as the pore length increases instead. Thus, the PAA thickness is linearly proportional to the anodization time.

As for the previous stages of anodization's current density curve, it describes the initial formations of the pores, which mechanism is a subject of discussion for decades. However, it is accepted that the initial pores formation is promoted by small protrusions and irregularities formed on the oxide layer that grows under increasing tension, which originates from eventual breakpoint randomly placed. The depression on the modified topography of the aluminium leads to the alteration of the electrical field pattern. Consequently, the concentration of current lines on the thinner places of the oxide layer along with the strong acid contact induces, further on, the formation of pores in the surface of the aluminium.

Therefore, the first stage describes a decrease of the current density due to the initial formation of alumina as an insulating layer; the second stage coincides with the emergence of the irregularities and depression on the oxide layer surface, where the current density decrease diminish and leads to the next stage; the third stage, is specified by the increase of the current density due to the eventual depression on the oxide layer promoting pore nucleation. [14]

Before the application of the anodization method, the fabrication of alumina templates requires, firstly, a pre-treatment of the aluminium (Al) foil, to prevent eventual contamination

and ensure the smoothness of the Al foils surface by removing any eventual roughness. For this purpose, the aluminium foil (99.997% of purity) is cut into pieces with an area of 1.5 cm² and submitted to a sequential ultrasonicated bath with acetone followed by ethanol 96%, during 3 min each. Then, Al foils proceed to an electropolish treatment and each foil is immersed in the perchloric acid solution (HClO₄) under 40 V for 2 min.

After the electropolish process, the Al foils are placed in a particular set up that allows the controlled anodization in a certain area (Figure 3.7). Therefore, the Al foils are settled into anodization cells, between the copper base and Teflon recipient. The recipient has an opening at the bottom, which allows the contact between the Al foils and the electrolyte. An O-ring rubber is placed at the opening to prevent any leakage of the electrolyte. The recipient also holds another structure which ensures that a Platinum wire mesh is immersed into the electrolyte, which constitutes the counter electrode. Both the copper and the Pt mesh are connected by different wires to a source meter (Keithley 2400C), as a working electrode and counter electrode respectively. The electrical voltage applied to the set up by the sourcemeter is controlled by a home-developed LabVIEW program.

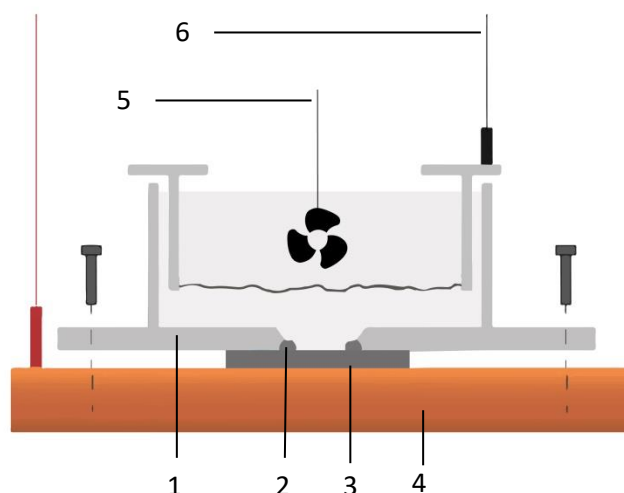


Figure 3.7 - Anodization setup. 1- Base copper 2- O-ring rubber; 3 Aluminium sample 4 copper base connected to de sourcemeter; 5- fan to homogenize the electrolyte temperature 6 - structures that hold the Pt mesh an connects it to the sourcemeter

All anodization process shared some conditions, such as the temperature which was performed at 2 ± 0.5 °C, the electrolyte used Oxalic acid [(COOH)²] at concentration of 0.3 mol/L. However, they differ in the anodization time and the applied voltage. The time is defined depending on the desired length for the nanopores. On the other hand, the voltage contributes to defining the pore's inter-distance and diameter, depending on either one employs mild or hard anodization. The former case uses 40 V and results in NpATs's pores with ~50 nm width and ~100 nm of interpore distance; as for the latter, one uses 140 V and results

in NpATs's pores ~150 nm width and ~200 nm interpore distance.

To obtain highly ordered nanopores into the membrane, the formation of these templates undergoes through a two-step anodization method, which consists of two consecutive anodization processes, is schematically represented in Figure 3.8. At the first anodization, the morphology of the nanoporous alumina layer molds the limit between the oxide-aluminium layers. Thus, after the subsequent chemical etching of the alumina layer with sodium hydroxide 98% (NaOH), it remains a concave pattern imprinted on the aluminium surface. This pattern becomes the nucleation centres for the second anodization and enables the production of organized nanopores in parallel with equal distance between them.

The first step anodization was performed in mild anodization condition during 24 hours. The second anodization was performed either by repetition of the mild anodization, although with the duration time of 48 hours and thus obtain pores with ~100 μm length; or by hard anodization condition for approximately 3 H which results in 150 μm long pores.

After the second anodization, the samples were submitted to another chemical etching to remove the underling aluminium using 0.2 M CuCl_2 in a 4.1 M HCl aqueous solution. At this point, each nanopore of the membrane has a barrier layer at its bottom. To grant the permeability NpATs this bottom layer was removed by chemical etching. Such is achieved by placing the membranes on the surface of the alumina removal solution, at 55 ± 0.5 °C. This is a simple method where the membrane floats in the solution, hence only the base of the membrane has contact with the acid, during approximately 23 min, until the base layer is removed and the nanopores are open. For further opening the pores, the membranes remained sunken into the same solution for additional 10 min, to expand the pore by ~30 nm than the width resulting from the second anodization.

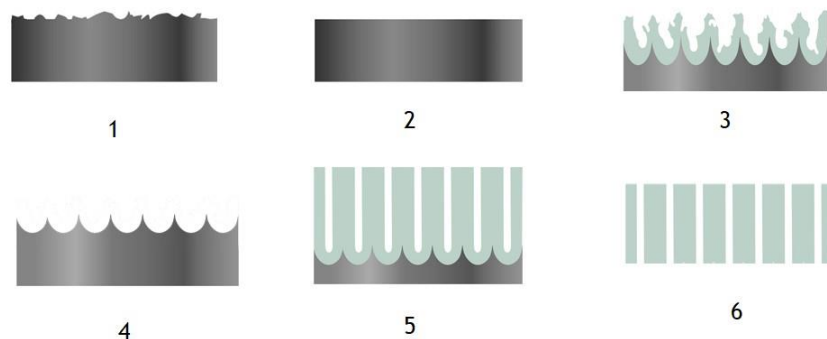


Figure 3.8 Schematic illustration of the formation of NpAT's steps. 1- illustration of the Al foil surface; 2- Al foil after the Electropolish process; 3- the formation of the pores after the first anodization; 4- Al foil after the removal of the alumina layer; 5- formation of the pores after the second anodization; 6 - result after the Al removal and pore opening.

3.2 Electrochemical Deposition

Electrochemical deposition, is based on a redox chemical reaction promoting charge and mass transference from one material to another, while is applied a constant current or voltage. Notice that often these materials are electrical conductors or at least semiconductors, so they can proceed as electrodes. The electrodes used might be the positive terminal of the current and, in this case, are referred to as cathodes; or be the negative terminal and referred to as anode. For electrochemical reaction to occur both electrodes types must be present and immersed into the electrolyte, i.e. the electrically conductive solution.

Depending on the solution used as an electrolyte, as well as the material intent to be electrodeposited, the chemical reactions require to reduce or oxidize the ions dissolved in the electrolyte. Accordingly to the interest of this work, the gold cations ought to be reduced into solid particles, where $\text{Au}^{3+}_{(\text{aq})} + \text{Ze} \rightarrow \text{Au}_{(\text{s})}$. The chemical reaction is composed of several steps, which are schematically represented in Figure 3.9, occurring at the electrode-electrolyte interface, where the electrical double layer is established (see section 2.2.4.).

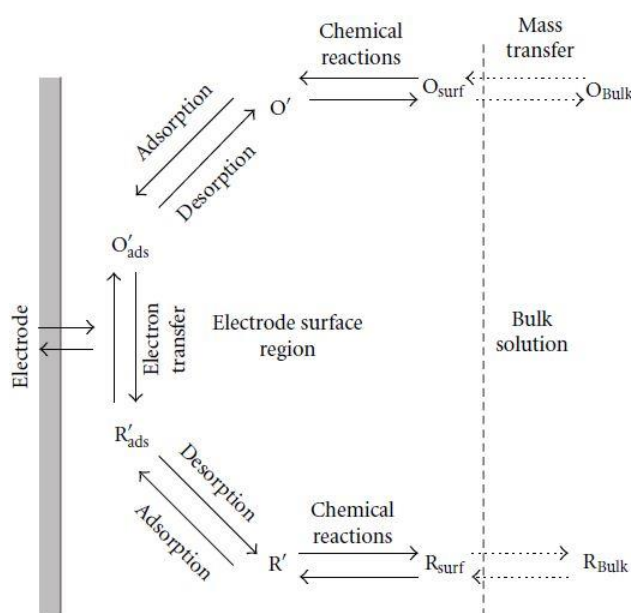


Figure 3.9 - Schematic of chemical reaction for electrodeposition at the electrode-electrolyte interface [71].

Overall, the chemical reaction responsible for the electrodeposition is defined by the mass

transference and electron transference. The mass transference is referent to the movement of the atoms, from de bulk solution in direction of the electrode or vice-versa. This movement might be propelled by migration, convection, or diffusion. The latter type of movement is the one that has more influence on the electrodeposition; it describes the tendency of the element present in the electrolyte to move towards areas with lower concentration. On the other hand, electron transference refers to the ability of the electron to move to other atoms that describe a redox reaction.

These two processes comprise the thermodynamic driving force for the phase transition, and hence the nucleation of the species in the electrolyte. For this, is necessary that the electrochemical potential of the metal ion is larger than the electrochemical potential of the metal. This electrochemical potentials discrepancy allows overcoming the energy barrier for the phase transition, which is called supersaturation [56].

Moreover, several factors contribute to the thermodynamics of the electrochemical supersaturation, which is discriminated at the diagram shown in figure 3.10. Some of the variables are possible to manipulate to achieve a higher rate of electrodeposition; such as the area of the electrode, the temperature, the resistance of the electrodes, and the conductivity at the electrode-electrolyte interface. Those will specifically influence either the mass or electron transfer. Moreover, the slowest of this pair, limits the rate of the general electrodeposition, often is characterized by the process with more resistance.

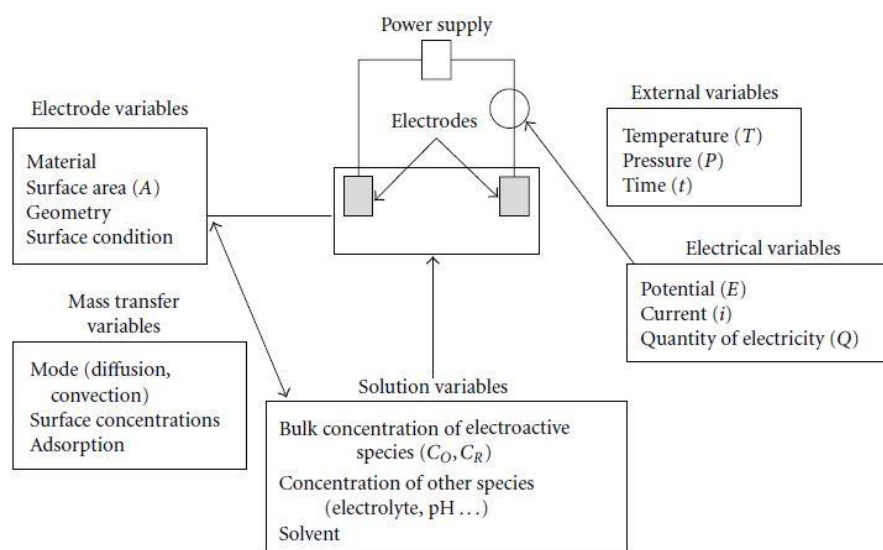


Figure 3.10. Different variables that influences the electrodeposition thermodynamics and kinetics.[71]

In this work, electrodeposition was preceded with a three electrode configuration: the working, the counter, and the reference electrode. Particularly to raise the charge flux, i.e., the current, it is required to meliorate the conductivity by shorting the distance of the electrodes.[71]

The samples are composed of a glass substrate with a thin layer of gold (800 Å thickness), which further on, are cut into ~1.5 x 1.5 cm squares pieces.

By default, the sample is connected vertically to the wire as the working electrode; therefore the sample has attached one segment of copper tape that sustains and connects the substrate to the wire. Both copper tape and the edges of the substrate are covered with varnish to isolate those areas from the electrolyte and limit the extension of the deposition of gold. This set up is collected by a Platinum (Pt) mesh as a counter electrode, Ag/AgCl as a reference electrode, and the sample as a working electrode. They were held close from each to provide the minimum resistance as possible and they were submersed into the electrolyte. The described setup is illustrated at Figure 3.11. Moreover the electrolyte used for gold electrodeposition was composed of a conductive gold cyanide bath ($[\text{Au}(\text{CN})_2]^-$), referred to as Orosene E +4 gr/lt.

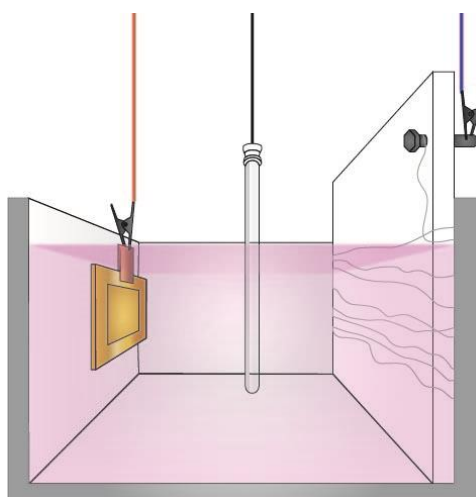


Figure 3.11. - Setup configuration of 3 electrodes for electrodeposition technique. A- Working electrode-cathode; B- reference electrode; B counter electrode- Pt mesh. The purple solution depicts the Orosene electrolyte.

3.3 Characterization of the microelectrodes

3.3.1 Profilometry

The profilometry is a quantitative measurement of the specimen profile, through the profilometer. This method relies on a diamond cantilever to scan the specimen surface, as a contact profilometer, it has a resolution to measure as small as 10 nm of thickness. Therefore, the samples were measured with a Bruker DesktakXTTM, profilometer provided by CEMUP-MNTEC clean-room;

3.3.2 Scattered Electron Microscopy

The morphology of the samples was investigated using scattering electron microscopy (SEM), contributing for surface and cross-section characterization using a FEI Quanta 400 FEG high resolution SEM. Instead using photons (from light beam), the surface of the sample is irradiated by a high energy electrons beam. Interestingly, due to high frequency of the electrons beam wavelength, it allows to produce a higher resolution image of the specimen (as about 5 nm). The beam of electrons (primary beam) is focused and directed back and forth across the specimen by a set of magnetic lenses. For each point of sample that is irradiated, two types of electrons are emitted from the specimen: secondary electrons and back scattered electrons. Secondary electrons emission results of the absorption of the inelastic energy from the primary beam collision, therefore there are characterized with lower energy than 50 eV. In the other hand, backscattered electrons originates from an elastic collision, resulting from the refraction of the primary beam reflection scattered through wide-angle ($<90^\circ$),

3.3.3 Energy Dispersive Spectroscopy

Duo to the different sensor accommodated in SEM, it allows analysing elemental composition of surface of the specimen, by using Energy Dispersive Spectroscopy (EDS) analysis of X-ray radiation. Due the incidence of the primary beam the chemical elements on the surface became ionized, leaving a vacancy of an electron in an inner layer of the atom. Sequentially, an outer electron refill this vacancy it releases its energy, more precisely, X-ray radiation. The X-ray radiations are detected the specialized sensor in the SEM, depending on the energy emitted its possible identify the atoms present on the specimen. Therefore it EDS provide quantitative and/or qualitative information about the element that compose along the surface of the sample.

Chapter 4

Results and Discussion

4.1 The template synthesized

As described in subsection 3.1.1 nanoporous alumina films (AAO) were fabricated through the two steps anodization method. This AAO produces capable templates that will define the dimension of the synthesized nanowires, with high resistance to temperature and chemical degradation as well as low conductivity. Furthermore, they have a homogenous pore distribution, in which the diameter, length interpore distance are tuneable depending on the anodization condition [14]. Initially, the nanowires were designed to have the maximum aspect ratio as possible. Hence the NpATs were fabricated ought to have at least 80 μm height and 50-80 nm width, resorting to mild anodization, which condition are resume in Table 4.1 in the end of this section. The evolution of the process can be followed by the progress of the current density curve, as presented on Figure 4.1. The current density reveals an expected profile, describing the standard “J” shape, where it is possible to discriminate the four-phase on the formation of the nanopores.

Table 4.1 - Resume of the condition implemented for produce NpAT from mild anodization

Mild Anodization		
Parameter	First Step	Second Step
Electrolyte	Acid Oxalate	
Concentration	0.3 M	
Temperature	2 ± 0.5 °C	
Voltage	40 V	
Time	1440 min	2880 min

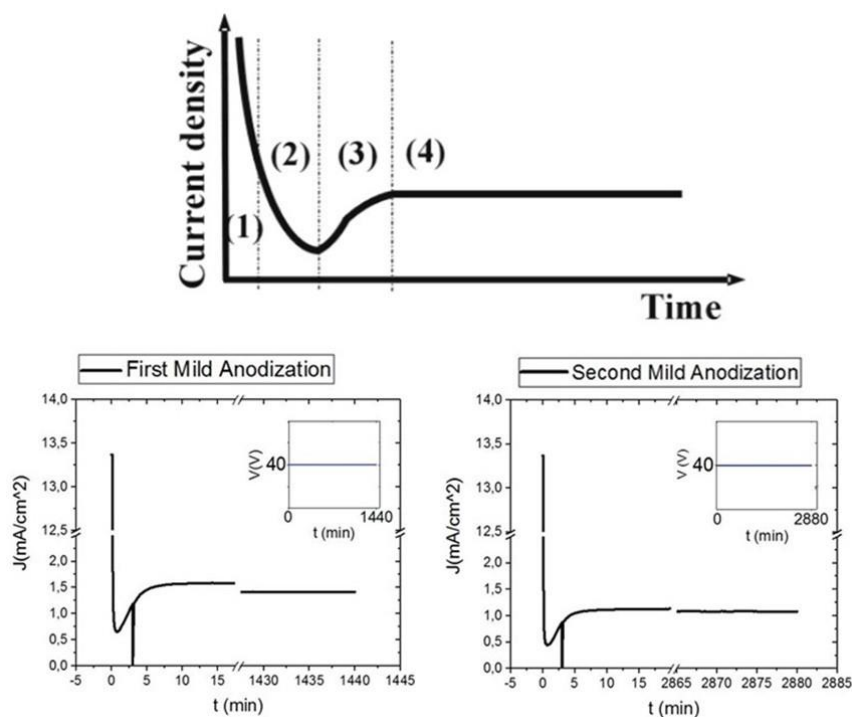


Figure 4.1. - Current density evolution along time, in mild anodization. A. First anodization for 24h; B. Second anodization 48h

The measurements on, SEM images in Figure 4.2, using ImageJ, program assistance confirmed that the produced templates reports desired dimension: 82 nm of pore diameter and 147 μm membrane thickness and 104 nm of interpore distance.

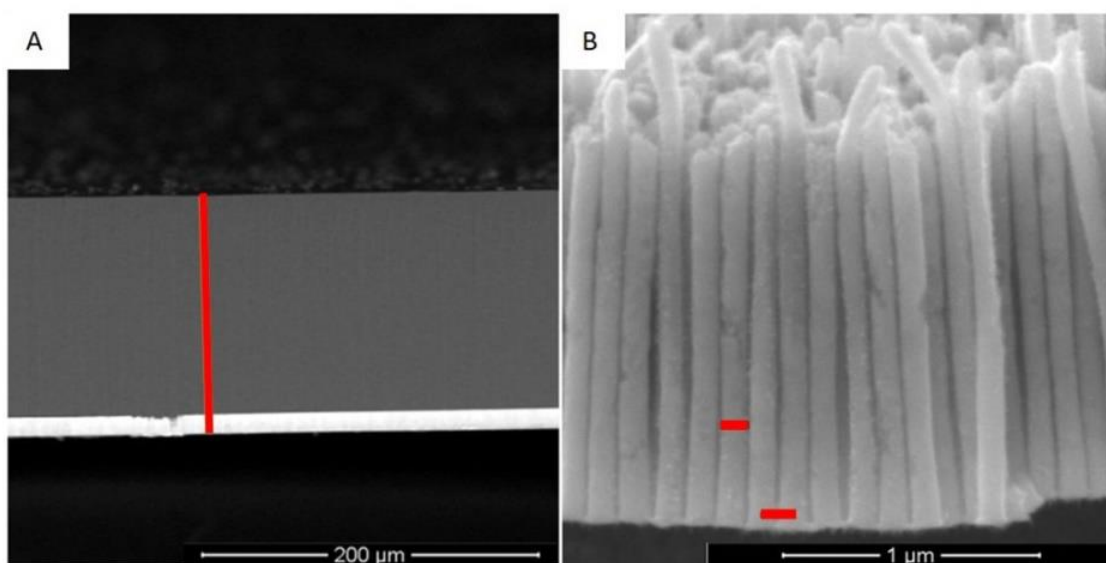


Figure 4.2. SEM picture after the gold electrodeposition in NpAT formed from mild anodization. Through ImageJ, the thickness (A), diameters and distance interpore (B) of the membrane were measured: 147 μm , 82 nm and 104 nm, respectively

At the SEM image from Figure 4.3 it is also possible to observe nanowires that were electrodeposited in a template resulting from mild anodization. However, these microwires demonstrate their tendency to bend over rather than stand straight vertically. This is an issue, considering that posteriorly it will be necessary for the pillar to have a certain amount of mechanical strength during the insertion into the biological sample.

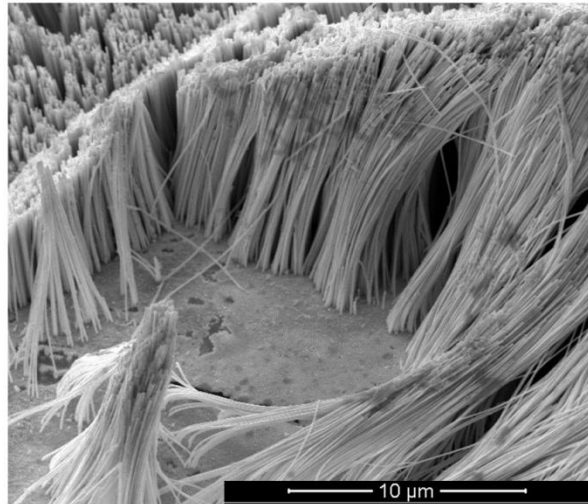


Figure 4.3 - Image capture through SEM technique. Demonstrates ductility of the nanowires resultants of the electrodeposition through NpAT produced from mild anodization

For these reasons, it was resorted to hard anodization for the second step of the anodization process, in order to produce NpAT with larger pore diameter, enabling the synthesis of nanowire with a wider diameter and therefore better mechanical support. The conditions of the hard anodization used are resumed in Table 4.2. In this case 40 V were applied for the first 5 min, to prevent breakdown effects caused by the following high current densities; next was applied an increase rate of 0.6 V/s until achieving a tension of 140 V for 3 h and finalized with 40 V only for 1 min to stabilize the oxide layer at the bottom of the pores.

Table 4.2 - Resume of the condition implemented for produce NpAT from hard anodization

Parameter	Hard Anodization			
	First Step	Second Step		
		Pre-Anodization	Anodization	After-Anodization
Electrolyte	Acid Oxalic	Acid Oxalic	Acid Oxalic	Acid Oxalic
Concentration	0.3 M	0.3 M	0.3 M	0.3 M
Temperature	2 ± 0.5 °C	2 ± 0.5 °C	2 ± 0.5 °C	2 ± 0.5 °C
Voltage	40 V	40 V (With rise of 0.6 V/s)	140 V	40 V
Time	1440 min	5 min	180 min	1 min

Depicted graphically at Figure 4.4, it was possible to follow the hard anodization progress,

similar to mild anodization, through the current density current evolution. Accordingly, as described at section 3.2, as the tension increases at the rate of 0.6 V/s the current density also increase, indicating that the oxide layer formed at the bottom of the pores is still not thick enough against the tension applied; nevertheless, the subsequent decrease of the current density indicates the PAA is continuously being formed.

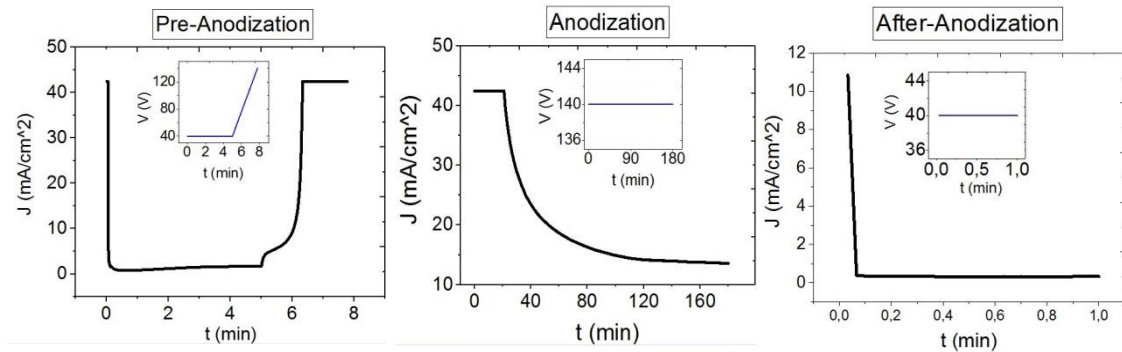


Figure 4.4. - Hard anodization graphics. The resulting development of current density of the three phases: Pre-Anodization, Anodization and After-anodization

Again it was resorted to SEM technique in order to verify the success of the templates syntheses. In Figure 4.5., with ImageJ was possible to investigate the dimension the NpAT that resulted from hard anodization, where it is observe a pore diameter of ~ 259 nm, interpore distance of ~ 314 nm and the thickness of ~ 189 nm.

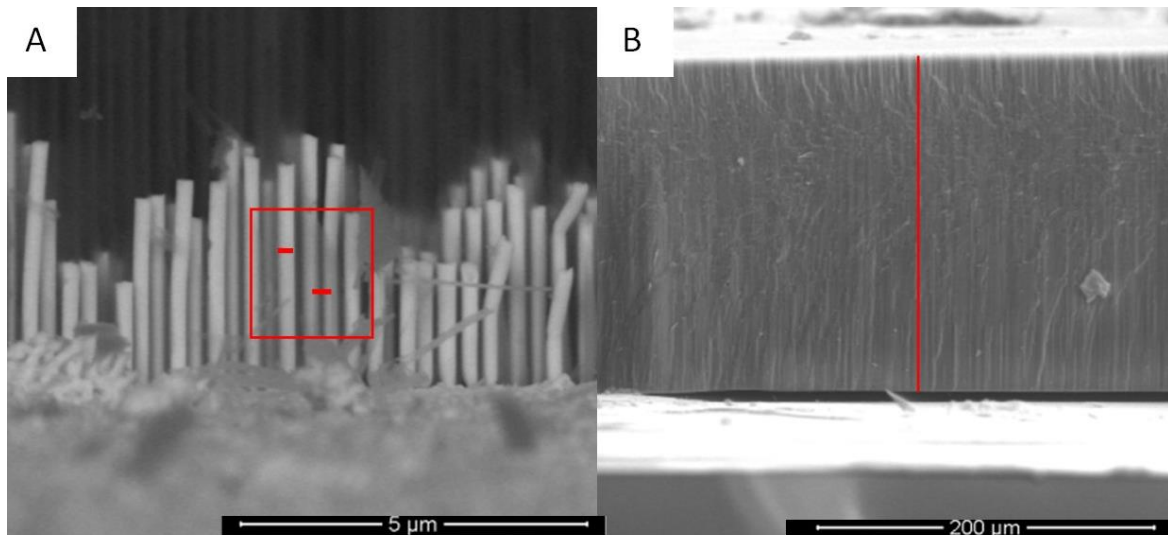


Figure 4.5 - SEM picture after the gold electrodeposition in NpAT formed from hard anodization. Through ImageJ, the thickness (A), diameters and distance interpore (B) of the membrane were measured: 189 μm , 259 nm and 314 nm, respectively

4.2 Optimization of the electrodeposition

For the purpose of optimization of the electrodeposition, it was first performed a Cycle Voltammetry (CV) to select the most adequate potential for gold electrodeposition; a temperature test to define the highest electrodeposition rate, as well as, understand the stability of the electrodeposition current density curve along time, as it is applied a continuous and constant voltage.

4.2.1 Cyclic Voltammetry

The cycle voltammetry study allows measuring the current behaviour under different potential values, by increasing and decreasing the potential cyclically. This provides information about dynamics of the oxidation/reduction of the solution during electrodeposition, such as the reversibility of the reaction, as well as, the potential range where the oxidation and the reduction of the electrolyte take place. Each cycle performed, from maximum to minimum potential (or vice-versa), is referred as a scan. Therefore the velocity of the potential linear variation is termed scan rate (mV/s).

In this work it was use the DC electrodeposition of the orosene solution in potentiostatic configuration. The reduction of the Au in the Orosene occurs in a negative potential, therefore the cyclic voltammetry was performed between the potential values of -1.6 V and 0.0 V with the scan rates of 100 mV/s, in a gold sputtered NpAT sample. The resultant graphic at Figure 4.6 at the pace that voltage value decrease the current density curve between -1.6 V and -0.8 V tends to decrease faster, therefore in this interval is associated to a faradaic and thus manifesting the occurrence of deposition. Moreover particularly, at the value -1.0 V the slope increase, this indicates that there is a higher rate of electrodeposition, at this point. The increase intensity of the current leads to the increasing number of charged transferred, and in turn, it leads the increase of thus the rate of electrodeposition. However, one should considerate that: too low voltage values are also associated with hydrogen evolution reaction in aqueous solution, which lead to bubble formation on the thin film deposited, jeopardizing the consistence of the pore filling. Therefore although the graphic at Figure 4.6 demonstrates other values with a high current density slope the gold reduction peak was determined to be at -1.0 V.

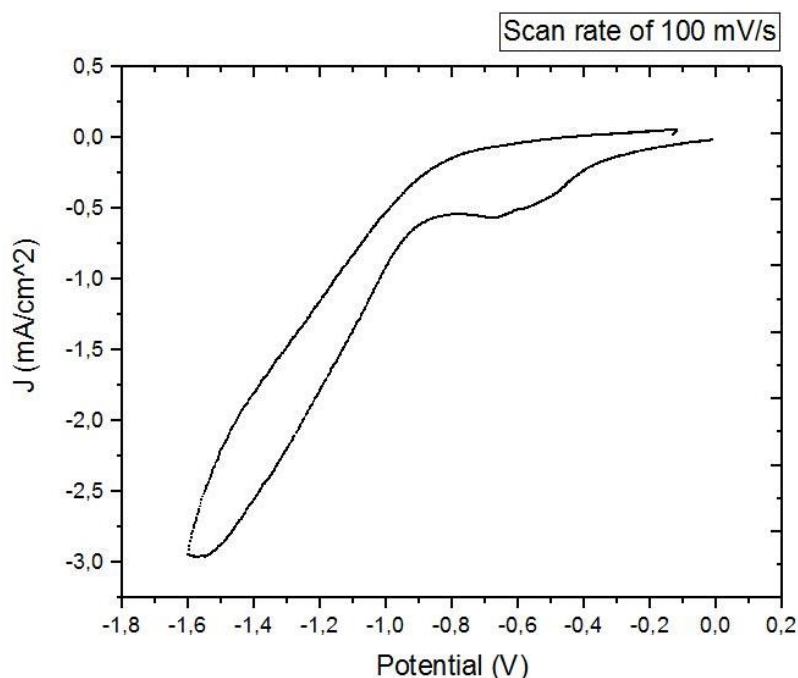


Figure 4.6 - Cyclic Voltammetry of orosene, between -1,6 and 0 V with a scan rate of 100 mV/s

4.2.2 Temperature

As referred in section 3.2 the temperature is one of the variables that influence the rate of the electrodeposition. Therefore in order to improve the time necessary to achieve the height proposed for nanowires, they were electrodeposited for 10 min each, at -1 V in different temperatures (17, 20, 30, 40 °C). The electrodeposited thickness was measured through a profilometer, the values average of three measurements are discriminate in Table 4.3.

Table 4.3. - Thickness of samples electrodeposited with different temperature (17 °C room temperature, 20 °C 30 °C)

17 °C	20 °C	30 °C
214.8 nm	125.1 nm	709.4 nm

Results demonstrate empirically there is an increase in the electrodeposition rate when the wile temperature is approximately 30 °C. Accordingly stated by Gamburg et al., suggest that the higher temperature might be favourable to increase the rate of electrodeposition augmenting the solution solubility and thus the mass transfer [72]. The result at 40 °C demonstrated too thin for the profilometer resolution. Thus, it was only possible to perceive one measure of 84.92 nm which is less than half, when compared with the other temperature.

Although it alludes coherently with literature, that too high temperature might be

prejudicial for the efficacy of the electrodeposition [72, 71], the measurement of sample thickness corresponds to the electrodeposition at 40 °C cannot be considered, since that temperature might be damaging for process of electrodeposition.

4.2.3 Continuous electrodeposition duration

Knowingly, the increasing number of nuclei is dependent of time, thus also the length of the electrodeposited nanowires [73]. Often is described in previous works electrodeposition employed with duration ranging minutes. However, in the extent of my knowledge, there are scarcely any reports of electrodeposition for long duration time. Deducing that long term deposition might cause an increase on the temperature and therefore cause perturbation on the current density curve; it was investigate the effect of the continuous electrodeposition for several minutes (up to 1 h 42 m), with a DC current, through the development of the behaviour of the density. With this purpose were performed two experiences. The first has the objective to observe the density curve development, as it is applied -1.0 V as long as possible. This is, until the current density curve demonstrates sings of instability. The second experience has the objective to observe the stability of the current density curve, while it is accumulate an intermittent and successive 10 min electrodeposition, by applying -1.0 V. Note that graphics presented at Figure 4.7 and 4.8 are the result that most represents the overall of the different experiments repetition.

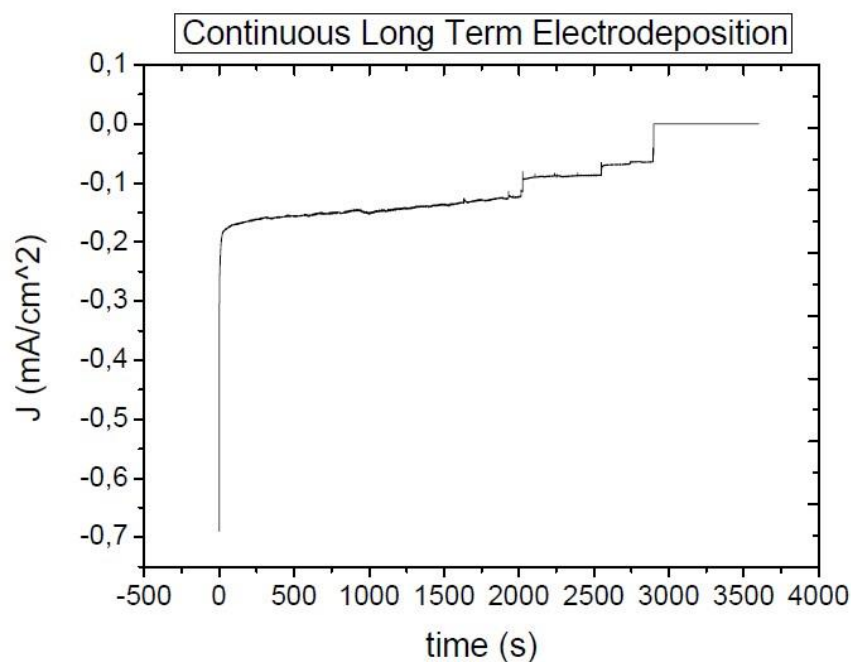


Figure 4.7 - Graphic of current density curve the experiment where it is been electrodeposited continuously during 3600 s corresponding to 1 h.

As it is shown at Figure 4.7 the current density curve follows the standard behaviour as it increases in the initial seconds and then it stabilizes where there is low variation of the Current density. As the time passes by the 2000 s, the current density curve starts to manifest some instability, as the curve further approximates abruptly to the 0.0 mA/cm^2 ; at the time of 3000 s the current is null.

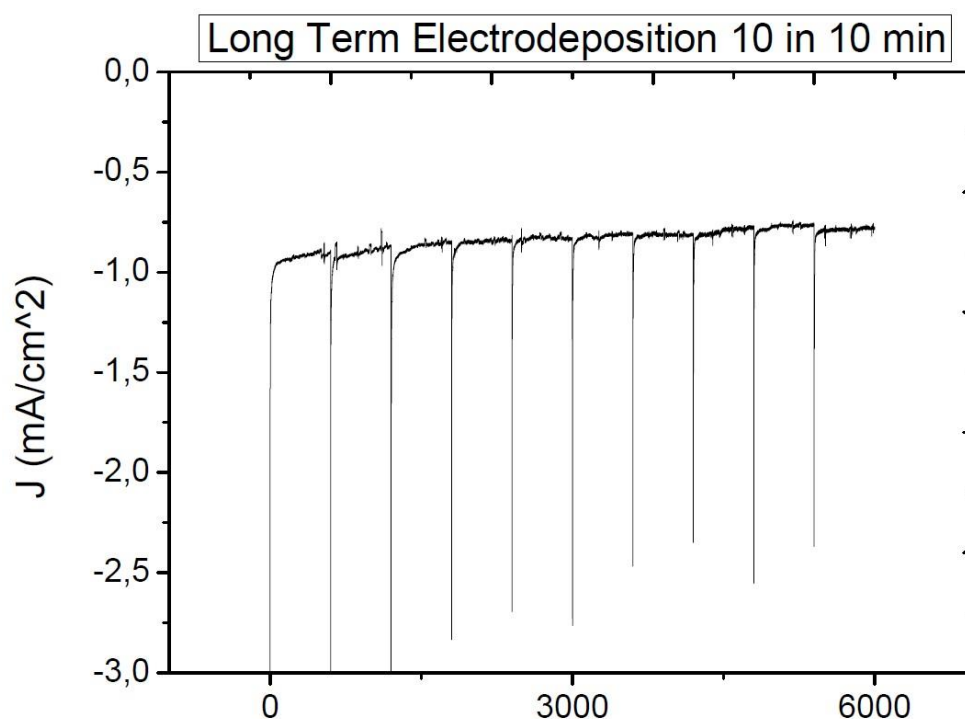


Figure 4.8 - Graphic of the current density curve development as it accumulatively implemented 10 min of electrodeposition, pausing 2 min between each other. The total duration is 6000 s corresponding to 1 h 42 min.

The results from the graphic depicted at Figure 4.8 demonstrates there is no significant variation of the current density along time, in contrast to the previous experiment where a continuous voltage has been applied; even considering that the present experiment have been performed for longer time.

Considering the results obtained as hypothesized that, by pausing for 2 min the electrodeposition contributes to maintaining the stability of the electrodeposition. Therefore it facing the results presented was delineated employing cyclically - 1.0 V during 2400 s (40 min) followed by 2 min of pause, for future electrodeposition in this work; in order to compromise maintaining the stability and minimize the time necessary to achieve 80 μm nanowires long.

4.3 Sputtered membrane

Attending that the NpAT are characterized as an insulating material, is necessary to add a conductive film at the base of the membrane to provides a good electrical conductor point, convert the template to a working electrode, for posterior electrodeposition.

Considering that nanowires would be posteriorly synthesized directly from the MEA substrate, is not possible to add this conductive film; since it would cease the individuality of the recording sites. Nevertheless, it was performed electrodeposition in a previously sputtered membrane with Au thin layer to NpATs, resulting from mild anodization (kindly provided by João Fradet, fellow investigator at bottom-up Laboratory, at FIFIMUP), and performed Au electrodeposition. Thus allowed the investigating, for further comparison, the progression of the current density in a context where the conductivity layer base is completely adhering to the template base

Therefore a thin Au film was coated on the backside of the AAO membrane side by sputtering deposition, in order to produce a base and cover the pores. From the figure, 4.9 obtained at SEM is possible to observe that the electrodeposited nanowires showed in white in a considerable degree of homogeneous growth.

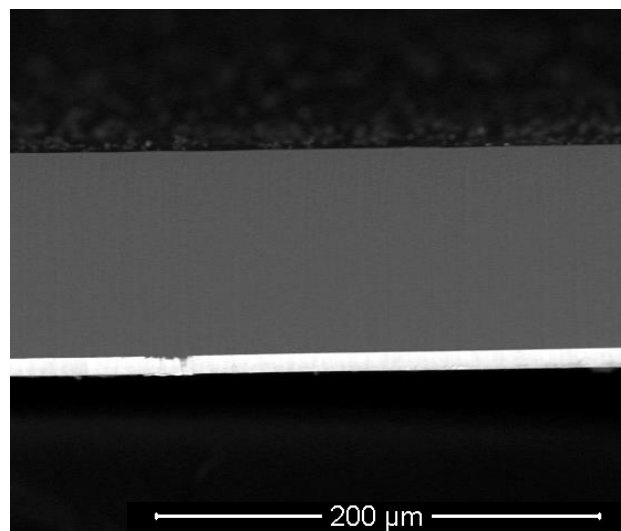


Figure 4.9 - Image captured from SEM of the sputtered membrane. In white are depicted the gold nanowires electrodeposited, with relatively same height, into the membrane depicted as the grey band.

After 10 min of electrodeposition, in the figure 4.10.A delaine a graphic of the current density was obtained, it is possible to verify decreasing current density at the first 50 seconds establishing at the value of ~ 0.3 mV/cm². For futures reference, is worth notice that visually electrodeposited nanowires are perceived, in top views of the template, as black coloration areas, Figure 4.10.B.

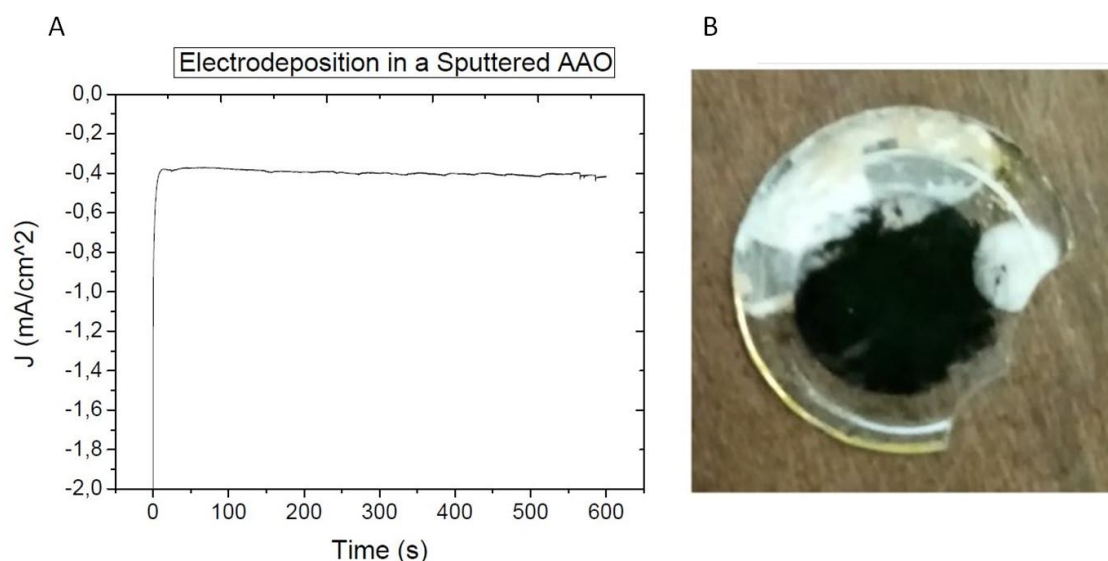


Figure 4.10 - Results of the electrodeposition depicted graphically current density along time (A) and the top view of the electrodeposited NpAT (B)

4.4 Transferring the NpAT to the Substrate

The NpAT one-sided coated with the Au layer is widely used for the synthesis of nanowires among other nanostructures [74]. However, it does not allow the integration of these nanomaterials directly into the substrate of functional devices for signal acquisition. Since to directly electrodeposit the nanowires onto the MEA device, it is necessary first to be able to adhere and stabilize the NpAT to the substrate surface, and then electrodeposit the Au nanowires. Thus, it is as a fundamental point in this work is to be able to assure the adherence of the NpAT to the substrate, where it was investigated different forms of sample preparations to achieve uniform nanowires growth.

It is worth to notice, that the electrodeposition that follows the several template preparations, was delineated to be performed according to the results comprising the experiences for electrodeposition optimization. This means that, each electrodeposition cycle encompasses 40 min of -1 V electrodeposition followed by a pause of 2 min at approximately 30° C. Further on, it was assessed the ability to grow uniformly in the electrodeposited area as well as posteriorly characterized by SEM. Although it was not possible to successfully fill up the nanopores, it is discriminated in this section, the different approaches used to attain the most uniform growth as possible. The electrodeposition graphics of the current density, demonstrated to be fairly similar to the one presented in the figure 4.8, apart from sudden drops on the density current or abrupt changes to 0 V, of which corresponded either to eventual

leakage or loss of contact, respectively. Furthermore for clarity purpose, the several samples were named depending on the type of the preparation which was employed. For improving clarity purposes, follows the Tables 4.4 and 4.5 discriminate the representative samples of used in this work along with the description of their preparation and subsequent observation.

Table 4.4 - Picture that identify each representative sample, after the electrodeposition.


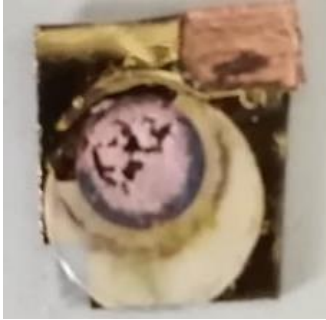




Sample A	Sample B	Sample C
		
Sample D	Sample E	Sample F
		

Table 4.5 - Resume of: the preparation condition for electrodeposition, results of observation and percentage of the electrodeposited area of the respective sample. Note that sample are not depicted in the previous table 4.4 due to the lack of change between before and after the electrodeposition

Sample name	Preparation conditions	Observation after the Electrodeposition	Percentage of electrodeposited area
Sample A	Sputtered membrane.	Total coverage of the black area.	100 %
Sample S	Use the standard setup describe at section 3.2.1. Spin coated with S1818 and soft baked.	S1818 lost consistency. The NpAT fell. No formation of nanowires.	—
Sample V	Use the standard setup	Varnish lost consistency.	—

describe at section 3.2.1. The NpAT fell.
 Fix with Varnish. No formation of nanowires.

(Continuation of the Table 4.5)

Sample B	Fix with varnish.	Broken NpAT.	35.5 %
Sample C	Fix with varnish.	Broken substrate (was remove shortly after initiating the Eletrodeposition.	—
Sample D	Fix with varnish. Released pressure.	Leakage of the electrolyte.	24 %
Sample E	Vacuum (<30 mbar, 40 min).	Increasing of the area covered by the black stain.	70 %
Sample F	Vacuum (<30 mbar , 40 min) Applied in the center a similar weight that exercised by the O-rig rubber.	No black stain verified, still a different tonality colour is verified. However due to different condition of reference electrode during electrodeposition the result cannot be considered.	—

In a first approach, the NpAT was fixed on the substrate using S1818 photoresist or varnish, since both of the products can be removed easily with acetone. These samples are referred to as sample S and V, respectively.

In the case of the sample S, a 1.5 μm photoresist layer was applied on the substrate uniformly through the spin coating at 3000 rpm with for 60 s, and then the NpAT was perched on top of it and baked for another 120 s at 115 °C. Once the photoresist solidified, a drop of acetone was applied on the top centre of the template; in such a way that the liquid infiltrated into the membrane, reaching and dissolving the S1818 directly underneath. With the aid of a paper the acetone used was removed and as result, the membrane was fixed by S1818 at the edges of the membrane leaving the central zone with the gold layer of the substrate exposed, see Figure 4.11.A.

In the case of the sample V, the NpAT was laid on top of the substrate and it was simply applied varnish at the edges of the template in order to fix to the substrate and isolate the areas of the gold layer of the substrate that are not covered by the NpAT. The different preparations are schematically depicted at Figures 4.11 B and C.

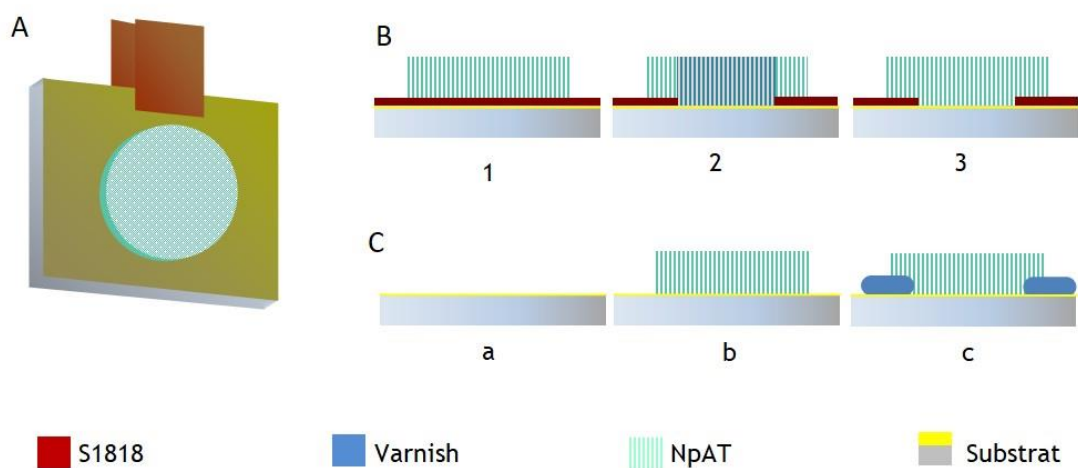


Figure 4.11 - A-The final result of the preparation of vertical samples, where It disposes of a copper tape attached to the gold substrate, which in turn is isolated at the edges, either with S1818 (for the sample S) or varnish (for sample V). B and C describe the process for sample preparations. B -sample S preparation process: 1- spin coated application of the NpAT and baking of S1818. 2- Application of the acetone 3- removed acetone; C- sample V preparation process: a-the gold substrate b- application on the NpAT c- application of varnish surrounding the NpAT.

Both cases were submitted to electrodeposition, in which the sample was set up as the working electrode vertically and in parallel to the Pt mesh as the counter electrode. After a couple of electrodeposition cycles, both samples with the S1818 and the varnish loosed consistency. As a consequence, the S1818 sample resulted in the complete detachment of the template; as for the varnish, the template resulted in the thinning of the varnish layer, which led to electrodeposition on unwanted areas, on the varnish sample.

Upon this result, another approach was employed, whereas neither the S1818 nor the varnish would be in contact with the orosene during the electrodeposition. In this case, the samples were prepared similarly to the sample V (figure 4.12.A). However this time they were packed in an identical set up used for anodization, described previously in section 3.1.1, but in place of the Al foil, the samples are packed between the copper base and the Teflon recipient instead (see figure 4.12.B).

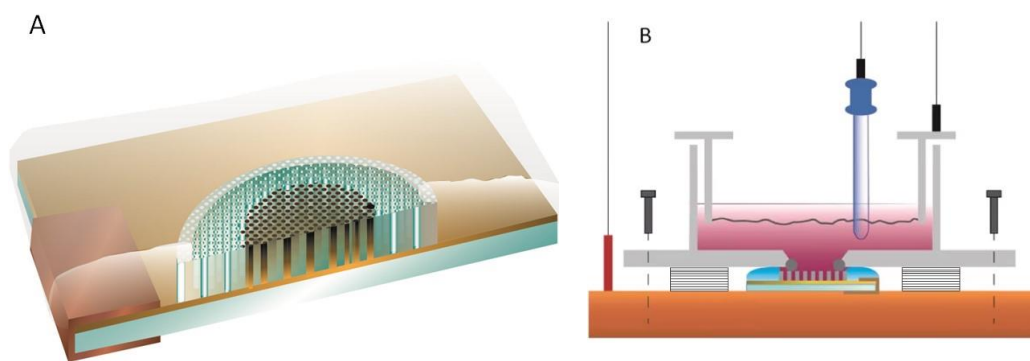


Figure 4.12 - A - Illustration of the cross view of the resulting samples preparation to be integrated on the set up illustrated in the left. It characterizes by the substrate piece (light blue) with a thin film of gold (in golden), wrapped in copper tape show at the right side of template. At the top centre of the substrate is illustrate NpAT with the respective pores, some on the centre are coloured at back demonstrating the ideal result. Surround it, the varnish showing in semi-transparent colour. B- Illustrates the setup similar to the anodization described at section 3.2.1. Although in this case the electrolyte used is orosene depicted with a purple colouration instead.

This assembly is useful when adding NpATs to the samples, since it facilitates the immobilization of the membrane on the substrate, depending only on the weight of the Teflon recipient. Note that, for this setup, the samples also had attached two copper tapes; however, they are folded in such a way that provides an electrical connection between the copper base underneath and the gold layer on the surface of the substrate. This is important because it provides an electrical connection between the copper base and the thin gold layer at the top of the substrate. The margins of the sample are also coated with varnish to provide additional support and better weight distribution from the Teflon recipient, electrolyte, and the structure with Pt mesh. Additionally folded papers were also added, neat to the sample, between the base copper and Teflon recipient, for the same reason of mechanical weight support. The result of samples preparation used and set up used is depicted in Figure 4.12.

As an improvement, this setup (show in Figure 4.12.B) allowed the NpAT to stay in place during the electrodeposition process. However, it was verified from several samples prepared, such samples B and C shown in Figure 4.13.A and B, that after electrodeposition they have a tendency to be broken at the NpAT or at the substrate. For that reason, it was hypothesized that the overpressure applied on the screws cause the template to be too constrained. Although, by releasing pressure on the screws, resulted in leakage of the orosene and consequently the electrodeposition out of the designated area Figure 4.13.C. Hence, to bypass this problem, a piece of cotton was added underneath the sample. The cotton provided a micro shock absorber during the electrodeposition, while also providing enough pressure on the sample against the Teflon recipient so that it prevented any leakage of the orosene

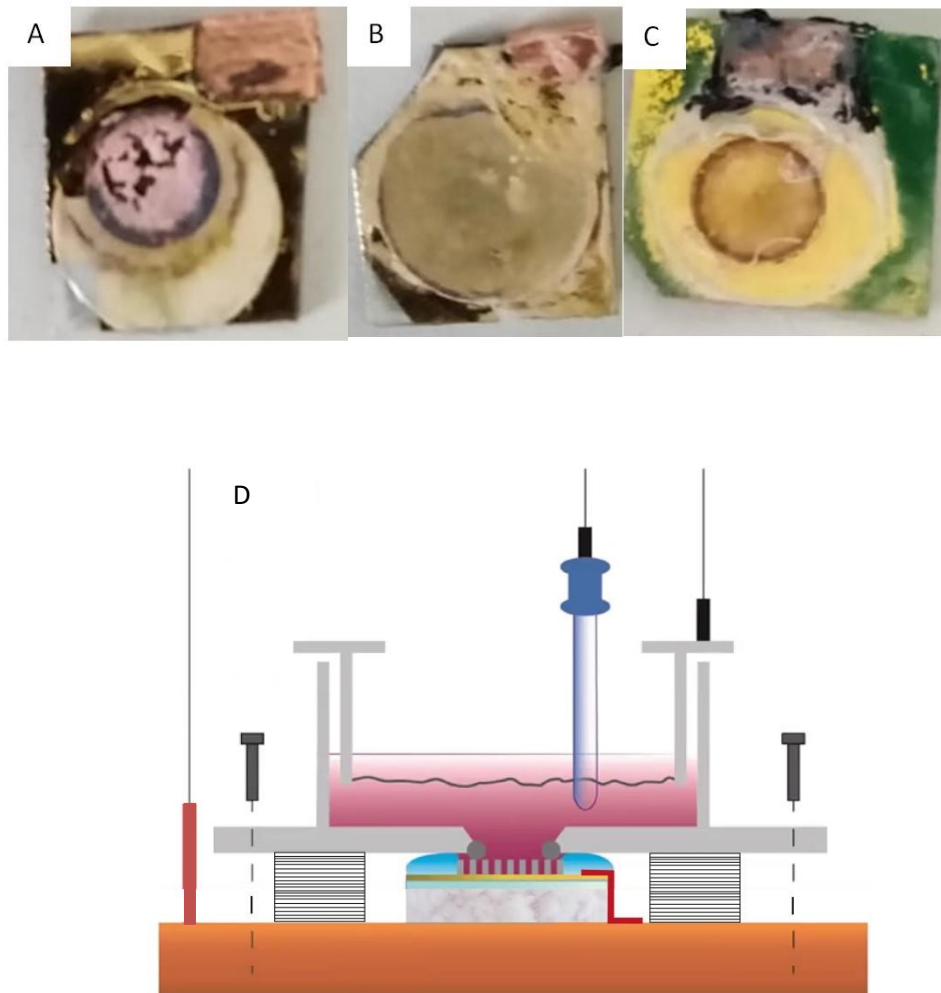


Figure 4.13 - Pictures of the sample after the electrodeposition. A- Sample B demonstrates the broken template; B- Sample C was not electrodeposited, since the substrate broke soon enough to grow nanowires. D - Identical set up presented in Figure 4.12, but modified by introducing a piece of cotton below the sample.

Similarly to the NpAT coated Au film, it is expected that after some given time of the electrodeposition to be visually perceptible a uniform black circle, such as depicted in Figure 4.10 (sample A), in a top view perspective of the sample. Instead, even after the double of electrodeposition time used for the sputtered membrane; from a top view, it is only visible the traces of a circumference were achieved. Thus, it was deduced the area that manifests the black trace, is where only the zone that the NpAT is actually adhered to the substrate. Furthermore, it was hypothesized that the improved electrodeposition in this area was caused by the pressure from the O-ring, which is the support point of the Teflon recipient's weight.

Consequently, to achieve more uniformity just before the electrodeposition, the next

sample already packed in the setup, the Teflon recipient was filled with Di-water and submitted to ~40 min of vacuum (<30 bar). This sample, named and depicted at the Tables 4.4 and 4.5, as sample E, after electrodeposition demonstrated improvement in terms of area cover by the black stains, possibly indicating the formation of more nanowires.

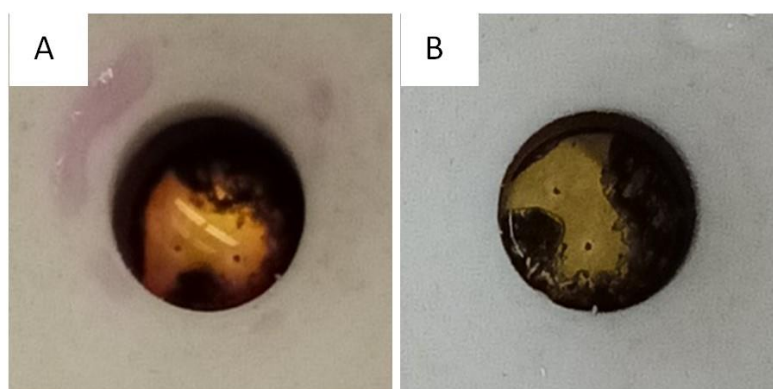


Figure 4.14 - Sample E. A- at 8 h after electrodeposition B-12 h after electrodeposition

Note that, the Figure 4.11 A and B shows two pictures of the sample E, respectively when with a difference of 4 h of electrodeposition. In terms of area covered by black stain, they have practically the same. Seemingly, the result of electrodeposition within 4 h apart, there is almost no evolution in term of distribution of the nanowires formed; which might be explained by the fact that there is more tendency of deposition in higher points in the electrodeposition surface, like on the area where some nanowire are already formed. This is substantiated by some investigators that in the higher point on the z-axis of the topography of the substrate the thickness of the diffusion layer is smaller on the substrate-oresene interface [75, 76]. As a consequence, those elevated points have a diffusion layer that is more compact, leading to higher mass transport and thus a high current density.

For morphology characterization, it was obtained a cross-section analysis of sample E depicted at Figure 4.15. In those images it is possible to clearly denote the gap between the substrate and the NpAT template mostly at the middle of the membrane. Although this sample was the most successful in terms of uniformity on the area electrodeposited compared with the others samples, it was still possible to observe with resorting to the ImageJ a gap with approximately 6 μm .

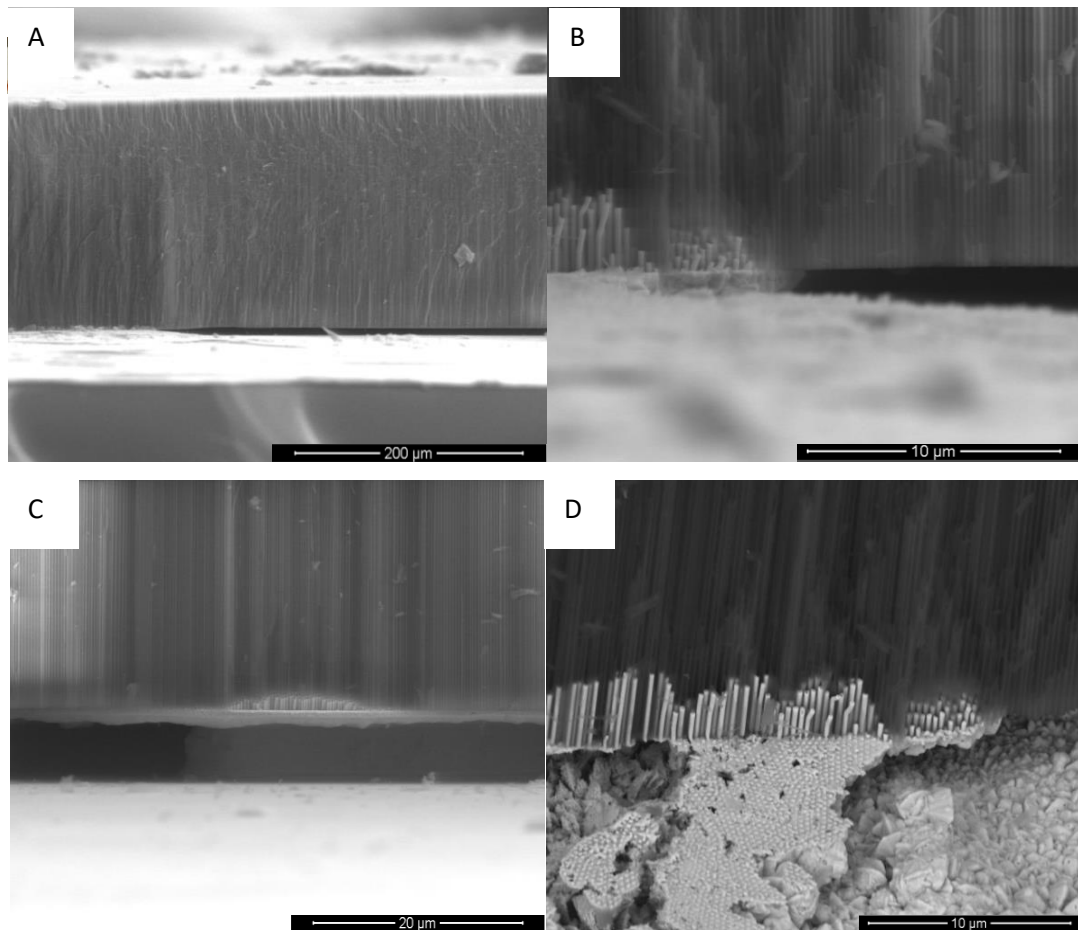


Figure 4.15 - SEM images demonstrating cross section of the sample E with only a half of the template removed. The scale of the images, it reads: A- 200 μm B –10 μm C- 20 μm and D-10 μm.

Further on to reduce the gap between the template and the substrate it was fabricated a weight which adapts to the setup currently used for the electrodeposition, in order to provide an extra pressure at the center of the sample F, depicted in Figure 4.16. Yet, the resulting sample F after the electrodeposition, did not present significant trace elements of nanowires, apart from the circle with a colour with a different tonality under the membrane, shown in figure 4.16. These could suggest the beginning of a uniform electrodeposition. However, at the end of this experiment the electrode of reference manifested some contamination, which calls into question the voltage used and hence it precludes any coherent conclusion. Therefore would be interesting, as a continuation of this work, to repeat this experiment.

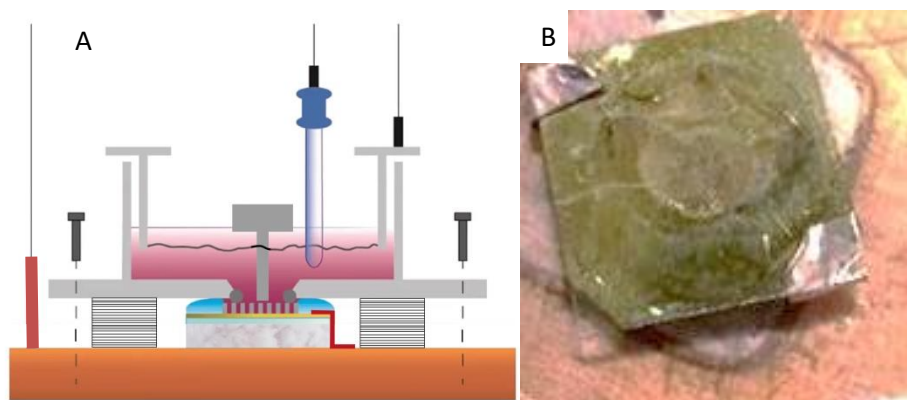


Figure 4.16 - A- Identical set up presented in Figure 4.13.D, but modified with an extra weight employer at the centre of the sample. B-Result of the sample F after the electrodeposition, where extra weight was employed

Furthermore, EDS analysis of the sample E, displayed at Figure 4.17 shows the components present in the samples. As expected, the main component that is revealed is the Au atom, however there are also traces of oxygen (O), aluminum (Al), potassium (K) and carbon (C). Additionally there is a trace of titanium (Ti) however barely has a peak associated. The presence of O and Al elements are explained, since the sample analyzed still had the half of the alumina membrane. The presence of K denotes traces derived from acid used to etch chemically the NpAT, which still remains on half of the membrane present on this sample. In case of the C probably derives from a fiber of the cotton used during electrodeposition. Note that, the allocation of this cotton fiber might occurred due to reduced dimension of the substrate ($1,5\text{cm}^2$) used in the experiment; which would not be a problem once applied the process directly on the MEA once applied to the MEA.

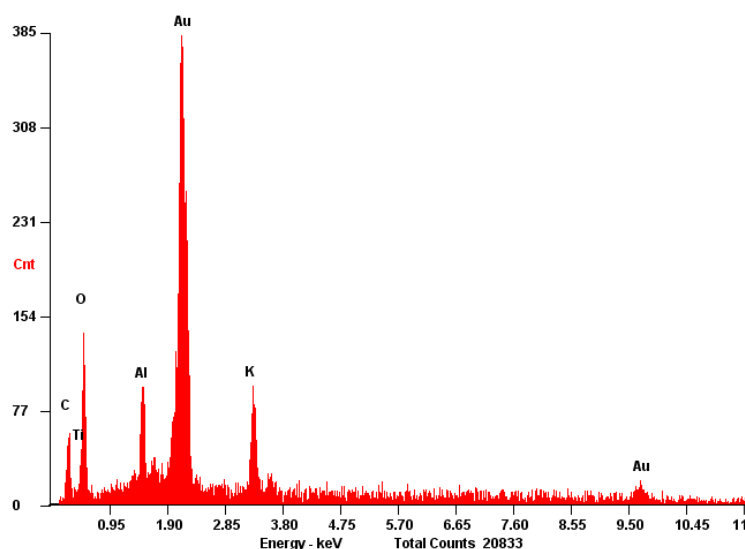


Figure 4.17 - EDS spectrum of the sample E with the NpAT

Although the element on the EDS analysis are justified, further investigation should be performed in order to verify if the impurities between the template and the substrate are the cause for the difficulty on the adherence at the middle of the sample. Therefore the results of chemical characterization, alludes to the fragility of the sample preparation against the emergence of eventual impurities between the template and the substrate which prevents their total contact. Hence it might be needed further pre-treatment of both the substrate and the template in order to guarantee that no any particle is between them.

Another hypothesis for the incompletely adherence to the substrate, is that the membrane is not completely plain, and therefore when it is packed on the anodization setup it might suffer some distortion; as a result of the pressure exercised by the Teflon recipient through the O-ring, the middle of the membrane gets away from the substrate.

Despite what is hypothesized above, the reason for the membrane not adheres to the substrate in its center is unclear. Nevertheless the Au tends to electrodeposit more at the edges of the designated area. Hence as a future experiment, would be interesting experiment the electrodeposition in an sample that was previously prepared on top of a substrate with a isolator layer patterned with 6 orifices: one at the center and others 5 around it; so that the orifices are distributed across the area with O-ring rubber, illustrated a Figure 4.18.A. With this condition the O-ring will be pressed against the isolator layer and not on the orifices area that are exposed to orosene. This experience ought to observe which of the orifices would be electrodeposited, if the pressure was the cause for faster formation on the edges in the previous experiments, then is expected after the electro chemical depositions of this sample the orifices and the subsequent nanoporous would be uniformly filled. The Figure 4.18.B demonstrates preparation of substrate for experience proposed. However, due to time constriction it was not possible to perform the electrodeposition.

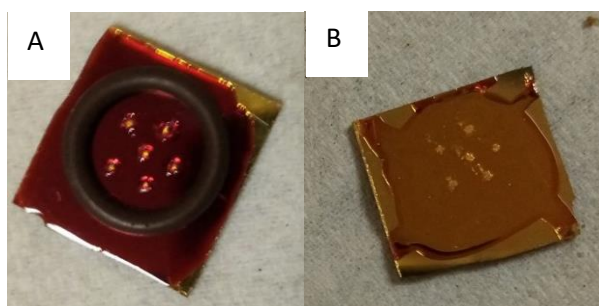


Figure 4.18 - Result of the preparation of the sample for proposed experience. A - Although the thickness of the layer is too high, therefore not the right sample; it demonstrates the distribution of orifices with the O-ring for scale. B- The sample prepared with the right thickness.

Additionally, others approaches reported in previous works, stated their ability to improve the template transferring to the substrate, such by coating the substrate with conductive polymers, resorting to van der Waal forces or by thermal annealing the two parts together [74, 77, 78]. Attending to that, once the process is applied to the MEA (acting as the substrate) the individuality of the recording sites should be maintained, therefore was not considerate as an option; on the other hand the annealing method described in Lombardi et al. [78], applying 500 °C to the sample during 2 h in the presence of Nitrogen was implemented. However it was not possible to reproduce the results reported, most likely due to the difference of the template thickness used on their work (range few hundred nm), since the membrane currently used as template are much thicker and possibly as result the coalition of the two material are less stable.

4.5 Future perspectives

Unfortunately is was not possible to produce further experiment, nevertheless, once reunited the conditions necessary for adequate template adherence and subsequent Electrodeposition of at least 80 μm high of nanowires, others experiences should follow, in order to verify the efficiency and biocompatibility of electrode produced this method such as:

- 1) Repeat the chemical characterization, with only the substrate and the structures formed resultant from electrodeposition. So that is possible to verify the elements present in the electrode. This is important since at final microelectrode using this fabrication process, ought to be in contact with the biological samples; thus it will have great influence on their biocompatibility.

- 2) Perform electrical characterization through the four-terminal sensing test, which is able to measure the electrical impedance and resistivity of the material that constitute the electrode. It resorts to two pair of type of electrode that senses either the current or the voltage. The separation of these two types, allows this technique to discard the contact and the lead resistance from the final measurement. Therefore it enables to perceive small values of impedance of the material, which is convenient since is expected that the gold use to build these structures having a low impedance, composing a critical characteristic for the electrode efficiency.

- 3) Additionally, considering that the micropillar will be inserted into organic slices, these structures should be tested about the mechanical resistance mechanical resistance. Although each bulk of the nanowires on recording site, are fabricated in such manner that are compacted against each other; the nanowires are not free of bulking upon the insertion. However the method offers the possibility to adjust the height of the base by adapting the photoresist thickness during the photolithography for the base and the nanowires by the electrodeposition time.

Chapter 5

Conclusion

Attending to the requirements that features a microelectrode suitable for organotypic cultures; the ultimate goal in this work is to be able to build a 3D microelectrode, with the most viable high aspect ratio as possible and least 100 μm height micropillar, so that is able to surpass the necrotic layer inherent to the brain slices. Therefore it was proposed a microfabrication process based on template-assisted gold electrodeposition.

Despite the simplicity of the techniques used in the process, it is possible to conclude that, coherently with the literature, the transference of the NpAT to the substrate is a considerable challenging point of the process. However the results acquired from the different adjustments in the sample preparation and subsequent electrodeposition into the NpAT, are not enough to understand the reason for the NpAT assuming an arc form after package into the setup. Nevertheless is hypothesized two possibilities for the cause of such event; due the pressure exercised by the O-ring rubber or/ the presence of eventual impurities.

Therefore it would be interesting to repeat some of the experience to confirm some of the results, as well as experiment new preparation conditions and further assess the mechanical, electrical and chemical properties of the product, as discussed in section XX. Once the key condition for the samples preparation that allow for transferring the NpAT to the substrate is disclosed it will impulse the fabrication of microelectrodes, and consequently promote advances in neuroscience. Once the chemical, electrical and morphological characterization correspond successfully to the designed microelectrode, it would be interesting to further investigate the biocompatibility, by cultivating cell on the 3Dmicroelectro fabricates and assess their reaction to it as well as test the its efficiency

Bibliography

- [1] L. Luo, Principles of Neurobiology. 4th ed. Garland Science, 2016
- [2] L. Squire, D. Berg, , F. E. Bloom, S. Du Lac, A. Ghosh, & N. C. Spitzer, Fundamental neuroscience. Academic Press, 2012.
- [3] J. Rivnay, "Next-generation probes, particles, and proteins for neural interfacing.", Science Advances, 3(6), 2017, pp.e1601649. DOI: 10.1126/sciadv.1601649
- [4] W. Gong, J. Sencar, D. Jäckel, J. Müller, M. Fiscella, M. Radivojevic, D. Bakkum, A. Hierlemann, " Long-Term, High-Spatiotemporal Resolution Recording From Cultured Organotypic Slices With High-Density Microelectrode Arrays." *International Conference on Solid-State Sensors, Actuators and Microsystems (TRANSDUCERS)*, IEEE, 2015. pp.1037-1040, doi: 10.1109/TRANSDUCERS.2015.7181103.
- [5] M. Jorfi, J. L. Skousen, C. Weder, & J. R. Capadona, "Progress towards biocompatible intracortical microelectrodes for neural interfacing applications." *Journal of neural engineering*, 12(1), 2014. pp. 011001. doi: 10.1088/1741-2560/12/1/011001
- [6] M. B. Taketani, *Advances in Network Electrophysiology: Using Multi-Electrode Arrays*, Springer, Boston, 2006: pp. 69-73.
- [7] G. Hong, and C. M. Lieber, "Novel electrode technologies for neural recordings." *Nature Reviews Neuroscience*, 20(6), 2019. pp.330-345, doi.org/10.1038/s41583-019-0140-6
- [8] M. Heidemann, J. Streit, and A. Tschertter, "Investigating Functional Regeneration in Organotypic Spinal Cord Co-cultures Grown on Multi-electrode Arrays". *JoVE (Jornal of Visualized Experiments)*, 103, 2015. pp.e53121. DOI: 10.3791/53121
- [9] G. H. Kim, K. Kim, E. Lee, T. An, W. Choi, G. Lim, & J. H. Shin, "Recent Progress on Microelectrodes in Neural Interfaces". *Materials*, 11(10), 2018. DOI: 10.3390/ma11101995
- [10] A. B. Kibler, B. G. Jamieson, and D.M. Durand, "A high aspect ratio microelectrode array for mapping neural activity in vitro." *Journal Of Neuroscience Methods*, 204(2), 2012 pp. 296-305. DOI: 10.1016/j.jneumeth.2011.11.027
- [11] C. Humpel, "Organotypic brain slice cultures: A review." *Neuroscience*, 305, 2015, pp. 86-98. DOI: 10.1016/j.neuroscience.2015.07.086
- [12] L. Pires and J. Gaspar, *Nanostructured Biomaterials for Regenerative Medicine*, Micro and nano-needles as innovative approach in nanomedicine, Woodhead Publishing, 2020. pp. 379-406. doi.org/10.1016/B978-0-08-102594-9.00014-0.

- [13] W. J. Stępniewski, and M. Salerno, "Fabrication of nanowires and nanotubes by anodic alumina template-assisted electrodeposition." *Manufacturing Nanostructures*, 12, 2014 pp. 321-357.
- [14] R. Abdel-Karim, and S. El-Raghy, *Nanofabrication using Nanomaterials*, Fabrication of nanoporous alumina, OCP (One Central Press), 2016. Chapter 7
- [15] H. A. Scott, A.W.Song, G. McCarthy, *Functional Magnetic Resonance Imaging*, Neuronal to Hemodynamic Activity. Sinauer Associates, 2014.
- [16] G.B. Ermentrout, and D.H. Terman, *Mathematical Foundations of Neuroscience*, The Hodgkin-Huxley Equations, Springer.2010. pp. 1-28.
- [17] D. Sterratt, B.Graham, A.Gilies, D.Wilshaw, *Neuroscience*, Pincipals of Computational Modeling, Cambridge University Press, 2012. doi: 10.1093/bib/bbs003
- [18] C. A. Anastassiou, G. Buzsaki, K.Cyorgy, C. Quiroga, R. Panzeri, *Principles of Neural Coding*, Biophysics of extracellular spikes, 2013. pp. 15-36. DOI: 10.1201/b14756-4
- [19] A. L. Efros, J. B. Delehanty, A. L. Huston, I. L. Medintz, M. Barbic, T. D. Harris, "Evaluating the potential of using quantum dots for monitoring electrical signals in neurons." *Nature Nanotechnology*, 13(4), 2018, pp. 278. doi.org/10.1038/s41565-018-0107-1
- [20] A. L. Hodgkin, A. F. Huxley, and B. Katz, "Measurement of current-voltage relations in the membrane of the giant axon of Loligo." *The Journal Of Physiology*, 116(4), 1952. pp. 424-448. doi: 10.1113/jphysiol.1952.sp004716
- [21] A. L. Hodgkin, and A. F. Huxley, "The dual effect of membrane potential on sodium conductance in the giant axon of Loligo." *The Journal Of Physiology*, 116(4), 1952. pp. 497-506. doi: 10.1113/jphysiol.1952.sp004719
- [22] A. L. Hodgkin, and A. F. Huxley, "The components of membrane conductance in the giant axon of Loligo." *The Journal Of Physiology*, 116(4), 1952. pp. 473-496. doi: 10.1113/jphysiol.1952.sp004718
- [23] A.L.Hodgkin, and A.F. Huxley, "A quantitative description of membrane current and its application to conduction and excitation in nerve." *The Journal Of Physiology*, 116(4), 1952. pp. 500-544. doi: 10.1113/jphysiol.1952.sp004764
- [24] A.L. Hodgkin, and A.F. Huxley, "Currents carried by sodium and potassium ions through the membrane of the giant axon of Loligo." *The Journal Of Physiology*, 116(4), 1952. pp. 449-472. DOI: 10.1113/jphysiol.1952.sp004717
- [25] I. Magrans de Abril, J. Yoshimoto, and K. Doya, "Connectivity inference from neural recording data: Challenges, mathematical bases and research directions." *Neural Netw*, 102, 2018 pp. 120-137. doi.org/10.1016/j.neunet.2018.02.016
- [26] M.E.J. Obien, K.Deligkaris,T.Bullmann, D. J. Bakkum, & U.Frey, "Revealing neuronal function through microelectrode array recordings." *Frontiers in neuroscience*, 8, 2015. pp. 423. doi.org/10.3389/fnins.2014.00423
- [27] S.Canakci, M. F. Toy, A. F. Inci, X. Liu, & D. Kuzum, "Computational analysis of network activity and spatial reach of sharp wave-ripples." *PloS one*, 12(9), 2017, pp. e0184542. doi.org/10.1371/journal.pone.0184542
- [28] Z.Huang, *Signal Processing in Neuroscience*, Brief History and Development of Electrophysiological Recording Techniques in Neuroscience, Springer, 2016, p. 1-10. doi.org/10.1007/978-981-10-1822-0_1

- [29] W. Ridings. "Brain layers." Available from: www.whitneyridings.com/#/brain-layers/. Accessed in January 26th 2020
- [30] P. Fattahi, G. Yang, G. Kim, & M. R. Abidian, "A review of organic and inorganic biomaterials for neural interfaces." *Advanced Materials*, 26(12), 2014. pp. 1846-85. doi.org/10.1002/adma.201304496
- [31] Lab, T.M.P.V. Intracellular versus Extracellular recording. Available from: http://www.medicine.mcgill.ca/physio/vlab/other_exps/CAP/recording.htm. Accessed in January 26th 2020
- [32] G. Buzsaki, C. A. Anastassiou and C. Koch, "The origin of extracellular fields and currents--EEG, ECoG, LFP and spikes." *Nature Reviews Neuroscience*, 13(6), 2012. pp. 407-20. doi.org/10.1038/nrn3241
- [33] P. Massobrio, G. Massobrio, and S. Martinoia, "Interfacing Cultured Neurons to Microtransducers Arrays: A Review of the Neuro-Electronic Junction Models." *Frontiers Neuroscience*, 10, 2016. pp. 282. doi.org/10.3389/fnins.2016.00282
- [34] D. Kleinfeld, L. Luan, P.P. Mitra, J.T. Robinson, R. Sarpeshkar, K. Shepard, C. Xie, T.D. Harris, "Can One Concurrently Record Electrical Spikes from Every Neuron in a Mammalian Brain?" *Neuron*, 103(6), 2019. pp. 1005-1015. doi.org/10.1016/j.neuron.2019.08.011.
- [35] A. Veronica, Y. Li, & I. M. Hsing, "Minimally Invasive & Long-lasting Neural Probes from a Materials Perspective." *Electroanalysis*, 31(4), 2019, pp.586-602. DOI: 10.1002/elan.201800719
- [36] P. R. F. Rocha, P. Schlett, U. Kintzel, V. Mailänder, L. K. J. Vandamme, and G. Zeck, H. L. Gomes, F. Biscarini, D. M. Leeuw, "Electrochemical noise and impedance of Au electrode/ electrolyte interfaces enabling extracellular detection of glioma cell populations." *Nature Scientific Reports*, 2016. doi.org/10.1038/srep34843
- [37] The Constant Phase Element (CPE). Available from: www.consultrsr.net/resources/eis/cpe1.htm. Accessed at November 15th 2019
- [38] K. M. Szostak, L. Grand, and T. G. Constandinou, "Neural Interfaces for Intracortical Recording: Requirements, Fabrication Methods, and Characteristics." *Frontiers Neurosci*, 11, 2017. pp. 665, doi.org/10.3389/fnins.2017.00665
- [39] R. Wang, H. Yu, Z. Li, "Microelectrode Array." *Micro Electro Mechanical Systems*. vol 2. In: Huang QA, Springer, Singapore, 2018. pp.1-33. doi:10.1007/978-981-10-2798-7_41-1
- [40] S. P. Lacour, S. Benmerah, E. Tarte, "Flexible and stretchable micro-electrodes for in vitro and in vivo neural interfaces." *Medical & biological engineering & computing*, 48(10), 2010. pp. 945-954. DOI: 10.1007/s11517-010-0644-8
- [41] L. Maiolo, D. Polese, and A. Convertino, "The rise of flexible electronics in neuroscience, from materials selection to in vitro and in vivo applications." *Advances in Physics: X*, 4(1), 2019. pp. 1664319 doi.org/10.1080/23746149.2019.1664319
- [42] S. Moussa, and J. Mauzeroll, "Microelectrodes: An Overview of Probe Development and Bioelectrochemistry Applications from 2013 to 2018." *Journal of The Electrochemical Society*, 166(6), 2019. pp. G25-G38. DOI: 10.1149/2.0741906jes
- [43] A. Weltman, J. Yoo, and E. Meng, "Flexible, penetrating brain probes enabled by advances in polymer microfabrication." *Micromachines*, 7(10), 2016. pp. 180. DOI: 10.3390/mi7100180

- [44] M. Gulino, K. Donghoon, S. Pané, S. D. Santos, & A. P. Pêgo, "Tissue Response to Neural Implants: The Use of Model Systems Toward New Design Solutions of Implantable Microelectrodes." *Frontiers Neuroscience*, 13, 2019. pp. 689. doi.org/10.3389/fnins.2019.00689
- [45] J. C. Williams, R. L. Rennaker, and D.R. Kipke, "Long-term neural recording characteristics of wire microelectrode arrays implanted in cerebral cortex." *Brain Research Protocols*, 4(3), 1999. pp. 303-313. DOI: 10.1016/s1385-299x(99)00034-3
- [46] D. A. Schwarz, "Chronic, wireless recordings of large-scale brain activity in freely moving rhesus monkeys." 11(6), *Nature methods*, 2014. pp. 670-676. doi.org/10.1038/nmeth.2936
- [47] M. A. Nicolelis, "Chronic, multisite, multielectrode recordings in macaque monkeys." *Proceedings of the National Academy of Sciences*, 100(19), 2003. pp. 11041-11046. doi.org/10.1073/pnas.1934665100
- [48] A. C. Patil, and N. V.Thakor, "Implantable neurotechnologies: a review of micro- and nanoelectrodes for neural recording." *Medical & Biological Engineering Computing*, 54(1), 2016. pp. 23-44. DOI: 10.1007/s11517-015-1430-4
- [49] D. Khudhair, *Emerging Trends in Neuro Engineering and Neural Computation. Microelectrode Arrays: Architecture, Challenges and Engineering Solutions*, 2017, Springer. p. 41-59. DOI: 10.1007/978-981-10-3957-7
- [50] K. D.Wise, J. B. Angell, and A. Starr, "An integrated-circuit approach to extracellular microelectrodes." *IEEE transactions on biomedical engineering*, vol. BME-17, no. 3, 1970, pp. 238-247, doi: 10.1109/TBME.1970.4502738
- [51] T. C. A. Thomas, P. A. Springer, G. E. Loeb, Y. Berwald-Netter, L. M. Okun, "A miniature microelectrode array to monitor the bioelectric activity of cultured cells", *Experimental Cell Research*, 74(1), 1972, pp.61-66, /doi.org/10.1016/0014-4827(72)90481-8..
- [52] M. E. Spira, and A. Hai, "Multi-electrode array technologies for neuroscience and cardiology." *Nature Nanotechnology*, 8(2), 2013. pp. 83-94. doi.org/10.1038/nnano.2012.265
- [53] U. Frey, U. Egert, F. Heer, S. Hafizovic, A. Hierlemann , "Microelectronic system for high-resolution mapping of extracellular electric fields applied to brain slices." *Biosensors Bioelectronics*, 24(7), 2009. pp. 2191-8. doi.org/10.1016/j.bios.2008.11.028.
- [54] B. Eversmann et al., "A 128 × 128 CMOS Biosensor Array for Extracellular Recording of Neural Activity.", *IEEE J Solid-State Circuits*, 38(12), 2003, pp. 2306-2317, doi: 10.1109/JSSC.2003.819174.
- [55] M.O. Heuschkel, M. Fejtl, M. Raggenbass, D. Bertrand, P.Renaud "A three-dimensional multi-electrode array for multi-site stimulation and recording in acute brain slices." *Journal Neuroscience Methods*. 114(2), 2002 , pp.135-48. doi: 10.1016/s0165-0270(01)00514-3.
- [56] S.Ojovan, , N. Rabieh, , N.Shmoel, "A feasibility study of multi-site,intracellular recordings from mammalian neurons by extracellular gold mushroom-shaped microelectrodes." *Scientific Reports*, 5(1), 2015, pp. 1-14.. doi.org/10.1038/srep14100

- [57] G. Piret, C. Hébert, J. P. Mazellier, L. Rousseau, E. Scorsone, M. Cottance, G. Lissorgues, M.O. Heuschkel, S. Picaud, P. Bergonzo, B. Yvert, "3D-nanostructured boron-doped diamond for microelectrode array neural interfacing." *Biomaterials*, 53, 2015. pp. 173-183. doi.org/10.1016/j.biomaterials.2015.02.021
- [58] P. Paci, S. Gabriele, and L. Ris, "A new method allowing long-term potentiation recordings in hippocampal organotypic slices." *Brain Behaviour*, 7(5), 2017. pp. e00692. DOI: 10.1002/brb3.692
- [59] J. Wellbourne-Wood, and J.-Y. Chatton, "From cultured rodent neurons to human brain tissue: Model systems for pharmacological and translational neuroscience." *ACS chemical neuroscience*, 9(8), 2018. pp. 1975-1985. DOI: 10.1021/acscchemneuro.8b00098
- [60] Z. Yu, and B. Morrison III, "Experimental mild traumatic brain injury induces functional alteration of the developing hippocampus." *Journal of Neurophysiology*, 103(1), 2010. pp. 499-510. DOI: 10.1152/jn.00775.2009
- [61] W. Boyd, "A chamber for organotypic culture; adapted for growing large volumes of tissue." *Stain Technology*, 46(2), 1971. pp. 85-87. doi.org/10.3109/10520297109067827
- [62] B. Gähwiler, "Organotypic monolayer cultures of nervous tissue." *Journal of Neuroscience Methods*, 4(4), 1981. pp. 329-342. doi.org/10.1016/0165-0270(81)90003-0
- [63] L. Stoppini, P.A. Buchs, and D. Muller, "A simple method for organotypic cultures of nervous tissue." *Journal of neuroscience methods*, 37(2), 1991. pp. 173-182. doi: 10.1016/0165-0270(91)90128-m.
- [64] M. Pisciotto, G. Morgavi, and H. Jahnsen, "Characterization of the in vitro propagation of epileptiform electrophysiological activity in organotypic hippocampal slice cultures coupled to 3D microelectrode arrays." *Brain Research*, 1358, 2010. pp. 46-53. DOI: 10.1016/j.brainres.2010.08.028
- [65] Y. Wu, H. Chen, and L. Guo, "Opportunities and dilemmas of in vitro nano neural electrodes." *RSC Advances*, 10(1), 2020. pp. 187-200. DOI: 10.1039/C9RA08917A
- [66] G. Charvet, L. Rousseau, O. Billoint, S. Gharbi, J. P. Rostaing, S. Joucla, M. Trevisiol, A. Bourgerette, P. Chauvet, C. Moulin, F. Goy, B. Mercier, M. Colin, S. Spirkovitch, H. Fanet, P. Meyrand, R. Guillemaud, B. Yvert, "BioMEA™: A versatile high-density 3D microelectrode array system using integrated electronics." *Biosensors and Bioelectronics*, 25(8), 2010. pp. 1889-1896. doi.org/10.1016/j.bios.2010.01.001.
- [67] H. D. Wanzenböck, P. Scholze, and J.K. Mika, *Neurohistology and Imaging Techniques, Imaging and Electrophysiology of Individual Neurites Functionally Isolated in Microchannels*, Springer 2020, p. 341-377. DOI: 10.1007/978-1-0716-0428-1
- [68] A. Spanu, N. Colistra, P. Farisello, A. Friz, N. Arellano, C. T. Rettner, A. Bonfiglio, L. Bozano, S. Martinoia, "A three-dimensional micro-electrode array for in-vitro neuronal interfacing." *Journal of Neural Engineering*, 2020. DOI: 10.1088/1741-2552/ab9844
- [69] S. Rajaraman, "Three-dimensional metal transfer micromolded microelectrode arrays (MEAs) for in-vitro brain slice recordings." *Actuators and Microsystems Conference, TRANSDUCERS 2007-2007 International Solid-State Sensors 2007, IEEE*, Lyon, 2007, pp. 1251-1254, doi: 10.1109/SENSOR.2007.4300364.

- [70] A. Biswas, I. S. Bayer, A. S. Biris, T. Wang, E. Dervishi, F. Faupel, "Advances in top-down and bottom-up surface nanofabrication: Techniques, applications & future prospects." *Advances in colloid and interface science*. 170(1-2), 2012. pp. 2-27. doi.org/10.1016/j.cis.2011.11.001
- [71] A. Mallik and B. Ray, "Evolution of principle and practice of electrodeposited thin film: a review on effect of temperature and sonication." *International Journal of Electrochemistry*, vol.2011, 2011. pp. 568023. DOI: 10.4061/2011/568023
- [72] Y.D.Gamburg, and G. Zangari, *Theory and practice of metal electrodeposition*. Springer Science & Business Media, 2011. pp1-25. DOI: 10.1007/978-1-4419-9669-5_1
- [73] L. P. Bicelli, B. Bnedetto, C. Mele, L. D' Urzo, "A review of nanostructural aspects of metal electrodeposition." *International Journal of Electrochemical Science*, 3(4), 2008. pp. 356-408.
- [74] J. Guiliani, J. Cadena, and C. Monton, "Template-assisted electrodeposition of Ni and Ni/Au nanowires on planar and curved substrates." *Nanotechnology*, 29(7), 2018. pp. 075301. DOI: 10.1088/1361-6528/aaa261
- [75] A. J. Bard and L. R. Faulkner, *Electrochemical Methods: Fundamentals and applications*, Russian Journal of Electrochemistry 38, ed 2, 2002, pp.1364-1365. doi.org/10.1023/A:1021637209564
- [76] L. Fan, H. L. Zhuang W. Zhang Y. Fu Z. Liao, Y. Lu, "Stable Lithium Electrodeposition at Ultra-High Current Densities Enabled by 3D PMF/Li Composite Anode." *Advanced Energy Materials*, 28(15), 2018. pp. 1703360. doi.org/10.1002/aenm.201703360
- [77] C. Nick, S. Quednau, R. Sarwar, H. F. Schlaak & C. Thielemann "High aspect ratio gold nanopillars on microelectrodes for neural interfaces." *Microsystem technologies*, 20(10-11), 2014. pp. 1849-1857. doi.org/10.1007/s00542-013-1958-x
- [78] I. Lombardi, P. L. Cavallotti, C. Carraro, R. Maboudian, "Template assisted deposition of Ag nanoparticle arrays for surface-enhanced Raman scattering applications." *Sensors and Actuators B: Chemical*, 125(2), 2007. pp. 353-356. doi.org/10.1016/j.snb.2007.02.057